University of Alberta

Analytical electron microscopy of thin films

by

Marek Malac ©

A thesis submitted to the Faculty of Graduate Studies and Research in partial fulfillment of the requirements for the degree of Doctor of Philosophy

Department of Physics

Edmonton, Alberta

Fall 2000

National Library of Canada
Acquisitions and Bibliographic Services
395 Wellington Street
Ottawa ON K1A 0N4
Canada

Bibliothèque nationale du Canada
Acquisitions et services bibliographiques
395, rue Wellington
Ottawa ON K1A 0N4
Canada

Your file Votre référence

Our file Notre référence

The author has granted a non-exclusive licence allowing the National Library of Canada to reproduce, loan, distribute or sell copies of this thesis in microform, paper or electronic formats.

L'auteur a accordé une licence non exclusive permettant à la Bibliothèque nationale du Canada de reproduire, prêter, distribuer ou vendre des copies de cette thèse sous la forme de microfiche/film, de reproduction sur papier ou sur format électronique.

The author retains ownership of the copyright in this thesis. Neither the thesis nor substantial extracts from it may be printed or otherwise reproduced without the author's permission.

L'auteur conserve la propriété du droit d'auteur qui protège cette thèse. Ni la thèse ni des extraits substantiels de celle-ci ne doivent être imprimés ou autrement reproduits sans son autorisation.

0-612-59627-3

Canada

University of Alberta

Library release form

Name of Author: Marek Malac

Title of Thesis: Analytical electron microscopy of thin films

Degree: Doctor of Philosophy

Year this Degree Granted: 2000

Permission is hereby granted to the University of Alberta Library to reproduce single copies of this thesis and lend or sell such copies for private, scholarly or scientific purposes only.

The author reserves all other publication and other rights in association with the copyright in the thesis, and except as herein before provided, neither the thesis nor any substantial portion thereof may be printed or otherwise reproduced in any material form whatever without the author's written permission.

Date: 13th September 2000

Marek Malac

10944 74 Avenue

Edmonton, Alberta

Canada T6G 0E6

University of Alberta

Faculty of Graduate Studies and Research

The undersigned certify that the have read, and recommended to the Faculty of Graduate Studies and Research for acceptance, a thesis entitled **Analytical electron microscopy of thin films** submitted by Marek Malac in partial fulfillment of the requirements for the degree of Doctor of Philosophy

R.F. Egerton

Dr. Raymond F. Egerton (supervisor)

Dr. Mark Freeman (chair)

John Beamish

Dr. John Beamish

Dr. Frank Marsiglio

Dr. Frank Hegman

Dr. Mike J. Brett

R.F. Egerton

Dr. Doug Perovic

Date: 13th September 2000

Abstract:

An analytical transmission electron microscope (ATEM) yields an impressive amount of information from a single instrument. The chemical composition of small areas of a sample is often obtained by energy dispersive x-ray microanalysis (EDX). EDX is routinely used both in research and industry to obtain fractions of heavier elements ($Z > 11$). To allow quantitative EDX analysis of samples containing light elements (B, C, N, O, F, Mg and Si) we developed, fabricated and characterized a set of three calibration samples. These calibration specimens allow users to obtain experimental Cliff-Lorimer factors with 10% to 15% accuracy and are sufficiently stable during storage, as well as under electron beam irradiation. Quantitative electron energy-loss spectroscopy (EELS) was employed to characterize these samples.

The good light-element sensitivity of EELS makes it a suitable method for chemical analysis of biological samples in ATEM. It is desirable to probe the detection limits of EELS and energy filtering transmission electron microscopy (EFTEM) as well as determine what physical processes underlying these limits. We find that a TEM / EELS system is capable quantifying of 2000 ppm of boron with about 10% accuracy and 1 μm resolution. EFTEM mapping using Gatan Image filter is capable of mapping 5000 ppm of boron with 66 nm pixel size. The minimum detectable fraction (MDF) was limited by detector gain-variations and beam-shot noise. Spatial (EFTEM or TEM / EELS) mapping of low boron concentrations is important for boron-neutron capture therapy (BNCT), a method of cancer treatment.

The high spatial resolution of TEM imaging and chemical analysis was applied to study microscopic mechanism of growth of thin films deposited onto oblique (rotating) substrate. The structure of these films can vary between arrays of columns (stationary substrate), helices (slowly-rotated substrate) or pillars (fast-rotated substrate). These structures (columns, pillars, helices) are composed of many individual fibers growing simultaneously. The fiber-diameter is characteristic of the deposition material and its ratio of substrate and melting point temperatures (T_s/T_m). Our experiments show that it is possible to grow *regular* arrays of pillars or helices by depositing onto a substrate which has been pre-patterned with an array of artificial nuclei. The repeat distance of such regular arrays can be varied at least between 18 nm and one micrometer. The pillars and helices within a regular array have narrower size distributions than those within a random array. This property can be attributed to the regularity of shadowing within a regular array.

Acknowledgements:

I would like to thank my wife Katka and my parents for their continued support. I'm deeply indebted to my supervisor Dr. Ray Egerton for his patience, kind advice and support. I would like to thank Dr. Mark Freeman, Dr. Mike Brett and Dr. Frank Marsiglio for their encouragement and fruitful discussions. I would like to thank Dr. Yimei Zhu for his advice, help and invitation to his group at Brookhaven National Laboratory.

Last, but not least my thanks belong to Mr. Donald Mullin, Mr. Tony Wallford, Mr. Steve Rogers, Ms. Yolande Peske and Ms. Lynn Chandler for their technical and administrative help.

Table of Contents

Chapter 1	Introduction	1
Chapter 2	Calibration Specimens for Determining Energy-Dispersive X-ray k-factors of Boron, Carbon, Nitrogen, Oxygen and Fluorine	8
	2.1 Introduction	8
	2.2 Materials and Methods	10
	2.3 Results and Discussion	14
	2.3.1 Film Characterization by EELS	14
	2.3.2 Effect of specimen x-ray absorption	18
	2.3.3 Film stability during storage and irradiation	21
	2.3.4 Measurement of EDX k-factors	24
	2.3.5 Specimen uniformity	28
	2.4 Conclusions	30
	2.5 References	31
Chapter 3	Concentration Limits For the Measurement of Boron By Electron Energy-Loss Spectroscopy and Electron-Spectroscopic Imaging	33
	3.1 Introduction	33
	3.2 Experimental	35
	3.3 Results and discussion	39
	3.3.1 Measurement of boron and carbon ratio	39
	3.3.2 Detection limit for an ideal detector	43
	3.3.3 Boron mapping using EFTEM mapping	44
	3.3.4 Radiation damage and boron mapping of the TMV samples	48
	3.3.5 Comparison of GIF and PEELS systems	53
	3.4. Conclusions	56
	3.5 References	56
Chapter 4	Fabrication of submicrometer regular arrays of pillars and helices	58
	4.1 Introduction	58
	4.2 Materials and Methods	59
	4.3 Results	64
	4.4 Conclusions	68
	4.5 References	68
Chapter 5	Observations of the microscopic growth mechanism of pillars and helices formed by glancing-angle thin-film deposition	69

5.1 Introduction 69
5.2 Experimental methods 71
5.3 Results and discussion 72
5.3.1 Randomly nucleated films 72
5.3.1.1 Shadowing within and between helices 75
5.3.1.2 Importance of diffusion processes and crystallinity 77
5.3.1.3 Comparison with films deposited onto a *stationary* oblique substrate 82
5.3.1.4 Initial stages of growth of randomly nucleated arrays 85
5.3.1.5 Pillars – deposition onto a *fast-rotating* substrate 88
5.3.2 Films grown onto a patterned substrate 90
5.3.2.1 Differences in the growth of regular and random arrays 90
5.3.2.2 Introduction of a defect into a regular array 93
5.4 Conclusions 95
5.5 References 97

Chapter 6 Thin-film regular-array structures with 10-100nm repeat distance 100

6.1 References 108

Chapter 7 General discussion and conclusion 110
7.1 References 115

Chapter 8 Appendices 121

Appendix A Calibration sample preparation procedures 118
A.1 Sample A (C-O-Si) 118
A.2 Sample B (B-N-O-Si) 119
A.3 Sample C (B-F-Mg-Si) 121

Appendix B Details of contamination lithography in JEOL 2010 124
Appendix C Program for beam scanning in the JEOL 2010 127
Appendix D Lithography on bulk silicon substrates 131
Appendix E Substrate rotation device for growth using Glancing Angle Deposition technique 132
Appendix F Electron energy-loss spectroscopy (EELS) 133
F.1 References 135

Appendix G Energy dispersive x-ray microanalysis (EDX) 136
G.1 References 137
Appendix H Selected unpublished micrographs 138

List of Tables

Chapter 2

Table 2.1. Oxygen/silicon atomic ratios measured from a SiO_2 film 16

Table 2.2. Ratios by weight of light elements present in the calibration specimens 16

Chapter 3

Table 3.1. Quantification of a boron test specimen by EELS in TEM 40

Table 3.2. Boron to carbon ratios in sample with 0.2% nominal boron fraction 42

Chapter 4

Table 4.1. Deposition parameters for growth of pillars and helices 63

List of Figures

Chapter 2

Figure 2.1 Characterization of specimen A (C-O-Si) 17
Figure 2.2 Percentage absorption of characteristic x-rays in calibration specimens 20
Figure 2.3 Radiation stability of calibration specimens 23
Figure 2.4 Typical EDX spectra of the calibration specimens 26
Figure 2.5 Zero-thickness EDX k*-factors for the Noran HPGe detector 27
Figure 2.6 Calculated percentage absorption of characteristic x-rays in an H_2O-ice contamination layer 29
Figure 2.7 Spatial uniformity of the calibration samples 29

Chapter 3

Figure 3.1 Background-subtracted Boron-K and Carbon-K edges 41
Figure 3.2 Boron mapping of the shadow masked non-uniform sample 47
Figure 3.3 Radiation sensitivity of BPA 51
Figure 3.4 Boron mapping in the BPA-stained tobacco mosaic virus (TMV) sample 52

Chapter 4

Figure 4.1 Substrate positions in chamber and geometrical considerations for growth of regular arrays. 61
Figure 4.2 SEM image of regular array of titanium helices 64
Figure 4.3 SEM image of regular array of titanium pillars 64
Figure 4.4 SEM image of regular array of cobalt pillars 65

Chapter 5

Figure 5.1 a) Substrate positions and movements in the deposition chamber. b) locations of the thermocouple and radiative heater. 70
Figure 5.2 Cross-sectional SEM micrograph of a randomly-nucleated array of silicon helices. 74
Figure 5.3 Cross-sectional TEM micrograph of a portion of a silicon helix from the same sample as figure 2. Inset: fiber diameter distribution. 74
Figure 5.4 Cross-sectional TEM micrograph of a narrow bismuth helix. Inset is diffraction pattern from the upper half of the helix. 80
Figure 5.5 Typical profile of temperature rise with increasing film thickness. 80

Figure 5.6 Cross-sectional TEM micrograph of silicon columns deposited onto a stationary substrate. 84
Figure 5.7 Initial stages of growth of nickel pillars. 87
Figure 5.8 Initial growth stage of a nickel film deposited onto a stationary thin-carbon substrate. 87
Figure 5.9 Cross-sectional TEM micrograph of titanium pillar. 89
Figure 5.10 a) Geometrical considerations for patterning artificial nuclei for growth of a regular array of pillars or helices. b) Top view SEM micrograph of a border between regular and random areas of a silicon-helix array. 92
Figure 5.11 a) Line defect within a regular array of silicon pillars with 1 μm repeat distance. b) Side view of a pillar within the same area. 94

Chapter 6

Figure 6.1 GLAD technique; position of the substrates in the vacuum chamber and substrate rotation during the film growth 101
Figure 6.2 Scanning electron micrograph of regular array of large silicon helices with repeat distance a = 1250 nm. 101
Figure 6.3 Transmission electron micrograph of initial stage of growth of silicon helices grown onto a patterned 10 nm-thick amorphous carbon film 104
Figure 6.4 Cross-sectional TEM micrograph of a regular array of nickel pillars with repeat distance a = 35 nm. 104

Chapter 8 Appendices

Figure H.1 Bismuth helix with bifurcation 140
Figure H.2 Array of nickel pillars with 18 nm repeat distance 140
Figure H.3 SEM micrograph of titanium pillars 140
Figure H.4 SEM micrograph of titanium helices 140
Figure H.5 Point defect in a regular array of silicon pillars 143
Figure H.6 Initial pattern on a bulk-silicon substrate (PMMA) 143
Figure H.7 TEM patterned substrate 143
Figure H.8 SEM micrograph of initial stages of growth of silicon helices 146
Figure H.9 Crystallites in a nickel helix 146
Figure H.10 Filling of helix-pitch in titanium structures 146

Chapter 1

Introduction

The thesis concerns electron microscopy and microanalysis of thin-film specimens. The work presented can be divided in two main parts which are complementary to each other. On the one hand, thin-film techniques were used to fabricate a set of calibration specimens for a widely used microanalytical method and to fabricate well-defined samples to explore the detection limits of boron. On the other hand, the capability of a transmission-electron to provide information on many levels was exploited with a view to improving our understanding of the physics of thin film growth.

Five chapters (chapter 2,3,4,5 and 6) within this thesis discuss the individual aspects of this work. Each of the above five chapters correspond either to a journal publication or to a manuscript submitted for publication:

- Chapter 2 was published by Marek Malac and Ray Egerton under the title "Calibration Specimens for Determining Energy-Dispersive X-ray k-factors of Boron, Carbon, Nitrogen, Oxygen and Fluorine" in Microscopy and Microanalysis 5 (1999), pages 29-38.
- Chapter 3 was submitted for publication in Ultramicroscopy by Yimei Zhu, Ray Egerton and Marek Malac under the title "Concentration Limits for the Measurement of Boron by Electron Energy-Loss Spectroscopy and Electron-Spectroscopic Imaging".

- Chapter 4 "Fabrication of submicrometer regular arrays of pillars and helices" was published by Marek Malac, Ray Egerton, Mike Brett and Brian Dick in Journal of Vacuum Science and Technology B 17(6), 1999, pages 2671-2674.
- Chapter 5 "Microscopic growth mechanism of pillars and helices grown onto an oblique substrate" was accepted for publication in Journal of Vacuum Science and Technology A by Marek Malac and Ray Egerton.
- Chapter 6 "Thin-film regular-array structures with 10-100nm repeat distance" was submitted for publication in Nanotechnology by Marek Malac and Ray Egerton.
- Chapter 7 "General discussion and conclusions" outlines the relation of the work described in individual chapters to current research.

Chapter 2 discusses development, fabrication and characterization of samples for the calibration of Energy-Dispersive X-ray (EDX) detectors. These samples are necessary for microscopists who attempt *quantitative* analysis of light elements ($Z < 11$) using the EDX technique. Such analysis is important to biologists since most of the tissue is composed of light elements. The ability to provide quantitative measurement of light elements is also relevant to material scientists who design new materials and engineer new electronic devices. To ensure correct use of the calibration samples (commercially available under name LoZiCal^{TM}), Chapter 2 also provides guidelines on their employment. During this project I had a chance to acquire practical experience with a TEM and its microanalytical techniques. I learned about the

limitation of those techniques and the physical reasons underlying these limitations. A short description of principle and some practical issues of energy-dispersive x-ray microanalysis (EDX) is give in appendix 8.7.

Experience with microanalysis in a transmission electron microscope made it possible to expand the project in the direction of exploring the detection limits of boron in biological samples (Chapter 3), which is important in connection with boron-neutron capture therapy (BNCT), a treatment for certain brain cancers. A medium-voltage (200 kV - 300 kV) transmission electron microscope equipped with a parallel electron energy-loss spectrometer (PEELS) proved to be capable of quantitative measurement of boron concentrations down to 0.2% with 10% accuracy. Beam shot noise and gain variations within of the detector array proved to be the factors determining this detection limit for radiation insensitive specimens. For biological applications the radiation sensitivity of the sample limits the spatial resolution in most cases. This information has provided guidance on the suitability of EELS for boron, without the necessity of preparing the samples and attempting to analyse them. A brief description of electron energy-loss spectroscopy technique is given in appendix 8.6.

Whereas Chapters 2 and 3 deal with the microanalytical aspect of the thesis, Chapters 4, 5 and 6 are concerned with aspects of thin film growth. My experience with microanalysis, electron diffraction and TEM imaging enabled me study in some detail the growth of films onto rotating substrates which are oriented obliquely with respect to incoming flux of atoms. Chapter 4 reports (for the first time) the production

of *regular* arrays of pillars and helices via the glancing angle deposition (GLAD) technique. The ability to form a regular array of structures considerably extends the range of applications of the GLAD technique.

As work on the regular arrays proceeded, it became obvious that further study was necessary to improve understanding of the microscopic processes involved in GLAD film growth. These processes and their influence on the final microstructure are discussed in chapter 5. Understanding of the growth process at a microscopic level allows better control of the final microstructure of the film, and improves the likelihood that the GLAD technique will be able to engineer films for more sophisticated applications. In addition to this applied aspect, thin film growth is an example of a non-equilibrium statistical system. Understanding the influence of microscopic variables and our ability to suppress randomness at a certain level opens the possibility of studying such systems in more depth than was previously possible.

Chapter 6 is an extension of the work on regular arrays (described in Chapter 4 and 5) toward very small repeat distances. Exploring the microscopic growth mechanism (Chapter 5) introduced questions about the size limits for the growth of regular arrays and what processes determine these limits. Up to the time of writing, arrays with 18 nm repeat distance have been fabricated. If each element of the array were used to store a single bit of information, this would correspond to a storage density of 2 TB/in^2. This compares favorably with 20 GB/in^2 laboratory demonstrated storage capacity in 1999, suggesting that such regular arrays might perhaps find an

application in fabrication of information-storage media. Even at these small repeat distances, the limits appear to be set by technical difficulties of the lithographic process rather than fundamental physical limits of the technique which is encouraging for possible applications of these films. Additionally, insight into relations between shadowing and diffusion at length scales of a few tens of nanometers improves our understanding of thin-film growth processes.

Transmission electron microscopy proved to be a crucial technique for chemical (EELS and EDX) and morphological (imaging and diffraction) analysis of these fabricated structures. In addition, I have shown that the TEM can be used for the patterning of substrates, leading to the fabrication of structures with a repeat distance below 100 nm.

Since this thesis is composed of publications to which several people have participated, I outline my own contribution to each project as follows. I undertook the fabrication and characterization of the calibration samples described in chapter 2. I calibrated the EDX detector mounted on JEOL 2010 using these samples, thus proving their suitability. I also tested their stability during storage and under electron irradiation, and their spatial uniformity. Within the project on boron detection described in Chapter 3, my participation involved preparing the low-concentration uniform-boron samples, refining the technique for low-concentration uniform-distribution sample analysis in the TEM/EELS system at the University of Alberta, and determining the boron detection limit using this instrument. Determination of the

boron detection limit using the JEOL 3000F equipped with a Gatan Image Filter™ (GIF) was done by Dr. Ray Egerton and Dr. Yimei Zhu at Brookhaven National Laboratory. I also prepared the non-uniform samples involved in the boron mapping experiments, refined the procedure for low-concentration boron mapping using the GIF and performed boron mapping at Brookhaven using these non-uniform test samples. Mapping of the samples containing tobacco mosaic viruses (TMV) is result of my cooperation with Dr. Yimei Zhu. Image processing for the publication was partly done by Dr. Yimei Zhu.

I am responsible for developing and executing the method for growing regular arrays of pillars described in Chapter 4. The cobalt pillars for magnetic recording media described at the end of Chapter 4 were grown by Brian Dick (in Dr. Mike Brett's group in Electrical Engineering) onto arrays of artificial nuclei provided by me and according to my instructions. Work on the growth of pillars and helices described in chapters 5 and 6 was done by myself, although I greatly benefited from frequent consultation with Dr. Ray Egerton and from discussion and encouragement from Dr. Mark Freeman and Dr. Mike Brett.

The figures in this thesis are numbered as in the journal publications but with a chapter number added. For example, figure 3 of the first publication (chapter 2) is numbered figure 2.3 in the text below. The same procedure was applied to the numbering of formulas and tables. The references in chapters 1, 2,3 4, 6, 7 and 8 are in the (Author, Year) format. Large number of references in chapter 5 requires the use of

the [number] format. Each chapter has it's own set of references (as required by the paper format of the thesis), therefore reference to the same author and year in different chapters may not refer to the same publication.

Chapter 2

Calibration Specimens for Determining Energy-Dispersive X-ray k-factors of Boron, Carbon, Nitrogen, Oxygen and Fluorine

(Marek Malac, Ray F. Egerton, published in Microscopy and Microanalysis 5, 29-38, 1999)

2.1 Introduction

Energy-dispersive x-ray (EDX) spectrometry is the most common procedure for performing elemental analysis in a transmission electron microscope (Williams and Carter, 1996). Although energy-loss spectrometry (EELS) is available on an increasing number of TEM's and offers similar capabilities, EDX analysis has remained popular because the equipment and related software is easy to use. Quantitative analysis is possible, and can achieve an accuracy of typically 10% - 15% by use of the k-factor procedure (Cliff and Lorimer, 1975) combined with the use of multi-element standards. Thin-film sputtered-glass standards containing magnesium and heavier elements are available from the National Institute of Science and Technology (NIST) (Steel et al, 1981).

Beryllium windows have been used to protect the cooled EDX detector from condensation of water vapour and hydrocarbons present in the microscope vacuum, but absorption in this relatively thick (>7 μm) window prevents analysis of elements with atomic number below that of sodium (Z<11). The more recent use of thin-window or windowless detectors makes the elements B to F detectable from K-series

peaks, recorded by x-ray emission spectrometry (Williams, 1993). Nevertheless, quantitative analysis of these elements remains problematical. Practical difficulties include separation of the K-emission intensity from a nonlinear background (tail of the noise peak), overlap of the light-element K-emission peaks with L or M peaks of heavier elements, correction for absorption of the low energy x-rays in the specimen (requiring a knowledge of specimen geometry), and insufficient knowledge of the sensitivity (Cliff-Lorimer k-factor) of the x-ray detector for the light elements. To alleviate the last of these problems, we have designed and fabricated test specimens containing the light elements (B, C, N, O, and F) together with silicon, which is a commonly used reference element when specifying k-factors (Williams and Carter, 1996).

The separation between adjacent K-peaks of the light elements varies from 91 eV to 156 eV, while the full widths at half maximum (FWHM) of the EDX peaks are typically between 75 eV and 100 eV in this energy range. If a single specimen contained all of the elements from B to F, there would be considerable peak overlap, making measurement of the characteristic intensities inconvenient and less accurate. To minimize such problems, we originally planned to make two types of specimens: one of them (specimen A) containing carbon, oxygen and silicon the other containing boron, nitrogen, fluorine and silicon. However, it proved difficult to incorporate stable amounts of all four elements in the second sample, so we ended up with three specimens: type A containing carbon, oxygen, and silicon; type B containing nitrogen, silicon, and some boron; and type C containing boron, fluorine, magnesium, and

silicon. The presence of magnesium in specimen C is not detrimental; its K-emission peak does not overlap significantly with those of fluorine or silicon.

2.2 Materials and Methods

Basic requirements of a calibration specimen are that it should be single-phase and uniform in thickness. With such a specimen the incident electron probe can be focussed anywhere on the specimen, and any probe or specimen drift during EDX acquisition will not affect the results. The specimen thickness should be above 30 nm (for mechanical rigidity and to provide adequate x-ray counts) but below 100 nm (so that the measured k-factors will not be affected greatly by absorption within the specimen). Vacuum deposition methods can be used to prepare films in this thickness range, with good uniformity (that is, a thickness variation < 1% over a 2cm x 2cm area).

We have fabricated specimen A by electron-beam evaporation of a mixture of carbon and silicon dioxide. Specimen B is prepared by radio-frequency sputtering of silicon, using nitrogen as the carrier gas, and coated with a thin layer of boron to prevent electrostatic charging in an electron beam. Specimen C is a three-layer structure formed by successive e-beam evaporation of silicon, magnesium fluoride, and boron. For each specimen, we have used a quartz-crystal oscillator to monitor the evaporation rate and film thickness. In every case, the base pressure of the deposition system was below 10^{-6} torr.

As substrates, we have employed mica and single-crystal sodium chloride, cleaved in air just before insertion into the vacuum system. Films can be separated from these substrates by slow immersion into water; surface tension causes the film to float onto the water surface so that small areas can be picked up on 200-mesh TEM grids. We use grids made of copper, whose EDX peaks do not interfere with K-emission peaks of the elements in the film. Up to 50 TEM specimens can be made from each vacuum deposition, using a substrate area of 4 cm^2.

All of the films give electron diffraction patterns containing diffuse halos (broad rings), characteristic of nanocrystalline or amorphous materials. An amorphous (glass) structure is convenient for our purpose because in a crystalline film, electron-channelling effects could cause the x-ray yield to be sensitive to specimen orientation (Hall, 1966). Multi-element amorphous films often have non-stoichiometric elemental ratios, implying that the chemical composition of a specimen may differ in subsequent depositions. However, this variation can be minimized by careful control of the deposition conditions and can be accommodated by measuring the composition of one or more specimens taken from each batch.

We chose electron energy-loss spectrometry as the most suitable method for measuring the composition of a light-element film whose thickness is below 100 nm. We use a JEOL-2010 transmission electron microscope operated at 200kV and fitted with a Gatan Model 666 parallel-recording electron energy-loss (PEELS)

spectrometer. Energy-loss spectra are recorded in TEM-diffraction mode, with the collection angle β (measured as 11 mrad) defined by an objective aperture. The ratio of the areal densities (atoms per unit area) N_A and N_B of two elements (A and B) is given by:

$$N_A / N_B = [I_A(\beta,\Delta) / I_B(\beta,\Delta)]\ [\sigma_B(\beta,\Delta)/\sigma_A(\beta,\Delta)] \qquad (2.1)$$

where $I_A(\beta,\Delta)$ and $I_B(\beta,\Delta)$ are intensities of the corresponding ionization edges, integrated over the same energy width Δ and with the noncharacteristic background at each edge subtracted. We use K-ionization edges for all elements, but for comparison purposes the silicon L-edge was also measured. Energy windows Δ of 50 eV to 200 eV are used for the silicon K-edge, and 50 eV to 100 eV in other cases.

Inner-shell ionization cross sections $\sigma_A(\beta,\Delta)$ and $\sigma_B(\beta,\Delta)$ are calculated using the SIGMAK and SIGMAL computer programs, based on a hydrogenic-atom approximation (Egerton 1996). In fact, these programs are available in several versions. SIGMAK2 and SIGMAL2 contain relatively minor improvements in the computer code, compared to the original SIGMAK and SIGMAL. A survey (Egerton 1993) of the results of Hartree-Slater calculations and experimental EELS and photoabsorption data led to the program SIGPAR (with parameterized oscillator strengths, but valid only for limited collection angles) and to SIGMAL3 and SIGMAK3 (the latter based on an inner-shell screening constant of 0.5 in place of the

original 0.3125). To find out which cross sections best suit our purpose, we used electron-beam evaporation to fabricate thin films of silicon dioxide, which were then analysed using our standardized EELS procedure. In composition, these films appear to be close to SiO_2; their low-loss and L-edge spectra resemble those of SiO_2 (Skiff et al 1987; Batson 1991) with no evidence of L-loss intensity below 106 eV, which would indicate sub-stoichiometry. The results of our EELS analysis are shown in Table 2.1. If we ignore the SIGPAR values, particularly for larger energy windows (where a mean-energy approximation used in the parameterization becomes inaccurate), the elemental ratios are within 10% of the expected value (x=2.0 in SiO_x). Consequently we estimate the accuracy of EELS elemental analysis to be about 10% for the light elements involved in this study. Agreement between measured values of silicon to oxygen ratio and expected value x = 2.0 for SiO_2 can be used as a benchmark for models used for calculating corresponding cross sections. As mentioned above the SIGPAR cross sections are not expected to be correct for larger collection angles β. The SIGPAR cross sections should be used with caution especially if the collection semiangle β and energy window Δ reaches or exceeds region of validity of the dipole approximation (Egerton 1996, p. 425). The Hartree-Slater (HS) calculations, based on HS estimate of the atomic potential, are in reasonable agreement with the expected value of x = 2.0. Hydrogenic-like potential used for calculation of SIGMAK3 (SIGMAK2) cross sections gives good agreement with the expected value of x = 2.0 and is less computation-extensive.

We also use EELS (at 200 keV incident energy and with $\beta = 11$ mrad) to measure the thickness t of each film, in terms of a total-inelastic mean free path $\lambda(\beta)$, making use of the relation:

$$t / \lambda(\beta) = \ln (I_t/I_0) \qquad (2.2)$$

Here I_t is the intensity integrated over the entire energy-loss spectrum and I_0 is the integral of the zero-loss peak. For $\lambda(\beta)$, we use an approximate formula (Malis et al, 1988) which takes into account the film composition. Film thickness is not involved directly in the determination of k-factor, but an approximate value allows the effect of x-ray absorption in the sample to be estimated.

As described more fully in Egerton and Cheng (1994), EDX spectra were collected using a $30mm^2$ HPGE (high purity germanium) detector and a Macintosh IIfx personal computer, via a 4-Pi Analysis data-acquisition board, and displayed using the Desk Top Spectrum Analyser (DTSA) program available from the National Institutes of Science and Technology (NIST).

2.3 Results and Discussion

2.3.1 Film Characterization by EELS

Figure 1a shows a TEM image and the electron diffraction pattern recorded from Specimen A, confirming that the film is amorphous. The structure remained

amorphous even under a focussed electron beam; we saw no evidence of beam-induced crystallization. Figure 2.1b gives the EELS ionization edges obtained from the same specimen; from Eq.(2.1) the composition of the film was determined to be $C_{0.9}$ $O_{1.33}$ Si. The equivalent weight fractions are C/Si = 0.39 and O/Si = 0.75. The use of weight fraction is common in metallurgical work and forms the basis of the usual definition of the k-factor (Williams and Carter 1996, page 600).

Table 2.2 gives weight fractions measured from all three specimens, determined in the same way from EELS. We believe that the presence of oxygen in Specimen B is due to reaction with the atmosphere. Table 2.2 also lists values of $t/\lambda(\beta)$ based on Eq. (2.2), and the corresponding total thicknesses.

model	Δ = 50 eV	Δ = 70 eV	Δ = 100 eV	Δ = 200 eV
SIGMAK2	2.14	2.18	2.18	2.14
SIGMAK3	2.16	2.20	2.19	2.19
SIGPAR2	2.23	2.34	2.35	2.41
HS (Rez)	2.22		2.21	

Table 2.1. Oxygen/silicon atomic ratios measured from a SiO_2 film (using K-loss EELS with β = 11 mrad, E_0 = 200 keV) with cross sections derived from a hydrogenic model (SIGMAK2, SIGMAK3), from parameterized dipole oscillator strengths (SIGPAR2) and from parameterized Hartree-Slater oscillator strengths (Rez, 1990).

	Specimen A (batch 1)	Specimen B (batch 1)	Specimen C (batch 1)
B/Si		0.23	1.7
C/Si	0.39		
N/Si		0.65	
O/Si	0.75	0.28	
F/Si			1.09
Mg/Si			0.78
t/λ	0.18	0.32	0.53
t (nm)	29	49	84

Table 2.2. Ratios by weight (relative to silicon) of light elements present in the calibration specimens, together with values of the inelastic-scattering parameter t/λ and total thickness t .

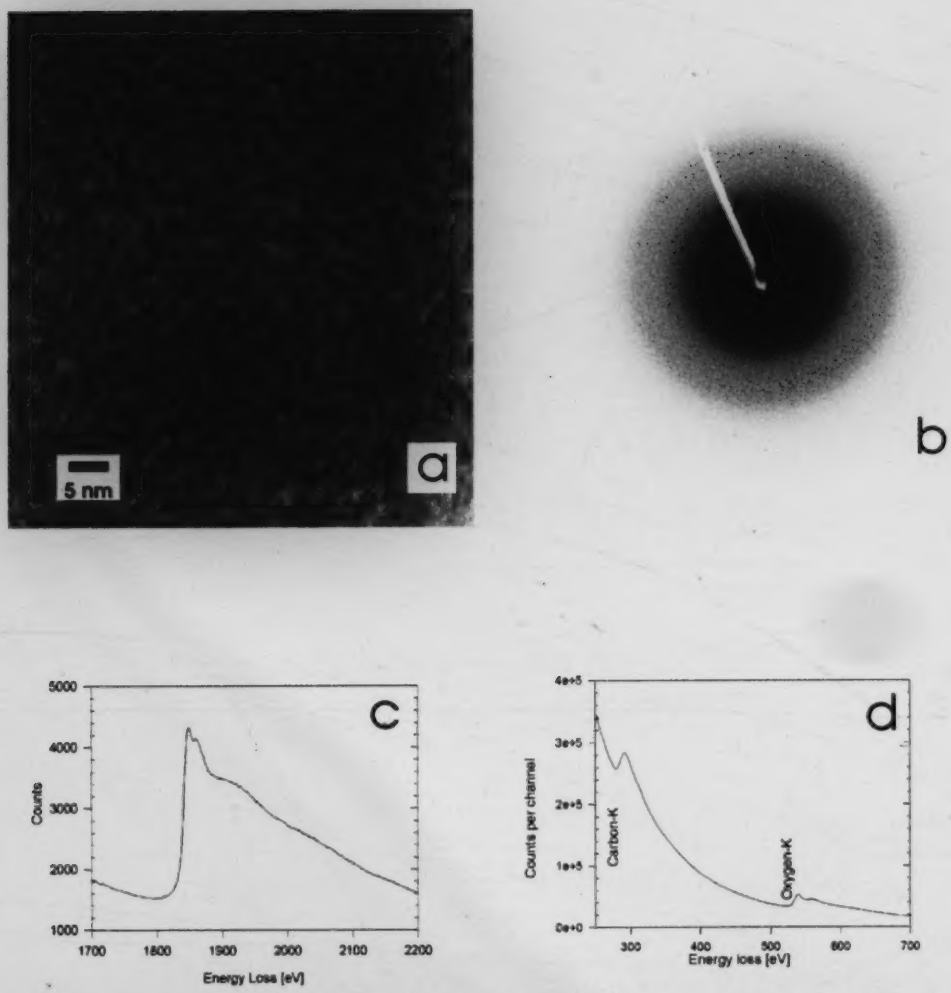

Figure 2.1 (a) TEM image and (b) electron diffraction pattern of Specimen A. (d) Carbon-K and Oxygen-K and (c) Silicon-K energy-loss ionization edges recorded from specimen A using a Gatan 666 PEELS spectrometer, 200 keV incident electrons, a collection semi-angle of 11 mrad and beam current of 2.5 nA; the collection time was 10 s for Carbon-K and Oxygen-K edges and 100 s for Silicon-K edge.

2.3.2 Effect of specimen x-ray absorption

A knowledge of film thickness enables the absorption of soft x-rays in each specimen to be estimated. We have done this based on linear absorption coefficients taken from Henke et al. (1982). We assume that Specimen C will be oriented so that boron layer is closest to the detector (on top, for a detector above the specimen plane) since this situation leads to less absorption of low-energy boron-K x-rays. In Figure 2.2, the percentage absorption p of the appropriate characteristic x-rays is shown for each element in each type of specimen, as a function of the angle between the specimen surface and the x-ray detector (the takeoff angle). The elevation angle of our detector is 24°, so a horizontal specimen corresponds to 24° takeoff angle. As the specimen is tilted towards the detector, the x-ray path lengths within the specimen decrease, leading to a fall in the fractional absorption.

As seen from Fig. 2.2, the calculated absorption of Si-K radiation is in all cases below 2% which can be neglected for practical purposes. This assumption allows a measured k-factor, k, to be corrected for specimen absorption using the simple formula:

$$k^* \approx (1 - p/100)\, k \qquad (2.3)$$

where

$$k = w\, [I_{Si}/ I_A] \qquad (2.4)$$

Here I_A and I_{Si} are the light-element and silicon-K intensities, both recorded from the calibration specimen, w is the weight fraction of the element (relative to silicon) as given in Table 2 and p is the percentage absorption of light-element x-rays, obtained from Figure 2.2. Since the calculated absorption is below 26% for all elements (see Fig. 2.2), a 20% error in p (due to error in thickness or absorption coefficient) would cause only a 5% change in the absorption-corrected value k*.

A correction for specimen absorption (to give k*) can then be made using Eq. (2.3), with calculated absorption factors taken from Figure 2.2.

Also known as zero-thickness k-factors, k* values are used by many workers in the field of EDX spectroscopy, since they have significance over a wider range of experimental conditions (for a given microscope accelerating voltage). They are derived by removing x-ray absorption effects by calculation (if the local thickness of the specimen is known) or by extrapolation of experimental data to zero thickness (Horita et al., 1987).

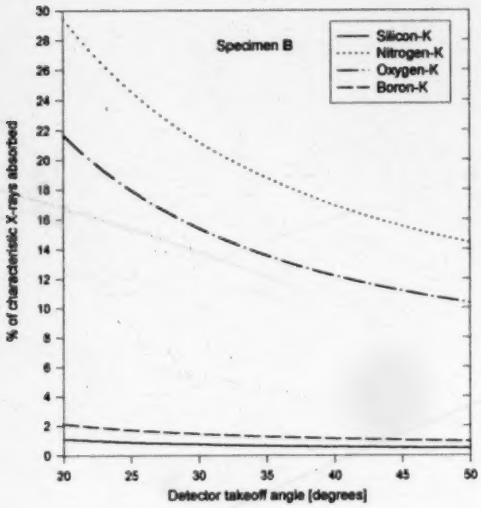

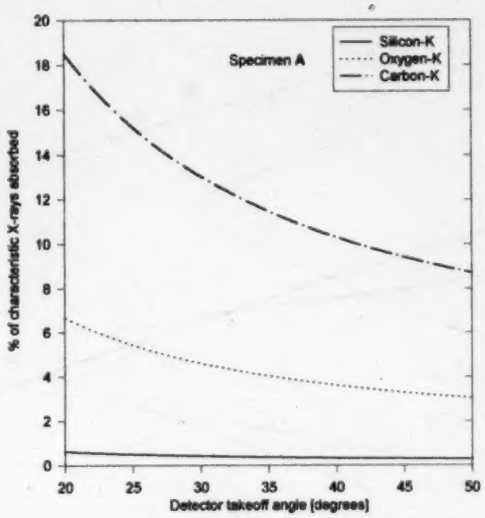

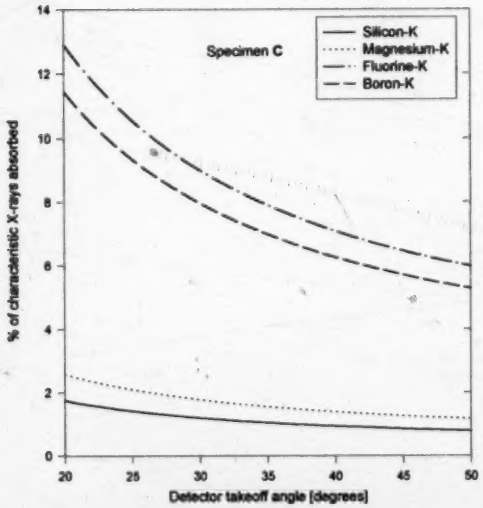

Figure 2.2. Percentage absorption of characteristic x-rays in the three calibration specimens, calculated as a function of detector takeoff angle for: (a) Specimen A; (b) Specimen B (with the boron layer nearest to the detector, absorption of Boron-K radiation is small); (c) Specimen C (the calculations assume that the silicon layer is furthest from the detector and the boron layer closest).

2.3.3 Film stability during storage and irradiation

A desirable property of any calibration specimen is that it remain essentially unchanged during storage. We have used EELS to measure the composition of the three types of specimen during storage in normal laboratory air, over a period of 15 months after preparation. The only significant change was that of oxygen in Specimen A, whose composition (relative to silicon) increased by about 7% over a 15-month period.

Another important consideration is that the specimen composition remain unchanged during the electron irradiation needed to collect an EDX spectrum with adequate statistics, typically 5×10^{-7} C (for example: 5nA beam current for 100 s, or an electron dose of $D \approx 10$ C/cm^2 with a 2μm-diameter incident beam). Although inorganic materials are generally more radiation-resistant than organic ones, some compounds (such as alkali halides) have efficient energy-conversion mechanisms which render them unstable in an electron beam (Hobbs, 1979).

Figure 2.3 shows EDX measurements of elemental ratios in the calibration specimens, as a function of exposure to 200keV electrons. In specimen A, the carbon/silicon ratio changed by less than 10%, even for an electron dose D of 10^5 C/cm^2 (a factor of 10^4 larger than that required to record an EDX spectrum from a 2μm-diameter area); the oxygen/silicon ratio remained stable up to 100 C/cm^2,

decreasing by 15% after D = 10^5 C/cm^2. In Specimen B, the nitrogen concentration appears stable; the oxygen content increased by about 15% at D = 10^5 C/cm^2, perhaps due to beam-catalysed reaction with traces of water vapour in the microscope vacuum. We used EELS to measure the stability of boron in Specimen C and found no variation, within experimental error.

Not surprisingly, the least beam-stable element is fluorine, which tends to be radiation-sensitive in both inorganic and organic compounds (Hobbs 1979, Ciliax et al. 1993). In Specimen C , a 10%wt decrease was observed for D $\approx$ 10 C/cm^2 at room temperature. As illustrated in Fig. 2.3c, this fluorine loss can be largely eliminated by cooling the specimen to 90 K, using a specimen holder cooled by liquid nitrogen. Even at room temperature, fluorine loss is insignificant and the EDX statistics are adequate provided the incident beam is defocussed to a diameter of 5 μm or more.

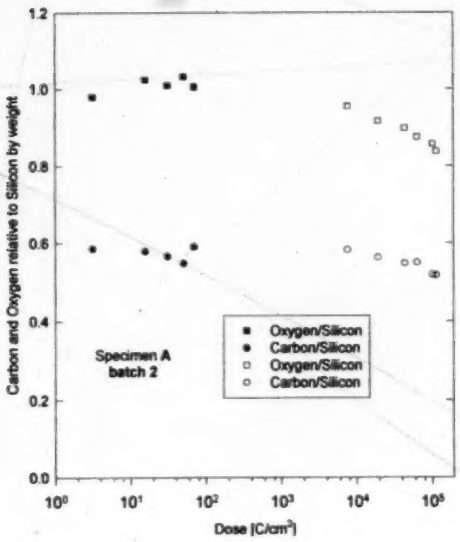

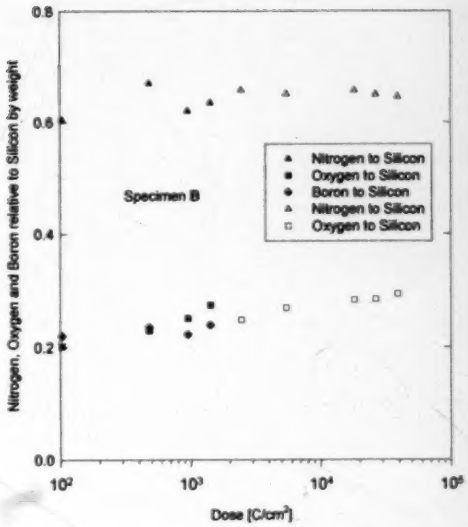

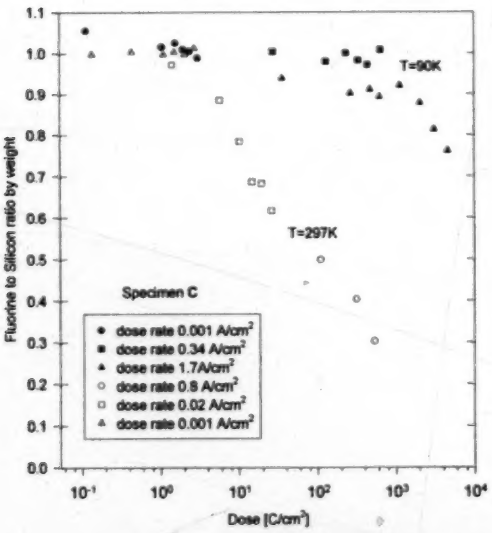

Figure 2.3. Light-element concentrations (relative to silicon) measured as a function of exposure to 200keV electrons for (a) Specimen A (square symbols Oxygen/Silicon, circle symbols Carbon/Silicon), (b) Specimen B (solid symbols measured by EELS, open symbols measured by EDX) and (c) Specimen C (open symbols measured with specimen at 297K, solid symbols at 90K).

2.3.4 Measurement of EDX k-factors

We have used the three calibration specimens to characterize the Noran high-purity germanium detector attached to our JEOL-2010 TEM. Energy-dispersive x-ray spectra recorded with a horizontal (untilted) specimen are shown Figure 2.4. In each case, the recording time was 100 s, the beam current was in the range 1 nA to 5 nA and the incident beam diameter was 2 μm.

Characteristic peaks arising from excitation of the copper support grid occur at around 950 eV (too weak to be visible in Figure 2.4) and 8000 eV, but do not interfere with the peaks of interest. The only substantial overlaps are those of the nitrogen and oxygen peaks obtained from Specimen B and those of oxygen and fluorine from Specimen C. We find that the use of a peak fitting routine, allows measurement of the individual peak intensities to an accuracy* of better than 5%.

The EDX k-factor for a particular element A (relative to silicon) was determined by integration (using nonlinear Marquardt-Levenberg fitting to a gaussian curve) of the measured K-emission intensity I_A and of the intensity I_{Si} of the silicon peak in the same spectrum, followed by application of Eq.(2.4).

Measured k* values for our detector are shown in Figure 2.5. EDX spectra were recorded both with a horizontal specimen (takeoff angle 24°) and with the

specimen tilted 20° towards the x-ray detector (takeoff angle 44°). The resulting k-factors, as determined from Eq.(2.4), differed by less than 10%, showing that x-ray absorption in these thin specimens is small. After correcting for this absorption using Eq.(2.3), the values of k* derived from zero-tilt and 20°-tilt measurements were within 1% of each other and are shown as single points on Figure 2.5.

Figure 2.5 also shows calculated k* values (Zemyan and Williams 1993 , Maher et al. 1981, Williams and Carter 1996). Points connected by dashed lines refer to an ideal detector; those connected by solid lines are for a modeled detector. In the ideal detector, x-rays are completely absorbed in the semiconductor diode and nowhere else, so that k* is simply a ratio of the x-ray emission cross sections. The modelled detector is based on the manufacturer's absorption curve for the Norvar window and a calculation of the absorption (Egerton and Cheng 1994, Zemyan and Williams 1993) in a 40nm aluminum front-contact film and a 60nm germanium dead-layer, using absorption coefficients given by Henke et al. (1982). Our measured k-factors are substantially less than those of the modelled detector, indicating that detector front-end absorption is less than expected and illustrating the value of determining k-factors by experiment rather than by calculation (Zemyan and Williams 1993, Williams and Carter 1996).

---

* Nonlinear Marquardt-Levenberg fitting to gaussian curve using Sigma Plot 2.0 was used to fit the experimental spectra, the accuracy of the fit was determined from the statistics of the fit.

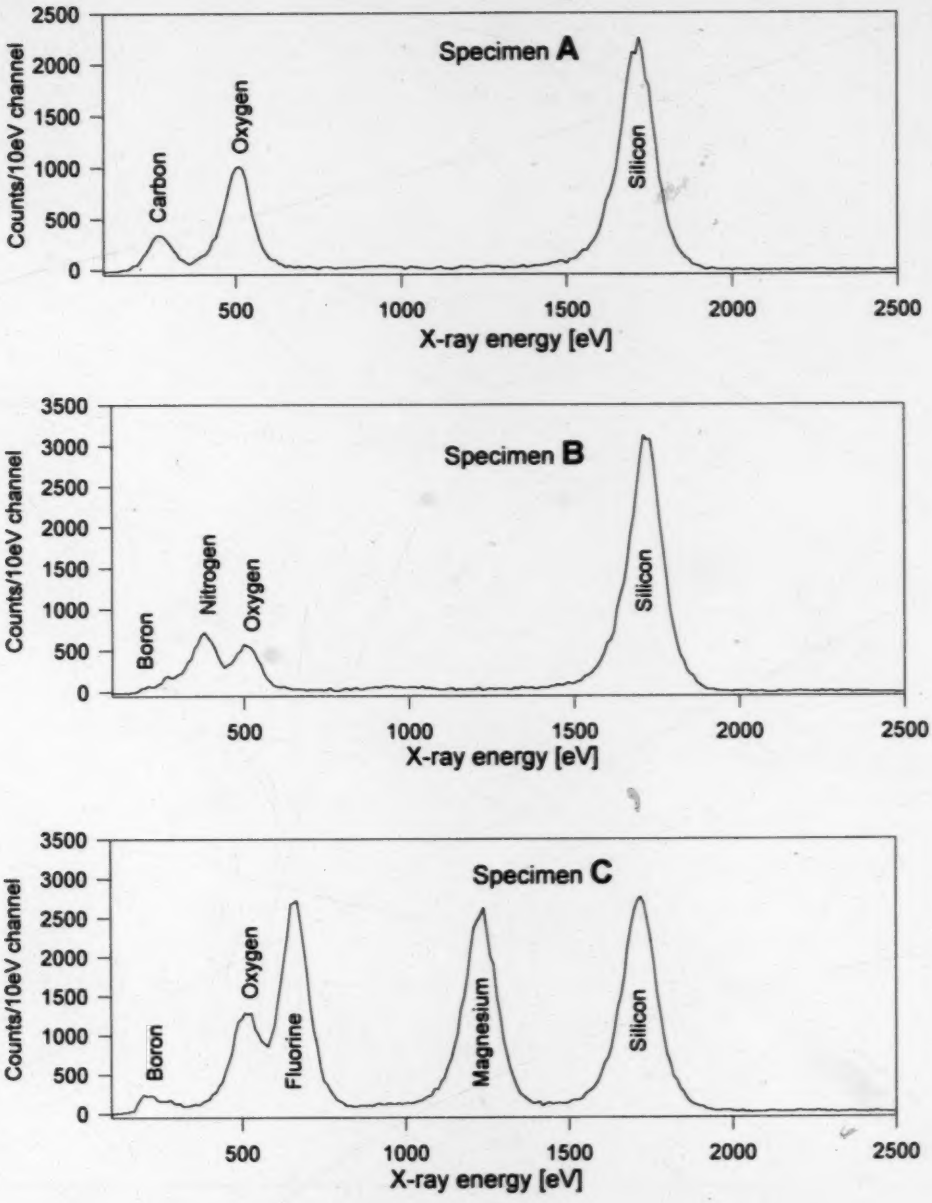

Figure 2.4. Typical EDX spectra recorded from the three calibration specimens, using a Noran high-purity germanium detector behind a Norvar atmospheric window, 200keV incident electrons and 24° takeoff angle, 100 seconds live time.

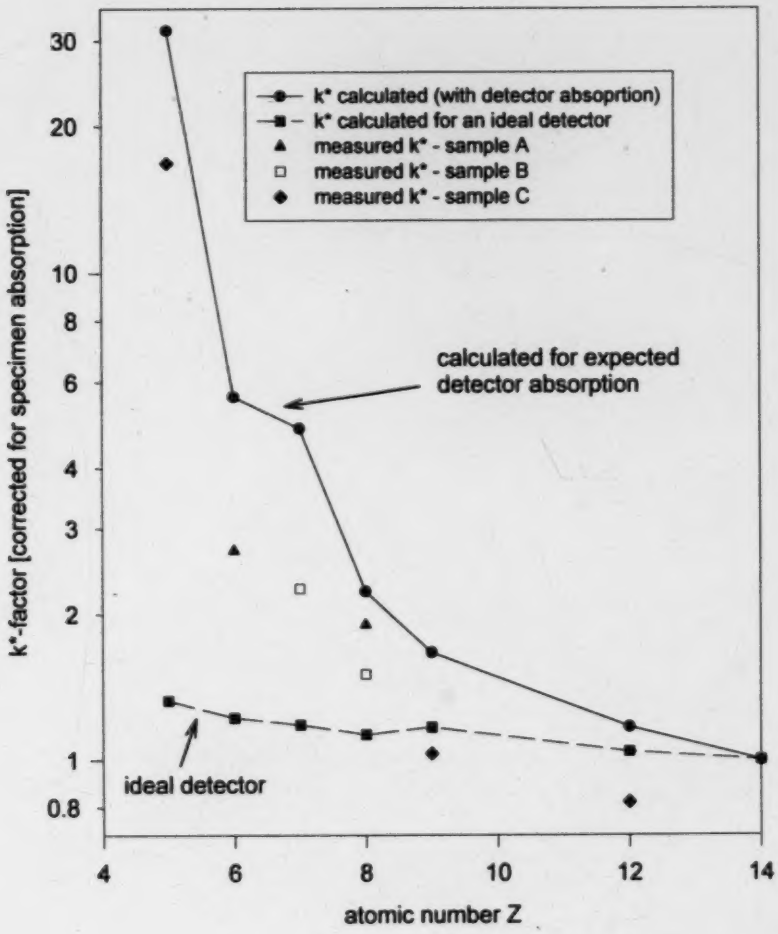

Figure 2.5. Zero thickness EDX k*-factors for the atmospheric-window Noran HPGe detector, measured using 200keV electrons, compared with calculated k*-factors which exclude (dashed lines) and include (solid lines) absorption in the detector window, front contact and dead layer.

If an ice or hydrocarbon layer gradually builds up on the detector crystal or its protective window, due to condensation of water vapour or hydrocarbons from the vacuum system, the measured k-factors will increase with time, in inverse proportion to the absorption factor of the corresponding element in the contamination layer. Figure 2.6 shows absorption factors calculated for water-layer thicknesses up to 1μm. As expected, the effect of icing is greatest for the low-energy boron x-rays and least for the silicon signal. The use of a nickel oxide test specimen provides a quantitative estimate of both the H_2O and carbon thickness (Egerton and Wong, 1995).

2.3.5 Specimen uniformity

We have used EDX spectrometry to measure element/silicon ratios in different grid squares across a 3mm-diameter specimen, and between different specimens prepared in the same deposition. There was no systematic change, within experimental error, as illustrated in Figure 2.7. From the scatter of the data points, we can estimate the statistical accuracy of the measurement of EDX intensity ratios to be ± 2% in these specimens. This figure gives an indication of the random error (precision) to be expected from the measurement of light-element k-factors; the absolute accuracy of the k-factors will likely be in the range 10% to 15%, determined largely by systematic errors involved in the measurement of elemental composition of the films by EELS (as discussed earlier).

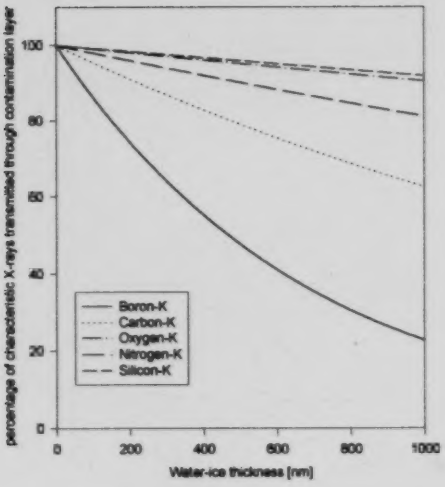

Figure 2.6 Calculated percentage absorption of characteristic x-rays in an H_2O-ice contamination layer.

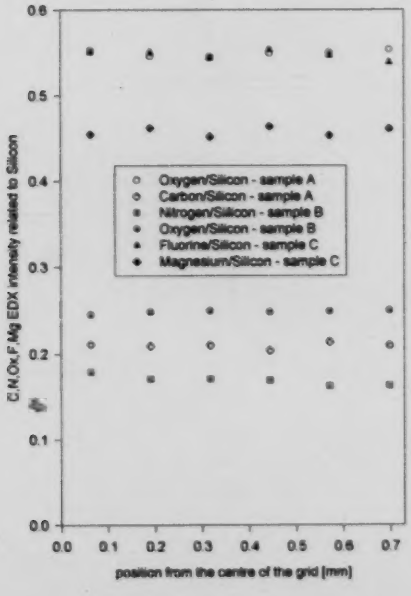

Figure 2.7. EDX intensity ratios measured as a function of distance from the center of the three calibration specimens. We detect no significant change in composition across the entire grid.

2.4 Conclusions

We have described the fabrication (see also Appendix 8.1) and characterization of amorphous thin-film specimens which contain light elements (B, C, N, O, F and Mg) in addition to silicon. For an analytical TEM equipped with a thin-window EDX detector, these specimens provide a convenient means of determining light-element k-factors. If the TEM is fitted with an electron energy-loss spectrometer, the specimens can be also used to check the EELS instrumentation and elemental-quantification procedures.

The specimens appear to be adequately stable during storage in air and (with reasonable precautions) under the electron-beam irradiation which is required for EDX analysis. We estimate that the k-factors determined using these calibration specimens will have an accuracy in the range 10% to 15%. While better accuracy would no doubt be desirable, it might not be of great practical benefit in view of the other uncertainties (background subtraction, correction for specimen absorption etc.) involved in light-element quantification by EDX spectroscopy.

2.5 References

Batson PE (1991) Studies of EELS $L_{2,3}$ absorption fine structure in thin silicon. *Microsc. Semicond. Mater. Conf. (Oxford 25-28 March 1991) IOP Conference Series No. 117.* Bristol: Institute of Physics, 55-62.

Ciliax BJ, Kirk KL and Leapman RD (1993) Radiation damage of fluorinated organic compounds measured by parallel electron energy loss spectroscopy. *Ultramicroscopy* 48, 13-25.

Cliff G and Lorimer GW (1975) The quantitative analysis of thin specimens. *J. Microscopy* 103, 203 - 207.

Egerton RF (1993) Oscillator-strength parameterization of inner-shell cross sections. *Ultramicroscopy* 50, 13 - 28.

Egerton RF (1996) Electron Energy-Loss Spectroscopy in the Electron Microscope, second edition. New York: Plenum Press.

Egerton RF, Cheng SC (1994), Characterisation of an analytical electron microscope with a NiO test specimen. *Ultramicroscopy 55, 43-54*

Egerton RF and Wong K (1995) The performance of analytical electron microscopes and EDX systems, measured with a nickel oxide test specimen. *Proc. Microscopy and Microanalysis 1995,* Bailey GW, Ellisman MH, Hennigar RA and Zaluzec NJ (eds.), 600-601.

Goldstein JI, Costley JL, Lorimer GW and Reed SJB (1977) Quantitative x-ray analysis in the electron microscope. *Scanning Electron Microscopy/1977* Vol. I, Johari, O (ed.). Chicago: IIT Research Institute, 315 – 324.

Hall, CR (1966) On the production of characteristic x-rays in thin metal crystals. *Proc. Royal Soc. London* A295, 140-163.

Hobbs LW (1979) Radiation damage in electron microscopy of inorganic solids. *Ultramicroscopy* 3, 381-386.

Henke BL, Lee P, Tanaka, TJ Shimabukuro RL and Fujikawa BK (1982) Low-energy x-ray interaction coefficients: photoabsorption, scattering and reflection. *At. Data Nucl. Data Tables* 27, 1 - 50. (see also http://cindy.lbl.gov/optical_constants/atten2.html)

Maher DM, Joy DC, Ellington MB and Zaluzec NJ, Mochel PE (1981) Relative accuracy

of k-factor calculations for thin film X-ray analysis. *Analytical Electron Microscopy 1981,* Geiss RH (ed.). San Francisco: San Francisco Press, 33 – 38

Malis T, Cheng SC and Egerton RF (1988) EELS log-ratio technique for specimen-thickness measurement in the TEM. *J. Electron Microscope Technique* 8, 193-200.

Rez P (1982) Cross sections for energy loss spectrometry. *Ultramicroscopy* 9, 283-288.

Skiff WM, Carpenter RW and Lin SH (1987) Near edge fine structure analysis of core shell excitonic absoprtion edges in silicon and it's refractory compounds with the use of electron energy microspectroscopy. *J. Appl. Phys* 62, 2439-2449.

Steel EB, Newbery DE and Pella P (1981) Preparation of thin-film glass standards for analytical electron microscopy. *Analytical Electron Microscopy 1981, ed. R.H. Geiss. San Francisco: San Francisco Press,* 65-70.

Williams DB (1993) Light element microanalysis and imaging. *Quantitative Microbeam Analysis,* A.G. Fitzgerald, B.E. Storey and D. Fabian (eds.). Bristol: Institute of Physics, 169-177.

Williams DB and Carter CB (1996) Transmission Electron Microscopy: A Textbook for Materials Science. New York: Plenum Press.

Zemyan SM and Williams DB (1993) Variables in calculated k-factors for analytical electron microscopy, *Microbeam Analysis* 2, S182-S183.

Chapter 3

Concentration Limits For the Measurement of Boron By Electron Energy-Loss Spectroscopy and Electron-Spectroscopic Imaging

(Yimei Zhu, Ray F. Egerton, M. Malac, submitted to Ultramicroscopy)

3.1. Introduction

In recent years, there have been many attempts to probe and extend the sensitivity limits of elemental analysis by electron energy-loss spectroscopy (EELS). Some studies have concentrated on detection of the smallest detectable mass. For this purpose, the electron beam must be focussed into as small a diameter as possible; by use of a (scanning) transmission electron microscope (S)TEM equipped with a field-emission electron source, detection of just a few atoms has been achieved (Krivanek et al 1991, Leapman and Rizo 1999).

Other studies have focussed on detection of low elemental concentrations; although TEM electron optics are used to confine the analysis to a small area, the incident-beam diameter is less important than collection of an adequate signal in the presence of a large spectral background. The relatively large L-edge cross sections of sulphur and phosphorus allow detection of low concentrations (~100 parts per million or ppm) of these elements in biological tissue (Wang et al 1992). Transition metals and rare-earth elements represent another favourable case, since their L or M ionization edges provide sharp (white-line) peaks at the ionization threshold; using a

field-emission source to provide good energy resolution, Leapman and Newbury (Lepman and Newbury 1993) demonstrated that concentrations below 100 ppm can be detected. In the case of carbon in iron, however, the detection limit has been calculated and measured to be no better than 1% (10,000 ppm) (Liu and Brown 1982, Natusch et al 1999).

Boron in silicon at the 1% level was easily visible in a second-difference STEM spectrum (Egerton 1991) while 0.5% could be detected in Ni_3Al, using elaborate correction for gain variations within the photodiode detector (Boothroyd et al 1990). Spatial mapping of boron is of particular interest for boron neutron-capture therapy (BNCT) (Gavin et al 1997, Coderre 1999), a cancer-therapy technique in which malignant tissue is injected with boronophenylalanine fructrose (BPA-F) and irradiated with thermal neutrons; the ^{10}B atoms then transform into energetic ^{4}He and ^{7}Li (penetration range 5 μm and 9 μm respectively), destroying the surrounding tissue by damaging the nucleus (1μm in diameter) of each cell (typical diameter 9 μm). Ion microscopy (SIMS) studies (Smith et al 1996) have indicated that rat-tumor tissue takes up about 3.5 times more boron (99 μg/g tissue, or approximately 100 ppm) than normal tissue, so BNCT spares normal tissue to some degree. There is also evidence that the boron is segregated within each cell, in which case local concentrations could considerably exceed 100 ppm, particularly in dried tissue samples where 80% of the mass has been removed during specimen preparation. Hence, there is a need for boron mapping with sub-micrometer spatial resolution and a sensitivity of a few hundred ppm, or better.

3.2. Experimental

The aim of the present study was to determine the measurement sensitivity of EELS for boron in a carbonaceous specimen. To avoid the problem of radiation damage, which may occur in biological tissue, we employed test specimens consisting of a very thin layer of boron deposited onto a carbon film supported on a TEM grid. The thickness of the boron and carbon layers could be controlled and measured during the fabrication process. A total specimen thickness of around 50nm was considered near-optimum for boron-edge spectroscopy at 200-300 keV; thinner specimens would provide less boron signal while thicker ones would result in excessive plural scattering, increasing the spectral background at the boron K-edge and reducing the edge visibility. BPA-stained tobacco mosaic virus (TMV) samples were used to estimate the radiation sensitivity of the BPA as well as to map the boron distribution.

Three types of test samples were prepared. First, thin-film specimens were made by electron-beam evaporation of carbon and boron in a diffusion-pumped vacuum system (base pressure below 5×10^{-7} torr). Film thickness was measured during deposition by a quartz-crystal thickness and rate monitor. Boron thickness below 1 nm required the use of an atomic-beam attenuator: a rapidly spinning aluminum disk with a 5-degree sector cut out, so that the flux reaching the carbon layer was reduced by a factor of 100 compared to that monitored by the quartz crystal. The boron/carbon films were separated from the cleaved mica substrates by slow immersion below the surface of deionized water, then mounted on 400-mesh copper

TEM grids. Such samples have a well known boron concentration and good uniformity of the boron distribution.

Second, to provide test samples with non-uniform boron distribution boron was electron-beam evaporated onto a 50nm thick carbon film. The carbon films were sprinkled with alumina particles and mounted at an oblique angle during the boron deposition (about 75° between the substrate normal and incoming flux of boron - atoms). Since electron beam evaporation at low pressures is a "line of sight" process the alumina particles provide a shadow where no boron is deposited. However, the boron concentration in samples deposited at an oblique angle is less precisely known than in the first type of sample, since a small deviation in the angle at which boron is deposited (due to slight wrinkling of the substrate) results in appreciable changes in boron concentration. Because the boron spatial distribution in such samples is intentionally non-uniform, they are suitable for boron mapping experiments.

Third, samples simulating biological tissue were prepared by drying a water solution of BPA on (2nm thick) carbon coated grids. Tobacco mosaic virus (TMV) added into the solution provides an internal size standard and creates areas with thicker deposits of dried BPA. The high boron content in BPA makes the BPA stained TMV samples ideal for boron mapping experiments on biological samples.

Specimens were examined at room temperature in two instruments. Instrument A is a JEOL-2010 TEM fitted with a LaB_6 electron source and Gatan 666 PEELS

spectrometer (Egerton et al 1993). Instrument B is a JEOL-3000F equipped with a field-emission source and Gatan imaging filter (GIF). As an electron detector, the PEELS system uses a one-dimensional (linear) photodiode array, fibre-optically coupled to an yttrium aluminum garnet (YAG) scintillator. The GIF system uses a two-dimensional (area) charge-coupled-diode (CCD) array, preceded by a powder-phosphor screen (for microscopes above 200kV); energy-loss spectra are obtained by integrating horizontal rows of diode elements (in the non-dispersive direction) over a user-determined range[†].

Spectra were acquired mainly in TEM-diffraction mode, a collection angle of 10mrad being selected by an objective aperture or by the spectrometer-entrance aperture. We used an incident electron energy of 200 keV in instrument A and 300 keV in instrument B. Employing an energy dispersion of 0.3 eV/channel allowed the boron-K and carbon-K edges to be recorded simultaneously. Initial elemental quantification was done by standard power-law background subtraction at the B and C K-edges, followed by integration of the core-loss intensity (over Δ = 50eV energy window) to obtain the core-loss intensities I_K^B and I_K^C. The formula:

$$N^B/N^C = (I_K^B/I_K^C)\,(\sigma_K^C/\sigma_K^B) \qquad (3.1)$$

[†] A detailed description of PEELS and GIF systems can be found in Ray Egerton's book (Egerton 1996) and in a book by David Williams (Transmission electron microscopy; a textbook for material science published by Plenum Press in 1996).

was used to obtain the ratio N^B/N^C of the areal densities of boron and carbon. K-ionization cross sections were calculated by running the SIGMAK3 computer program [13] which gives similar values to the Hartree-Slater cross sections used in the latest version of the Gatan EL/P program [14]. For $\Delta = 50$ eV and $\beta = 10$mrad, we obtain $(\sigma_K^C/\sigma_K^B) = 0.432$ for $E_0 = 300$ keV and $(\sigma_K^C/\sigma_K^B)=0.423$ for $E_0 = 200$ keV.

For weak ionization edges, the power-law subtraction provided by the Gatan EL/P program is sometimes inadequate: after background subtraction, the boron K-edge intensity is seen to fall off too rapidly or not rapidly enough. We circumvented this problem by mis-calibrating the energy-loss axis, so that the K-edge shape appeared reasonable after power-law subtraction. This procedure was more necessary for the PEELS system; power-law extrapolation seems to work well in the GIF provided care is taken to avoid stray electrons or photons reaching the CCD array. The width of energy window for background fit below boron K-edge was between 10 eV and 20 eV positioned between 160 eV and 180 eV. Background below carbon K-edge was fitted using 30 eV wide window starting 48 eV below the carbon π^*-peak. Typical background fit for boron K-edge can be seen in the inset of Figure 3.1. Additionally, samples with nominal boron concentration between 2% and 0.006% were analysed to ensure correct data-processing procedures.

3.3. Results and discussion

3.3.1 Measurement of boron and carbon ratio

Table 3.1 shows boron to carbon ratios obtained from different areas of the same specimen prepared by electron-beam evaporation of boron onto 50 nm carbon, measured with the two instruments. There is reasonable agreement between the two instruments and between different areas, confirming that the sample is uniform. There also is a good agreement between TEM diffraction mode and image mode; however, diffraction mode appears to give better quality spectra (carbon-edge jump ratio ~10 rather than ~2.2). The variation in the N^B/N^C ratio in table 3.1 can be attributed to statistical variation between measurements. This is due to combined effect of error in background fit for both boron and carbon edges, beam shot noise and in case of instrument A gain variations have to be taken into consideration. The boron to carbon ratio measured using instrument A is $N^B/N^C = 0.0104 \pm 0.0065$, corresponding value using instrument B is $N^B/N^C = 0.016 \pm 0.009$.

The fine structure of the boron K-edge, a sharp threshold peak followed by a broad peak 9 eV beyond the threshold, is characteristic of a boron compound (likely an oxide) rather than boron metal. Oxidation should not affect the elemental quantification but could conceivably reduce the radiation resistance, allowing mass loss of boron at high dose. In fact, we found no measurable decrease in boron fraction after doses as high as 2.5×10^4 C/cm^2 at dose rates between 5 and 10 A/cm^2 at incident electron energy 200 keV.

Instrument	mode	I_K^B [counts×10^6]	I_K^C [counts×10^8]	N^B/N^C
PEELS at 200kV	D	2.87	1.24	0.010
PEELS at 200kV	D	4.21	1.56	0.0114
PEELS at 200kV	D	1.8	0.76	0.01
GIF at 300kV	D	19.1	6.37	0.013
GIF at 300kV	D	18.4	6.5	0.0122
GIF at 300kV	D	6.39	2.46	0.0112
GIF at 300kV	D	6.65	2.44	0.0116
GIF at 300kV	D	17.2	7.33	0.0101
GIF at 300kV	D	3.09	1.28	0.0104
GIF at 300kV	I	0.53	0.187	0.0123
GIF at 300kV	I	0.385	0.142	0.0117

Table 3.1: Quantification of a boron test specimen by EELS in TEM diffraction mode (D) and image mode (I). The first three measurements were made using instrument A (JEOL-2010 at University of Alberta), the rest using instrument B (JEOL-3000F at Brookhaven National Laboratory).

Figure 3.1 shows a background-subtracted boron K-edge and the carbon K-edge (inset) measured from a specimen consisting of a 50nm carbon layer and a 0.1nm boron layer (7.2 nm on the rate-monitor crystal, 5/360 attenuation factor for the carbon substrate), giving an expected atomic ratio of 0.2% boron. The ratios measured on the same sample in both instruments are shown in Table 3.2; the spectra collected in the instrument B (GIF at 300kV) give average boron fraction N^B/N^C=0.0021±0.0002 and the spectra collected in instrument A (PEELS at 200kV) give average boron fraction N^B/N^C= 0.0019±0.0005 .

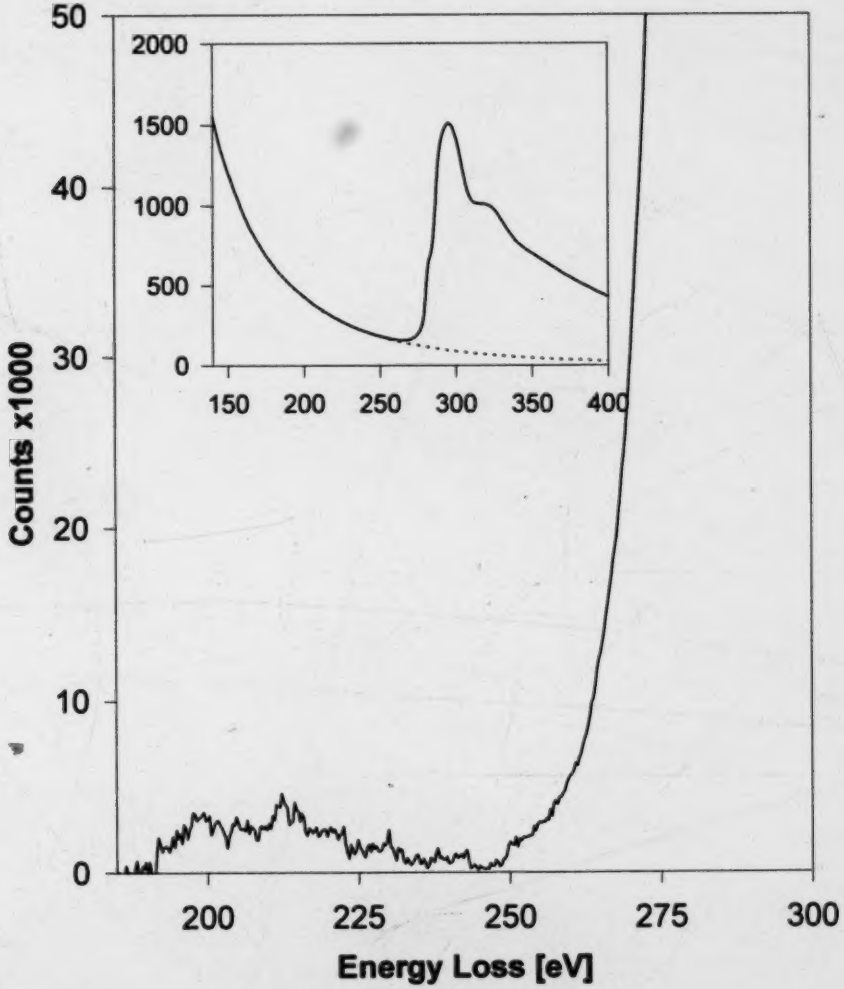

Figure 3.1 Background-subtracted boron-K edge and original spectra (inset) of a sample with nominal 0.2% boron concentration. The boron to carbon ratio was determined to be $N^B/N^C = 0.0021 \pm 0.0002$ using the instrument B. The solid line in the inset is the original spectrum, dotted line is corresponding background fit under the boron-K edge.

Instrument	Acquisition time [s]	I_K^B [counts] [counts×10^6]	I_K^C [counts] [counts×10^8]	N^B/N^C
GIF at 300kV	6.25	4.60	9.84	0.0020
GIF at 300kV	6.25	5.07	9.68	0.0023
GIF at 300kV	12.5	9.94	2.02	0.0021
GIF at 300kV	1.25	8.06	1.92	0.0018
PEELS at 200kV	50	1.10	2.91	0.0016
PEELS at 200kV	100	0.909	2.65	0.0015
PEELS at 200kV	100	0.967	2.62	0.0016
PEELS at 200kV	100	1.46	2.59	0.0024
PEELS at 200kV	100	0.918	2.46	0.0016
PEELS at 200kV	100	1.32	2.09	0.0027

Table 3.2: Quantification of a specimen containing 0.2% boron (0.1nm B on 50nm C) using the GIF at 300kV and PEELS at 200kV, both in diffraction mode with 1μm-diameter incident beam and 10mrad collection semiangle.

The beam current in the instrument A (JEOL 2010 with PEELS) was measured to be 20nA using solid-state electrometer connected to the drift tube of the spectrometer. For the purpose of the beam current measurement the spectrometer was set to 180kV while the microscope was operated at 200kV, so that the drift tube of the spectrometer acts as a Faraday cup.

The beam current in the instrument B (JEOL 3000F) was obtained from the TEM screen current, calibrated by previous measurements using a Faraday cup. With a gun emission current 156 μA, the current was up to 8 nA for the 150 μm condenser aperture, 0.67 nA for the 70 μm condenser aperture and 0.36 nA for the 50 μm condenser aperture. Since the 70 μm condenser aperture was used in most of the quantitative measurements, the beam current can be taken as 0.7 nA for the

calculations of boron detection limit. For the mapping of boron distribution using the GIF, the 150 μm condenser aperture was used and therefore the beam current used in the calculations is 8 nA.

3.3.2 Detection limit for an ideal detector

For a perfect electron detector (detector quantum efficiency, or DQE = 1), the minimum-detectable atomic fraction (MAF), determined by electron statistics, is given (Egerton 1996, page 105) by:

$$MAF = (SNR / \sigma_k) (h\, e\, \sigma_b / N_t)^{1/2} (I\, T)^{-1/2} \qquad (3.2)$$

Here SNR is the minimum-acceptable signal/noise ratio[‡], h is a statistical factor associated with separating the core-loss signal (cross section σ_k) from the non-characteristic spectral background (scattering cross section σ_b), e is the electronic charge, N_t is the total number of atoms (all chemical species) per unit area of specimen, I is the incident-beam current and T is the recording time. Note that MAF depends on the total charge (beam current times acquisition time) used for measurement and is independent of the incident-beam diameter (spatial resolution).

For our test sample consisting mainly of 50 nm of carbon, the areal density $N_t = (\rho t/Au) = 4.5 \times 10^{17}$ cm^{-2} (where A is atomic mass number, ρ is density in g/cm^3, t is thickness and u is atomic mass unit). For 300keV incident energy, 10mrad collection

angle and 50eV integration window, the cross section for boron K-shell ionization is $\sigma_k = 6940 \times 10^{-24}$ cm^2 (using SIGMAK3 for the boron K-edge). The cross section for the non-characteristic background is $\sigma_b = 0.22 \times \sigma_k = 1530 \times 10^{-24}$ cm^2, estimated from measurements of the non-characteristic background in typical spectra collected from the 50nm carbon samples with 0.2% boron.

The minimum-atomic detectable fraction (MAF) can be then calculated taking SNR = 10 (for 10% measurement accuracy), h = 10 [13, p.297], integration time T = 6 s and beam current I = 0.7 nA (typical values, as discussed above). For the above values (typical conditions in instrument B), Eq.(1) gives MAF = 0.0017. In other words, about 0.17% of boron should be measurable with 10% accuracy. Experimentally, we achieved about this accuracy at a measured concentration of 0.2%. Since the MAF is independent on the incident beam diameter, it should be possible map 0.2% boron in STEM by acquiring spectra from each point with resolution as good as allowed by the radiation damage (for beam sensitive samples) of the sample or by spherical aberration of the objective lens (Egerton 1999).

3.3.3 Boron mapping using EFTEM mapping

Energy Filtered Transmission Electron Microscopy (EFTEM) offers the possibility of mapping the spatial distribution of an element of interest, by recording one or more

‡ SNR can be roughly interpreted as measured signal divided by the statistical error of the measurement (Egerton 1996, page 106), thus SNR = 10 roughly corresponds to 10 % error in a measurement. For detection (rather than quantification) of an element a value of SNR = 3 is generally considered adequate.

pre-edge images (for energy losses just below a characteristic edge) and a post-edge image. The pre-edge data enable allowance to be made for the non-characteristic background on which the core-loss intensity is superimposed.

The above calculation of detectable atomic fraction (Eq. 3.2) can also be applied to elemental mapping, to determine the minimum area (n × n pixels) in which boron can be detected. Here the incident-beam current I is spread over the whole image, consisting of N × N pixels. However, the number of pixels can be reduced by binning n pixels together, in which case the current within a binned n^2-pixel area is $(n/N)^2$ I . Formula (3.2) can then be rewritten in the form:

$$MAF = (SNR / \sigma_k) (h e \sigma_b / N_t)^{1/2} (I T)^{-1/2} (N/n) \qquad (3.3)$$

Taking typical values: I = 8 nA, SNR = 3 (for boron detection rather than quantification), h = 10 as before, N = 1024, boron-K ionization cross section $\sigma_k = 2170 \times 10^{-24}$ cm^2 for an integration window (width of the energy-selecting slit) Δ = 10 eV, image recording time T = 240 s and n =16, Eq. (3.3) gives MAF = 0.3 %. In other words, it should be possible to map 0.3% variations in boron concentration when 16x16 pixels are combined into one pixel.

Instrument B (JEOL 3000F fitted with GIF) was used for the experiment. Figure 3.2a is the zero-loss filtered image (an image formed exclusively by elastically

scattered electrons) of an area with an alumina particle (black) and the shadow (bright band) of the particle formed during boron deposition. The boron map in Fig. 3.2b was obtained with acquisition time T = 240s, beam current I=8 nA and no objective aperture (100mrad collection semiangle). After acquisition, the boron image was software-binned 1:16 to reduce the beam shot noise, compressing the original 1024×1024 pixels to 64×64pixels. The non-characteristic background was subtracted using binned pre-edge and post-edge images. To calibrate absolute boron concentration (y-axis in figure 3.2c), we measured the boron concentration in the shadowed area (bright band in figure 3.2a) and just outside this area, using image-mode spectroscopy with a collection semiangle of 10mrad. The size of a binned pixel depends on the microscope magnification and on the magnification of the Gatan Image Filter. Using independent calibration of the magnification, we estimate size of each binned pixel in figure 3.2b to be 66 nm. A boron profile (histogram) taken along the white line in figure 3.2a is shown in figure 3.2c; it reveals that the difference in boron concentration between the shadowed and unshadowed areas is about 0.5%. In other words, Fig. 3.2b is map showing variations of boron concentration as little as 0.5%. Although this value is in good agreement with the calculation above, the boron map and histogram in figure 3.2 should be considered semi-quantitative rather than quantitative, due to uncertainties in subtraction of the non-characteristic background (which cannot be directly observed in EFTEM images).

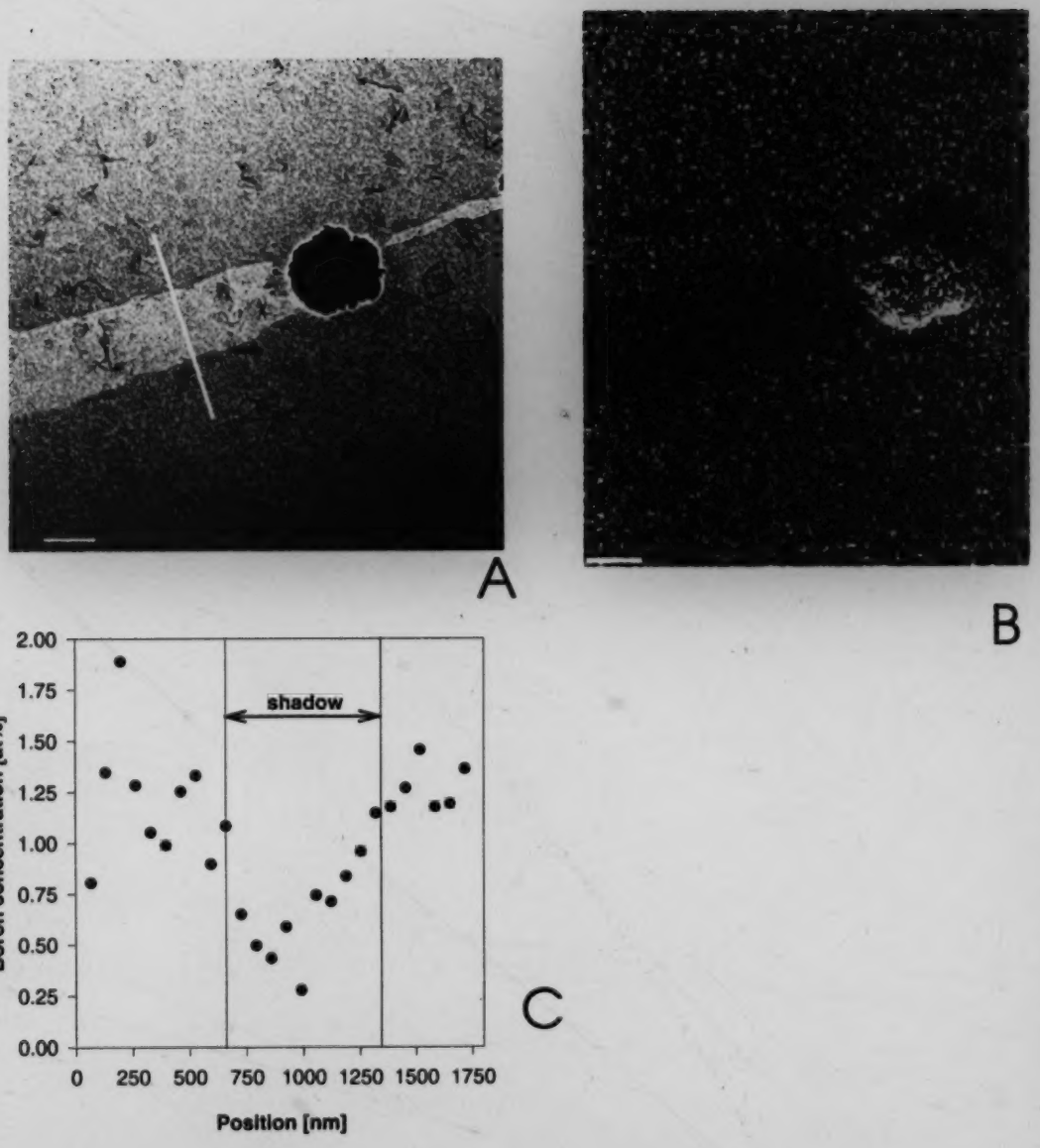

Figure 3.2. Boron mapping of the shadow-masked non-uniform (boron on 50nm carbon) sample. (a) Zero loss filtered image; (b) corresponding thickness-normalized boron map; (c) histogram of boron counts along the white line in (b). The width of the line scan depicted in the histogram in (c) is one pixel. The scale bar corresponds to 500nm.

3.3.4 Radiation damage and boron mapping of the TMV samples

Radiation damage to TEM samples is a serious concern and in many cases can limit the achievable spatial resolution (Egerton 1999). The measurements shown in Table 1 involved a radiation dose of the order of 0.1 C/cm^2. In some organic materials, this dose would cause extensive mass loss, but this may not be so for a dry sample containing mostly carbon and boron.

The biological test samples, containing Tobacco Mosaic Virus (TMV), prepared from a water solution of BPA were used sample to determine the mass-loss radiation sensitivity of BPA. Figure 3.3 shows the dose dependence of boron and carbon depletion in BPA at room temperature, with 300keV incident-electron energy and a dose rate of 0.26 A/cm^2. From the slopes of the lines Fig. 3.3, the characteristic dose is estimated to 1830 ± 40 C/cm^2 for carbon removal and 1300 ± 400 C/cm^2 for boron removal from BPA. Knowing the characteristic dose for boron removal allows us to estimate the smallest diameter d_{min} in which boron can be detected, if limited by radiation damage (Egerton 1999):

$$d_{min} = 3.3\,(f\sigma_k)^{-1}\,(he\sigma_b)^{1/2}\,(\eta D N_t)^{-1/2} \qquad (3.4)$$

This equation predicts d_{min}= 7 nm for detection of 0.2% of boron, taking σ_k = 6940×10^{-24} cm^2 for the boron K-shell cross section (integration window Δ = 50eV), background cross section $\sigma_b = 0.22(\sigma_k) = 1530\times10^{-24}$ cm^2, detector quantum efficiency η = 0.5 and background–extrapolation parameter h = 10. At a dose rate 0.3A cm^{-2}, however, the required acquisition time would be 83 minutes, so in practice the detection limit (d_{min}) will likely be determined by the specimen drift.

Another practical problem is the presence of phosphorus, whose L_1 edge is at the same energy as the boron K-ionization edge. Tissue contains about 0.1% phosphorus overall, and about 1% in each cell nucleus. Using a hydrogenic approximation, we find the L_1 cross section to be about 40% of that for boron K-ionization. If the boron concentration is 100 ppm, the integrated boron signal I_K^B will be only about 25% of the P-L_1 signal outside the cell nucleus, and only 2.5% within the nucleus. Outside the nucleus, *variations* in boron concentration might still be directly detectable from EFTEM elemental mapping, provided the phosphorus concentration was uniform. If not, quantification of the phosphorus distribution via the P-L_{23} edge might be necessary. If the boron is segregated into sub-micrometer granules, the presence of phosphorus may not be a problem, since the boron signal could well exceed that of phosphorus at a granule. The presence of the phosphorus P-L_{23} in biological samples may result in additional difficulties in background extrapolations under the boron K edge.

An additional problem associated with boron measurement in real tissue is that of specimen preparation without loss of boron. Wet tissue sections may have to be about 250nm thick in order to give an equivalent-carbon thickness of 50 nm after removal of water.

Figure 3.4a is a zero-loss image of three tobacco mosaic viruses, acquired in EFTEM mode using instrument B. Figure. 3.4b is a boron map of the same area, acquired at a beam current I = 2.1 nA , acquisition time T = 30 s, binning factor $n = 4$ and energy-selecting slit width $\Delta = 10$ eV. Figure 3.4c is a boron-count profile, measured along the white lines in Figure 4a, and indicating an increase in boron signal in regions corresponding to the positions of TMV (see insets in Figure 3.4c). Providing the non-characteristic background subtraction is correct, the number of boron atoms per (binned) pixel N^B (in units of atoms/cm^2) can be estimated using:

$$N^B = I_K / (\sigma_k \, I_{low}) \tag{3.5}$$

Here σ_k is the ionization cross section for the appropriate energy-selecting slit width and collection semiangle; I_K is the number of counts per pixel in the background-subtracted core-loss image; I_{low} is the total number of counts per pixel in an unfiltered image recorded (for a thin sample) with the same integration time T and the same binning n. Using the formula (3.5) we estimate the areal density (number of boron atoms per unit area) in the figure 3.4b to be approximately 3×10^{17} boron

atoms/cm^2 (or about 3000 boron atoms per pixel) in the vicinity of the tobacco mosaic viruses.

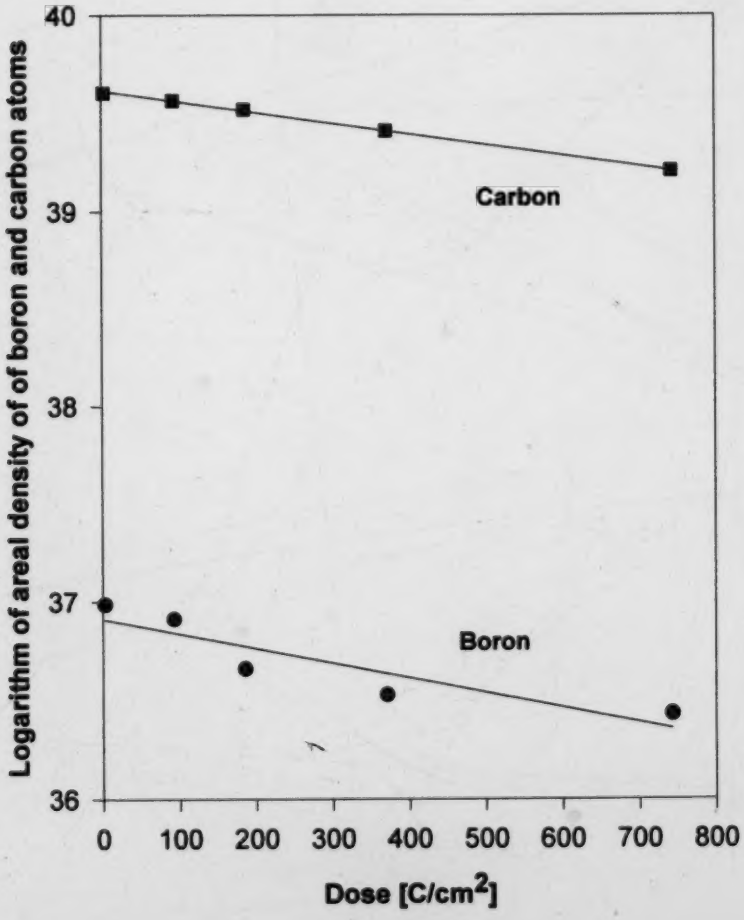

Figure 3.3. Radiation sensitivity of BPA at room temperature, measured using 0.3A/cm^2 of 300keV electrons, irradiated diameter 1 μm. The y-axis is calibrated in units of natural logarithm of areal density of boron (circular symbols) and carbon atoms (square symbols).

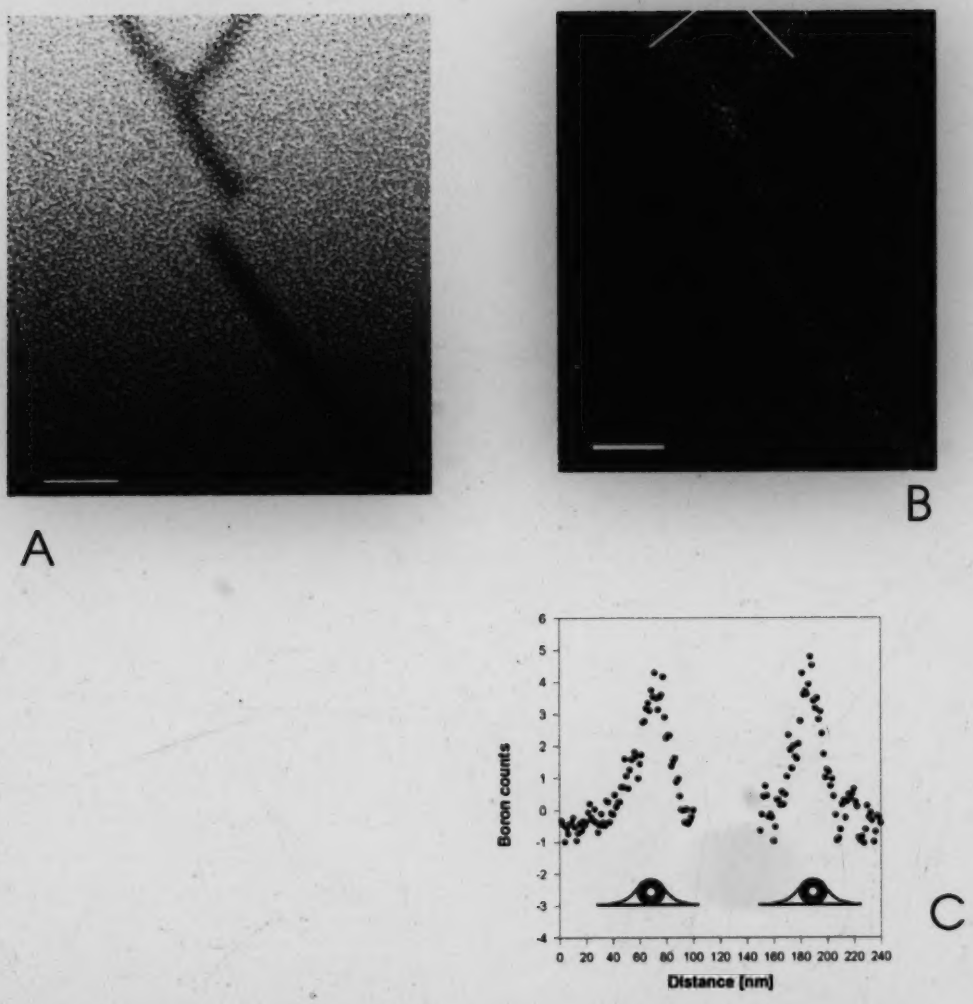

Figure 3.4. Boron mapping in the BPA-stained tobacco mosaic virus (TMV) sample. (a) zero-loss filtered image; corresponding thickness-normalized boron map; (c) histogram of boron counts (from the boron map) along the white lines in (b); inset shows schematically the position of the TMV and BPA meniscus. The line scan in (c) is an average over twenty pixels. The scale bar corresponds to 50 nm.

3.3.5 Comparison of GIF and PEELS systems

Our experience with the two types of instrumentation suggests the following comments.

The PEELS system has a sensitivity of about 25 incident electrons per count and the electron-beam shot noise with the output almost saturated (16000 counts/channel) is $(25 \times 16000)^{1/2}/s = 126$ electrons, since the interchannel smoothing factor s is about 5 (Egerton 1996, p.105). Because the readout noise is about 60 incident electrons per element, the readout and shot noise are roughly matched (within a factor of two). In other words, the sensitivity is not far from optimum, in terms of detector noise performance (DQE).

The GIF system has the advantage of a two-dimensional detector (CCD array) which allows automatic and accurate gain normalization. Through such normalization, variations between individual diode elements (and in the scintillator screen and fiber optics) are largely eliminated, improving the DQE (Egertn 1996, p.107) and allowing weak (<1%) modulations of the energy-loss intensity to be detected. For 100-200keV microscopes, a YAG screen is used, resulting in about 1 count per incident electron; the readout noise is around 1.5 counts rms, so the device has almost single-electron sensitivity. At full output, the beam shot noise is $(16000)^{1/2} = 126$ electrons and shot noise predominates over readout noise. For a 300keV TEM, the GIF uses a phosphor

screen which gives about 10 counts per incident electron; the device is single-electron sensitive and shot noise is predominant.

For spectroscopy, the GIF produces a line spectrum and the outputs of (typically) 200 to 500 elements are electronically added over a user-defined range. Because of the high sensitivity (250 times greater than PEELS) the output easily saturates, especially since electron intensity falls off in the y (non-dispersive) direction so that central ($y \sim 0$) diodes saturate before the others. Care has to be taken since the diode saturation level (16384 counts per pixel) applies to the counts per pixel in the raw data, before dark current subtraction; the dark-current level can be as much as several thousand counts per pixel for prolonged integration time. A further result of the y-variation of intensity is that the saturation effect in the spectrum is more gradual than in the PEELS system (where it is seen to be abrupt), making the saturation of central-diode elements less easy to detect. Saturation of the array becomes even more of a concern when spectra are acquired in diffraction mode, since the falloff in intensity in the y (non-dispersive) direction is faster than for spectra is acquired in image mode.

To improve the shot-noise statistics, the recording time should be made as long as possible. Because of CCD saturation, this cannot be done by using a long (> 0.5 sec) integration time per readout; instead, many readouts must be accumulated in computer memory. Unfortunately, the transfer time (from the CCD array to the EL/P program) is about 2 seconds, so a 1-minute acquisition may contain only 10 s of

recording time. Longer acquisition times introduce the possibility of spectrum and specimen drift, as well as radiation damage of the specimen.

The above comments apply mainly to spectroscopy mode and spectrum imaging in STEM mode. The following remarks apply to energy filtered imaging and elemental mapping using EFTEM images. When a weak inner shell ionization edge is mapped in EFTEM mode (such boron in our test sample in Figure 3.2), most of the intensity within the pre-edge and post-edge regions comes from the non-characteristic background. The count rate per (unbinned) pixel can be low and often a prolonged acquisition time (as high as several hundred seconds) must be used to obtain adequate statistics for edge detection. As in case of spectroscopy, the number of readouts of the array should be minimized by collecting the highest possible number of counts per readout, limited by saturation of the array. This also helps to minimize the number of primary electrons wasted (and associated radiation damage) while data is being transferred out of the array. However, long acquisition times require caution when collecting the dark current reference images, to avoid contamination by stray electrons and photons within the GIF. One possibility for obtaining correct dark references is to acquire an energy filtered image (or thickness map) with a blanked beam, using the same integration time as will be used to acquire the core-loss image. Usual precautions have to be taken to avoid temporary damage to the array by previous exposure to an intense electron beam.

3.4. Conclusions

We have shown that TEM/EELS can measure (to 10% accuracy) the atomic concentrations of boron in carbon down to 0.2% (2000 ppm) at 1 μm spatial resolution. Since the sensitivity should depend on incident-beam current but not diameter, similar measurement should be possible with spatial resolution down to a few nm, provided that radiation damage and specimen drift is not a problem. We have also demonstrated boron mapping down to 0.5% B, using a Gatan energy filter with a pixel size of 66 nm.

3.5 References

Boothroyd CB, Sato K and Yamada (1990) Proc. XII Int. Cong. Electron Microscopy, San Francisco Press, San Francisco, vol. 2, pp. 80-81.

Coderre, J.A. and Morris, G.M., The radiation biology of boron neutron capture therapy. Radiation Research, 151, 1-18, 1999.

Egerton, R.F. (1991) Microscopy, Microanalysis, Microstructures 2, 203-213

Egerton RF, Yang YY, Cheng SC (1993) Ultramicroscopy 48, p 239-250.

Egerton RF (1996) *Electron Energy-Loss Spectroscopy in the Electron Microscope*, second edition, Plenum Publishing Co.

Egerton, RF (1999) Journal of Electron Microscopy 48 (1999), p.711.

Gavin, P.R., Kraft, S.L., Huiskamp, R., and Coderre, J.A. A review: CNS effects and normal tissue tolerance in dogs. Journal of Neuro-Oncology, 33, 71-80, 1997.

Krivanek, OL, Mory C, Tence M and Colliex C (1991) Microscopy, Microanalysis, Microstuctures 2, 260.

Leapman RD and Rizzo NW (1999) Ultramicroscopy 78, 251-268.
Leapman RD and Newbury DE (1993) Analytical Chemistry 13, 2409-2414.

Liu DR and Brown LM (1982) Developments in Electron Microscopy and Analysis (Institute of Physics Conf. Ser. No.61, I.O.P Bristol) 201-204.

Malac, M and Egerton, R.F. (1999), Microscopy and Microanalysis 5, 29-38.

Natusch, M KH, Humphreys CJ, Menon N and Krivanek OL, Micron 30 (1999) 173-183

Smith, D.R. et al. (1996) Cancer Research 56, 4302-4306.

Wang, Y.Y., HO, R., Shao, Z. and Somlyo, A.P. (1992) Ultramicroscopy 41, 11-31.

Chapter 4

Fabrication of submicrometer regular arrays of pillars and helices

(M. Malac, R.F. Egerton, M.J. Brett, B. Dick, published in Journal of Vacuum Science and Technology B 17(6), 1999, pp. 2671-2674)

4.1 Introduction

The propagation of electromagnetic waves in periodic structures exhibits an abundance of interesting properties[§]. In analogy to electron propagation in crystals, where bands of forbidden energies arise due to crystal periodicity, an energy gap can be formed for photon propagation in certain periodic structures. A microstructure with such (photonic) band gap is called a photonic crystal. If similar periodic structures are fabricated from magnetic materials, then they can be suitable for magnetic storage media.

Many processes have been exploited to fabricate such structures which are periodic in both 2 and 3 dimensions on a scale where a photonic gap can be formed in infrared or optical regions. Each of the fabrication processes employed so far suffers serious problems due to either a low level of process control or prohibitive cost and complexity. Here we present an easy and reliable method of fabrication of regular structures with a lattice constant adjustable to well below 1μm, offering a reasonable level of process control while keeping a sufficient number of degrees of freedom to allow for the growth of a wide range of structures.

[§] The original paper by Eli Yablonovich was published in Phys. Rev. Letters 58 (20) on May 18, 1987 on page 2059. Sajeev John and Jian Wang (Phys. Rev. Let. 64 (20), 1990, page 2418) calculated existence bound states of photons to an excited atom in a photonic bandgap material. Modification of blackbody radiation was studied by Cornelius and Dowling (Phys. Rev. A, 59 (6), 1999, page 4736). Bound states of photons in a cavity within photonic bandgap material was investigated by Maede et al (Phys. Rev. B 44 (24), 1991, page 13772).

4.2 Materials and Methods

To obtain a material with a photonic band gap in 2 dimensions, it is desirable to fabricate regular arrays of pillars[1,2]. To have the photonic gap in the infrared or visible regions the diameter of the helices and pillars as well as the lattice constant of the photonic crystal has to be in submicrometer region. A general local geometry that forms a photonic band gaps in three dimensions, was suggested by Chutinan and Noda as a regular array of helical structures[3].

A method for the growth of random arrays of well-defined helical structures, as proposed by Robbie[4,5,6], uses a tilted rotating substrate (Figure 4.1a) with a carefully controlled rotation rate, deposition rate and angle of the arriving species. This method (referred to as glancing-angle deposition or GLAD) also offers the possibility of growing well-defined pillars of given material, at a higher rotation rate[7,8]. To fabricate the structures proposed by Chutinan and Noda[3], the glancing angle deposition method[4,5,6] provides a suitable level of process control** for the growth of random arrays of well defined helices (or pillars). However, the position of the individual helices on the substrate is randomly determined by the nucleation process.

For the growth of ordered arrays, it is necessary to suppress randomness in the nucleation stage of film growth and to be able to predictably control nucleus size and position. Since the deposition (for growth of both helices and pillars) is done onto an oblique substrate, shadowing by nuclei already present on the substrate can determine where further film growth will occur. Growing the film onto a substrate where suitable nuclei were already patterned will therefore enable growth of pillars or helices in

** The pitch angle of the helices is controlled by the angle of incoming vapour θ, as described in reference 11.

regular arrays. Supposing that shadowing only by next nearest neighbors is sufficient to suppress random growth between the patterned nuclei, we have:

$$\tan\theta = \frac{a\sqrt{2}}{h} \qquad (4.1)$$

where θ is the angle of arriving species relative to the substrate normal, h is the height of the artificial nuclei (thickness of the film after lift-off, see Figure 4.1) and a is the lattice constant of the structure, as depicted on Figure 4.1b. Moreover, the diameter of each artificial nuclei should be comparable to the natural diameter of (randomly) growing structures, in order to reduce the chance of growth of more than one feature (helix or pillar) from a given artificial nucleus.

The next consideration is the fabrication of an array of suitable-sized nuclei for film growth. The diameter of randomly growing features is of the order of 200 nm and it is desirable to provide artificial nuclei of a similar diameter. The smallest feature size easily achievable by electron-beam lithography (based on PMMA photoresist) is of the order of 100 nm, close to the required value. We find that the maximum thickness h for convenient lift-off of material between the nuclei is in the 200–500nm range. Eq. (4.1) then allows us to estimate the maximum spacing a between the nuclei for sufficient shadowing for given incident angle θ: the lattice parameter a is in the μm range for incident angles θ from 80 to 85 degrees and nuclei height h= 200-500nm. Further growth of pillars or helices, starting from the artificial nuclei less 1μm apart and more than 250nm in height, should then take place mainly from those artificial

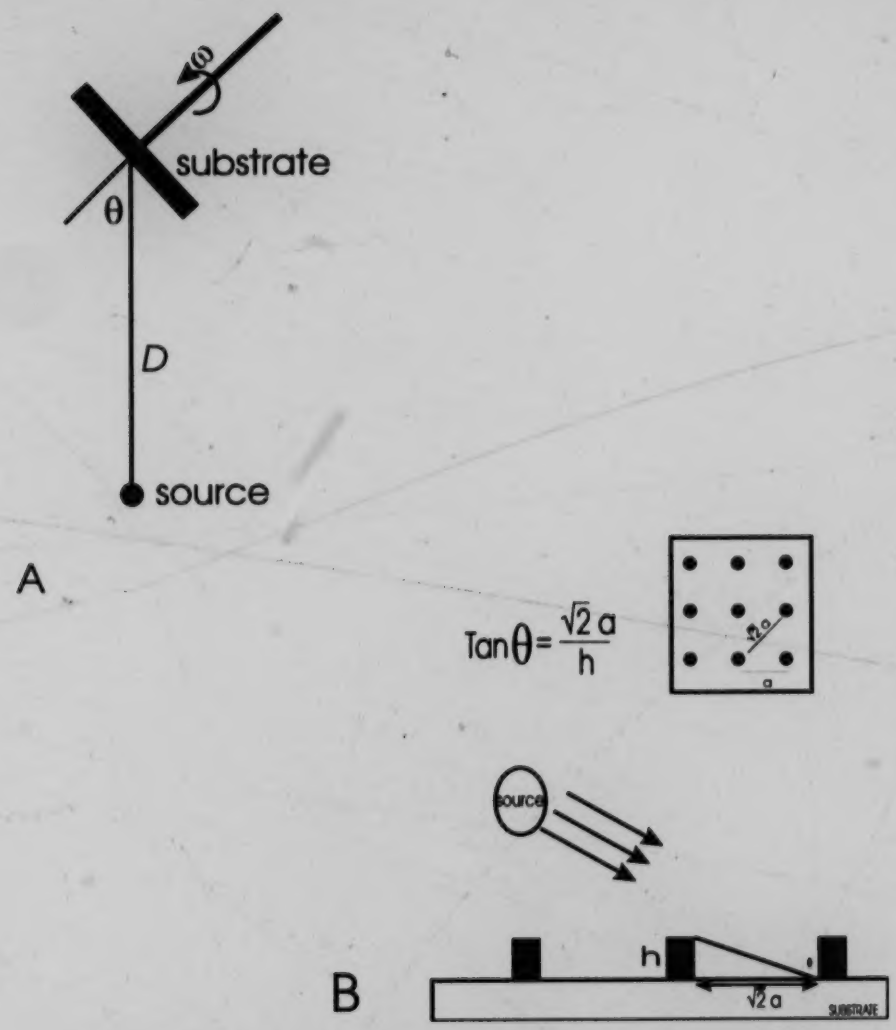

Figure 4.1. a) Position of the substrates in the vacuum chamber; b) Geometrical considerations for the patterning of a regular array of helices or straight pillars.

nuclei produced by lift-off[††]. Arrays of up to 1000x1000 features were grown using above method, making use of a Philips 505 scanning electron microscope (SEM) operated at 30kV and driven by a digital raster provided by an external computer running the SMART program[9].

Although dielectrics or semiconductor materials would be preferable for the growth of photonic crystals, we selected Ti, and Bi as trial materials. The large difference of their melting points implies that different mechanisms dominate during the growth process. Regular arrays of cobalt pillars were grown to assess the possibility of using the GLAD method to grow regular magnetic structures with diameter and lattice constant in submicrometer range. Titanium, cobalt and bismuth films were grown in a diffusion-pumped vacuum system equipped with a LN_2 cold trap. A typical base pressure was $4x10^{-5}$ Pa and the pressure during the film deposition did not exceed $7x10^{-5}$ Pa. The titanium and cobalt films were deposited using an electron-beam evaporation unit. A resistively heated source was used for thermal evaporation of bismuth. A detailed list of the deposition parameters can be found in the table 4.1. The source purity was 99.5% and 99.999% for titanium and bismuth respectively, the cobalt source purity was 99.95%. Silicon wafers were used as substrates. The deposition rate was monitored in situ using a Sycon STM-100 /MF thin-film thickness monitor.

[††] In most cases the nuclei were fabricated from the same material as the structures themselves, however no difficulties were encountered by growing nickel structures onto titanium nuclei.

	Figure	substrate tilt θ	rotation rate [rpm]	growth rate [nm/s]	growth per revolution [nm/revolution]
Ti helices	2	86°	0.12	0.155	77.5
Ti pillars	3	86°	1.6	0.9	33
Co pillars	4	86°	0.22	0.15	14

Table 4.1 Deposition parameters for film growth. Substrate tilt is the angle between the substrate normal and incoming flux (see Fig. 4.1); rotation rate is number of revolutions of the substrate per minute; growth rate is the flux of species reaching unit area of the substrate, allowing for the substrate tilt; growth rate per revolution is thickness of material deposited during one revolution of the substrate, as estimated from the crystal thickness monitor.

4.3 Results

Scanning electron microscope (SEM) observations were made on as-prepared samples. The samples were scratched across the patterned area to reveal a side view of the growing structures. A regular array of titanium helices grown with lattice parameter a = 380nm is shown in Fig. 4.2. The origin of the debris visible between the helices in Fig. 4.2 is probably incomplete shadowing during the initial stages of film growth. The thickness of the debris, as estimated from cross sectional view, is less than 5% of the helix height. Both the random and patterned areas of the titanium film show a strong tendency towards branching (bifurcation) within the growing structures. This bifurcation (branching) is present even at a stage close to the beginning of film growth and becomes more pronounced as the film grows. The growth regime of titanium films is probably dominated by strong shadowing (even within one pillar or helix arm) and low adatom diffusion, as expected from low ratio (0.15) of the substrate temperature T_s to melting point T_m for titanium.

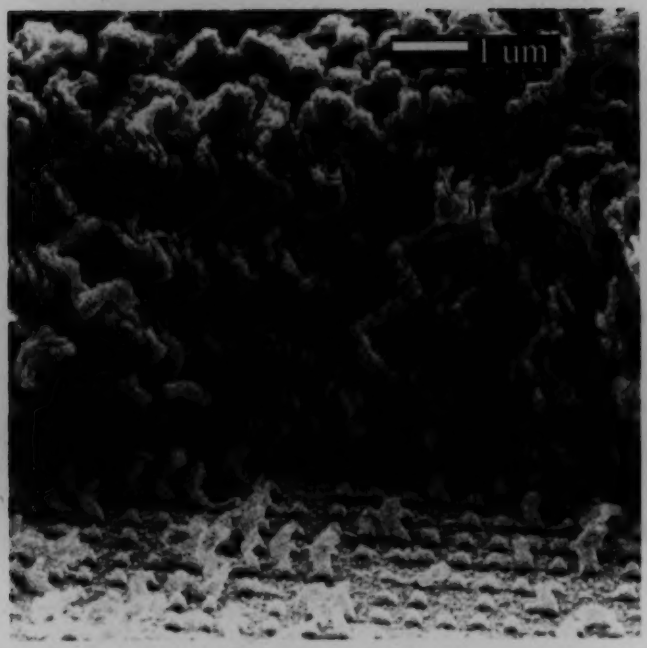

Figure 4.2. SEM micrograph of a regular array of titanium helices with lattice parameter a = 380 nm. The scale bar corresponds to 1 μm.

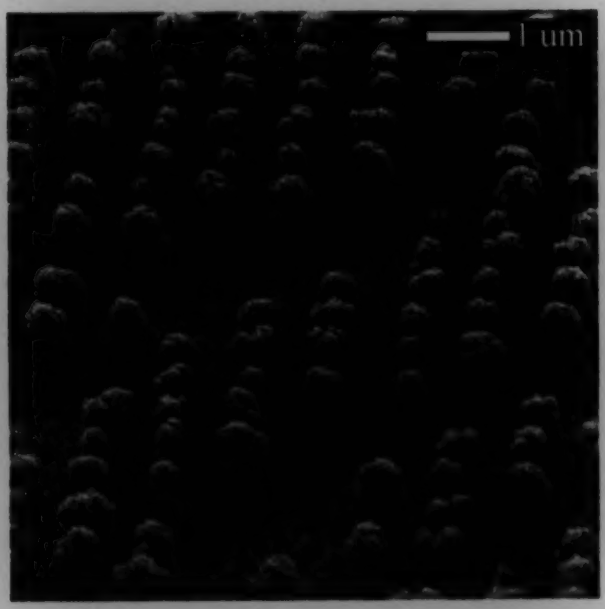

Figure 4.3. Regular array of titanium columns with lattice parameter a = 800 nm. Note the presence of the patterning defect in the centre of the micrograph. The scale bar corresponds to 1 μm.

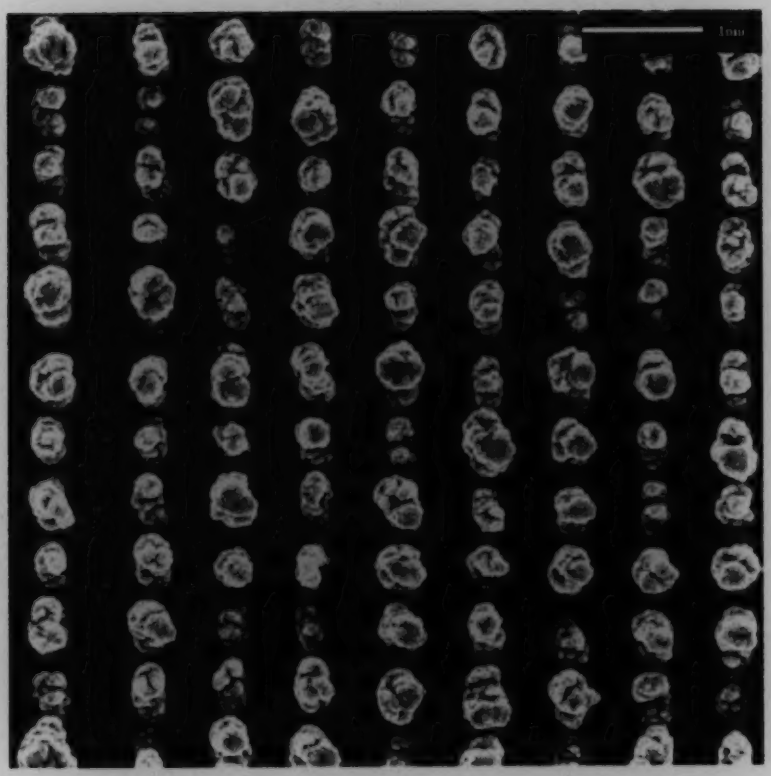

Figure 4.4.A regular array of cobalt pillars deposited onto prefabricated Ti nuclei at θ = 86° incident angle. The height of the pillars is between 250 nm and 300 nm. The scale bar corresponds to 1 μm.

An oblique view of a regular array of titanium pillars is shown in Fig. 4.3. The presence of a defect in the regular pattern (several artificial nuclei missing in the center of Fig. 4.3) does not seem to have a radical effect on film growth: neither the height nor the diameter of the nearest pillars is affected by the presence of this defect. However the amount and size of the debris between pillars seems to be increased within the defected area. The rather small influence of missing nuclei on the growing structure suggests the possibility of deliberately introducing rows of missing artificial nuclei (implying rows of missing pillars after the film growth) and thus creating waveguides for the propagation of electromagnetic waves through such media, as well as the possibility of photon localization[2].

Structures made from bismuth (both random and patterned) show much less inclination towards bifurcation. Each bismuth helix tends to have a very limited number of crystallites. The strong suppression of bifurcation in case of bismuth can be attributed to an enhanced surface diffusion of adatoms, as expected from the high ratio of substrate temperature to melting point (T_s/T_m=0.55).

Our substrate holder allowed rotation of the substrate only about one axis and was not designed to change substrate tilt during the deposition. Changing the angle of incidence during growth gives an additional degree of freedom, allowing control over the shape, pitch and air filling of the helices[4,5,6].

Magnetic storage media is another area of application for periodic arrays of pillars. Recent research has studied fabrication of both longitudinal (magnetic field axis pointing along the plane of the substrate) and perpendicular (magnetic field axis

perpendicular to the substrate) single-magnetic-domain bits[10]. To fabricate an array of perpendicular single-magnetic-domain bits it is desirable to fabricate posts (pillars) perpendicular to the substrate surface[11]. Ideally the size of each post is such that it contains only a single magnetic domain, and is isolated from other posts by placing them on a non-magnetic media (e.g. silicon).

Deposition of random arrays of magnetic pillars (Fe and Co) using the glancing angle deposition method has already been demonstrated and magnetic characterization of the resulting film was reported[8,11,12]. However, random distribution of pillars (posts) make it more difficult to track individual bits for reading and writing. Techniques such as nanoindenting[10] and optical-interference lithography[13] have been employed to fabricate regular arrays of magnetic posts, however the fabrication process is usually fairly complex. Growth of magnetic-material pillars using glancing angle deposition onto a patterned substrate offers the possibility to simplify the fabrication process. Figure 4.4 shows cobalt pillars of height ~300 nm produced by electron-beam evaporation of Co over the top of a regular array of titanium artificial nuclei. Fabricating a periodic array of magnetic pillars will eliminate the tracking inefficiency inherent in previous glancing angle deposited films and allow the pillars to be used as a potential magnetic-storage medium.

4.4 Conclusions

We have demonstrated a method for producing regular arrays of helices and pillars with dimensions suitable for use as photonic crystals and magnetic-recording media.

4.5 References

[1]D. Labilloy, H. Benisty, C. Weisbuch, T. F. Krauss, R. M. De La Rue, V. Bardinal, R. Houdre, U. Oesterle, D. Cassagne and C. Jouanin, Phys. Rev. Lett. **79**, 4147 (1997).

[2]A. Mekis, F. Shanhui, J. D. Joannopoulos, Physical Review B **58**, 4809 (1998).

[3]A. Chutinan, S. Noda, Physical Review B **57**, R2006 (1998).

[4]K. Robbie, M. J. Brett and A. Lakhtakia, J. Vac. Sci. Technol. A **13**, 2991 (1995).

[5]K. Robbie and M. J. Brett, J. Vac. Sci. Technol. A **15**, 1460 (1997).

[6]Robbie K, Sit JC, Brett MJ, *J. Vac. Sci. Technol B 16*, 1115, (1998).

[7]J.C. Sit, D. Vick, K. Robbie and M. J. Brett, Journal of Material Research **14**, 1197 (1999).

[8]F. Liu, T. Umlor, J. Weston, W. Eads, J. A. Barnard and G. J. Mankey, J. Appl Phys **85**, 5486 (1999)

[9]R. F. Egerton and L. Wan, Journal of Microscopy **191**, 113 (1998).

[10]S. Y. Chou, Proceedings of the IEEE **85**, 652 (1997).

[11]K. Robbie, *Glancing Angle Deposition*, Ph.D. Thesis (University of Alberta), 1998.

[12]B. Dick, M. Brett, M. Aktary and M. McDermott, MRS-99 Spring Conference (Symposium J), 1999.

[13]M. Thielen, S. Kirsch, H. Weinforth, A. Carl and E. F. Wasserman, IEEE Transactions on Magnetics **34**, 1009 (1998).

Chapter 5

Observations of the microscopic growth mechanism of pillars and helices formed by glancing-angle thin-film deposition

(Marek Malac, Ray F. Egerton, submitted to Journal of Vacuum Science and Technology A)

5.1 Introduction:

Deposition of thin films onto a *rotating* substrate oriented obliquely with respect to the flux of incoming vapour (as depicted in figure 5.1a) allows growth of a wide range of film structures[1-12]. This technique, often referred to as GLAD (GLancing Angle Deposition[2,7]), offers high degree of control over the film microstructure. Film morphologies in the form of separated pillars[23], zig-zags and helices[1,3-5,8,9] can be fabricated. Possible applications range from optical media and filters[13-17,60] to magnetic-storage media[7,8,10,18,60] and biological applications[7,59,60]. Although the parameters influencing the growth of such films have been studied by several groups[2,3,5,9,11,12,19,20] there is still a need for understanding of the processes underlying film growth on a microscopic scale. Here we present results of cross-sectional transmission electron microscopy (TEM) of GLAD films and discuss the microscopic processes which influence the final microstructure. We have previously described a technique for growing pillars and helices in the form of a regular array, with sub-micrometer repeat distance[8], in the present paper we compare the growth of regular arrays to growth of random-nucleated areas. We also briefly discuss the influence of

substrate rotation and introduction of regular array of nuclei on microstructure of obliquely deposited films.

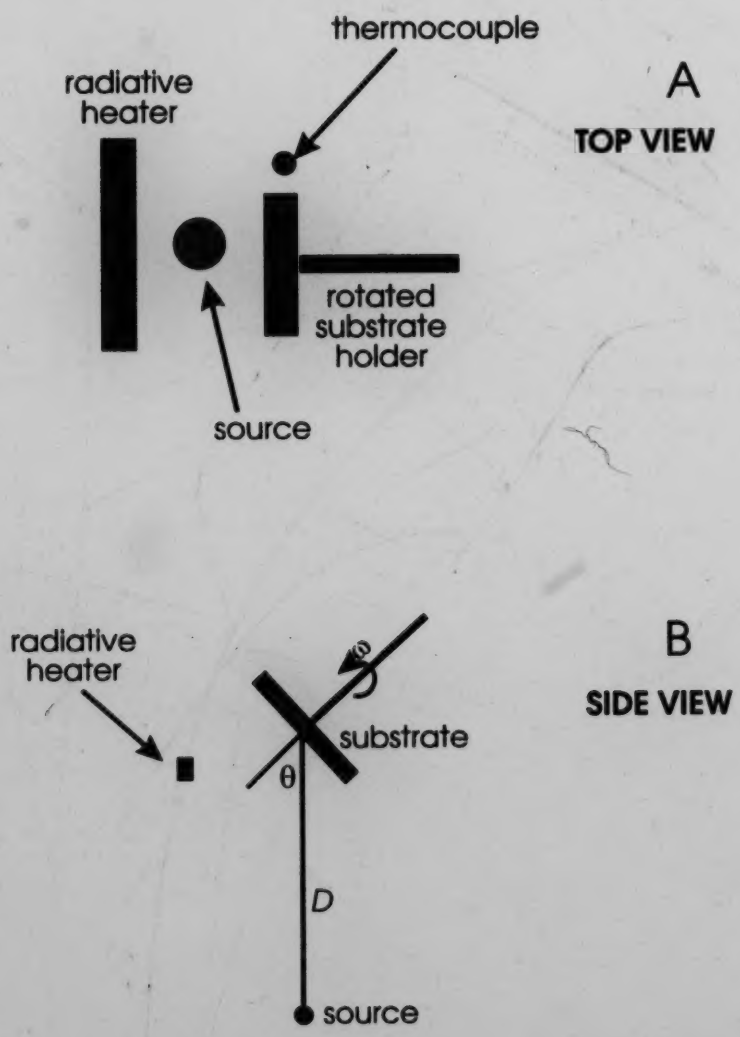

Figure 5.1 a) Substrate positions and movements in the deposition chamber. b) locations of the thermocouple and radiative heater.

In the following text, the term *column* refers to a structure grown onto *stationary* substrate oblique with respect to the incoming flux of atoms, whereas the terms *helix* and *pillar* refer to structures grown onto *rotating* substrate, oriented obliquely with respect to the incoming flux (figure 5.1a). *Slow* substrate rotation implies a high ratio of deposition rate and substrate rotation, as required for the growth of helices; *fast* rotation implies a low ratio of deposition rate and rotation rate, corresponding to the growth of pillars.

5.2 Experimental methods

Thin films of bismuth, silicon, silicon monoxide, silicon dioxide, nickel and titanium were deposited onto *rotating* substrates, inclined obliquely with respect to the incoming vapour flux as depicted in the figure 5.1b. These films were deposited using electron-beam evaporation in a diffusion-pumped vacuum system[8] with base pressure below 5×10^{-7} torr. The materials were pre-evaporated with a closed shutter for at least 5 minutes prior to deposition. Source purity was 99.5% or better for each of the materials used. The source to substrate distance (measured between centers) was D = 42 cm (see figure 5.1a) and the diameter of the vapor source was ϕ_{source} = 1 cm or less, giving a convergence angle α of the incident flux at the substrate of approximately 1 degree. The angle θ between the substrate normal and the incident flux was between θ = 80° and θ = 87° for all depositions and was kept constant during each deposition. We used 100 or 111 oriented, polished silicon wafers as substrates.

Cross-sectional samples for transmission electron microscopy were made by sandwiching small portions of film (scraped off the substrate) between two 200-mesh TEM grids coated with an amorphous-carbon film[7]. Samples were examined in a JEOL 2010 transmission electron microscope[21] (TEM) operated at 200 kV and equipped with a LaB_6 electron source, energy-dispersive x-ray (EDX) detector and a Gatan 666 parallel-recording electron energy-loss spectrometer (PEELS).

Patterning of arrays of nuclei on silicon substrates was achieved using PMMA-based lift-off lithography[8]. Exposure of the PMMA was done in a Philips 505 scanning electron microscope[8] (SEM) connected to a digital image-acquisition system[22]. A field-emission scanning electron microscope (JEOL JSM 6301 FXV) was used to obtain cross-sectional images of "as grown" structures by scratching through the film, or by fracturing the substrate to reveal a side view of the grown film. In this way we were able to verify that entire (unbroken) helices or pillars were present in the TEM specimens.

5.3 Results and discussion

5.3.1 Randomly nucleated films

When a film is deposited onto a rotating oblique substrate, the resulting morphology can vary from pillars[4,5] to helices[2,11], depending on the substrate rotation speed[7]. The position of individual pillars or helices is determined by the randomness of the nucleation process and by shadowing during film growth[7]. The SEM micrograph in

figure 5.2 is an example of a film of randomly positioned silicon helices. The morphology of a film is determined by many parameters (the deposition angle θ, ratio of the rotation rate of the substrate with respect to the deposition rate, nature of the material being deposited etc.) as discussed by several authors[2,5,7,11,12,20]. Here we concentrate on experimental observation of the processes which influence growth on a sub-micrometer scale.

As can be seen in figure 5.2, the helix-arm diameter gradually increases during deposition, resulting in wide distribution of helix-arm diameters[12]. Although this increase is undesirable for many applications, it conveys important information about the processes involved during the film growth. These processes may include:

(1) increase in the adatom diffusion length due to an increase in substrate temperature during film growth[12],

(2) increase of the amount of material deposited onto a growing helix due to a decrease in the number of neighboring helices (some helices terminate during deposition and the remaining ones collect material which would have been deposited onto those which were eliminated),

(3) increase in the number of atoms scattered between growing helices, due to a decreasing sticking coefficient (perhaps as a result of an increase in substrate temperature during the film growth),

(4) bifurcation (branching) within a growing helix due to self-shadowing within the helix arm, resulting in an increased number of fibers growing within each arm,

Figure 5.2 Cross-sectional SEM micrograph of a randomly-nucleated array of silicon helices grown at $\theta = 83°$, deposition rate R = 5.5 nm/s and rotation rate 0.6 rev/min. The scale bar corresponds to 500 nm.

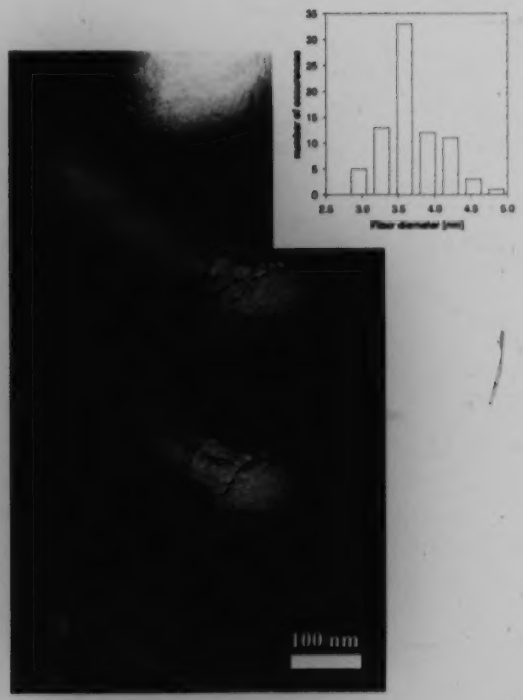

Figure 5.3 Cross-sectional TEM micrograph of a portion of a silicon helix from the same sample as figure 5.2. The scale bar corresponds to 100 nm. Inset: fiber diameter distribution obtained by measuring eighty fiber diameters at random positions within the helix.

(5) preferential growth of fast-growing crystal planes, which may promote bifurcation within a helix-arm,

(6) recrystallization and growth of crystallites within an already-formed helix.

5.3.1.1 Shadowing within and between helices

Figure 5.2 reveals that the increase in helix-arm diameter appears to be very fast during the initial 100 nm of film growth[‡‡]. This is also the growth stage in which competition between helices (due to shadowing between neighbors) is strongest, leading to large rate of helix eliminations, suggesting a strong influence of process (2), at least during the initial stages of the film growth.

This process can be understood from geometrical considerations. The larger the helix-arm diameter, the larger is the area which must be shadowed by its neighbors to eliminate an already growing helix. Small helix-arm diameter at the beginning of the film growth makes it easier to eliminate a helix, so the largest number of helix terminations occurs during the initial stages of growth. A model capturing similar behavior for perpendicular deposition onto a stationary substrate is discussed by Karunasiri et. al[24].This model is sometime referred to as a "grassy lawn" model[19], the individual stalks (representing growing columns) growing proportionally to the amount of light they receive. Even though very simple, such model already captures the scaling behavior of the growing film[31]. The situation for an oblique angle of incidence and stationary substrate has been discussed by many authors.[23,25-51] Krug

and Meakin recently discussed results of ballistic deposition for nearly-grazing incidence[52,53]. A continuum model capturing non-local effects such as shadowing was proposed by Keblinski et al[33].

Figure 5.3 is a cross-sectional TEM micrograph of part of a silicon helix extracted from the same sample as in figure 5.2; it reveals the helix to be composed of a large number of individual fibers growing close to each other. The diameters and spacing of the individual fibers appear to be fairly constant along the helix, as well as along each individual fiber. The fiber-diameter distribution is very narrow as can be seen from the inset in figure 5.3. Consequently it appears possible to relate the increase in helix-arm diameter to an increase in the number of fibers within a helix arm, suggesting the importance of process (4). The increase of the number of fibers within a helix arm is determined by the ratio of the frequency of bifurcation (branching and starting of a new fiber) to the frequency of fiber termination (elimination). The constant diameter of individual fibers within a helix arm throughout the whole helix suggests only a limited importance of process (1).

The behavior described above should apply to materials with very short adatom diffusion length, and was observed in titanium, nickel, silicon and silicon dioxide films grown between room temperature and about 300°C (corresponding to ratio of substrate temperature T_s and melting T_m point between $T_s/T_m = 0.15$ and 0.35). No major difference was observed between films deposited at constant substrate

---

‡‡ See appendix H for more details

temperature and on substrates where the temperature was either decreased or increased within the above mentioned range during film growth.

5.3.1.2 Importance of diffusion processes and crystallinity

It is generally believed that the influence of diffusion processes on the thin film growth increases with increasing ratio T_s/T_m of substrate temperature T_s and melting temperature T_m of a material[25,27]. Increased diffusion (both adatom and bulk) allows the crystalline nature of the growing material to exert a stronger influence on the final film morphology. To evaluate the importance of diffusion processes and the crystalline nature of a growing film, we grew nickel, silicon dioxide (SiO_2) and bismuth helices onto a room-temperature substrate. The corresponding T_s/T_m ratio is about 0.17 for nickel, 0.15 for SiO_2 and 0.55 for bismuth. Although nickel forms a crystalline film at room temperature, its low T_s/T_m suggests a regime where the adatom diffusion length is short[25]. Bismuth films also grow crystalline at room temperature and the high T_s/T_m indicates the importance of adatom (and perhaps even bulk) diffusion during film growth. The crystal structure of bismuth being rhombohedral, the growth rate depends strongly on the orientation of a crystal plane[54]. Silicon dioxide (SiO_2) gives amorphous or nanocrystalline films at room temperature and its low T_s/T_m suggests little influence from diffusion processes.

The surface-diffusion length manifests itself through the average crystallite size[12]. In nickel, the crystallite size within fibers is typically 5 - 10 nm, rarely reaching 20 nm. The fiber diameter is between 15 nm and 35 nm, so each fiber is

composed of many crystallites[§§]. This implies that surface smoothing due to adatom diffusion[19,25,27,32,33,46] influences the growth of nickel helices on scale smaller than the fiber diameter, in which case the mechanism responsible for bifurcation of the growing helices *is not* the difference in growth rate between different crystal planes (process 5). SiO_2 helices grown onto a room temperature substrate were amorphous, as confirmed by diffuse TEM electron-diffraction patterns. The diameter of individual fibers and frequency of branching is observed to be the same as for nickel. This similar behavior (of Ni and SiO_2) can be attributed to a similar influence of the diffusion process at similar T_s/T_m and little importance of crystallographic order (long-range in nickel and short-range in amorphous SiO_2)[47,56,56]. This again, in agreement with previous work[19,23,28,44,53] points to shadowing as the mechanism responsible for bifurcation at low T_s/T_m.

Unlike the case of deposition onto a *stationary (columns)* or *fast rotating (pillars)* oblique substrate, the incoming flux can reach deep between the growing structures when the substrate is *rotated slowly* (leading to the growth of *helices*). This behavior arises from the fact that a helix arm grows significantly in height during a single substrate rotation, leading to exposure of a portion of the side of an already grown helix to the incoming vapour flux. A new fiber within a helix-arm can be started by flux reaching the exposed side of growing fiber. This is a true three-dimensional problem, perhaps qualitatively different from the situation of films

[§§] See figure H.10 in Appendix H for more detail.

deposited onto a stationary oblique substrate[52,53]. A ballistic deposition model capable of simulating three dimensional problems is currently being developed by Smy et al[58].

For bismuth, a room-temperature substrate corresponds to a rather high ratio of substrate temperature to melting point ($T_s/T_m \sim 0.55$). In this situation the adatom diffusion length can be relatively large, permitting newly arrived atoms to search for a low-energy position (dictated by the crystalline nature of the material) over large distances. Moreover, such a high T_s/T_m may allow bulk diffusion within each helix, resulting in crystallites comparable in size to the helix-arm diameter and extending to a large fraction of the helix height. The frequency of branching in a bismuth helix is strongly suppressed compared to helices formed at low T_s/T_m (nickel, SiO_2, titanium, silicon). However, the large diameter of individual fibers results in a significant increase in helix-arm diameter even for small increase in number of fibers. As in the case of films grown at low T_s/T_m, the overall helix-arm diameter is determined by the number of fibers growing together.

Branching can be suppressed almost completely by carefully adjusting the ratio of deposition rate, rotation rate and substrate temperature. The film in figure 5.4 is composed of 3.7 μm-high single-crystal bismuth helices of relatively small diameter (240 nm) which is almost constant over the entire height of the helix. However, it remains difficult to distinguish the effects of surface diffusion (process (5)) and bulk diffusion (process (6)).

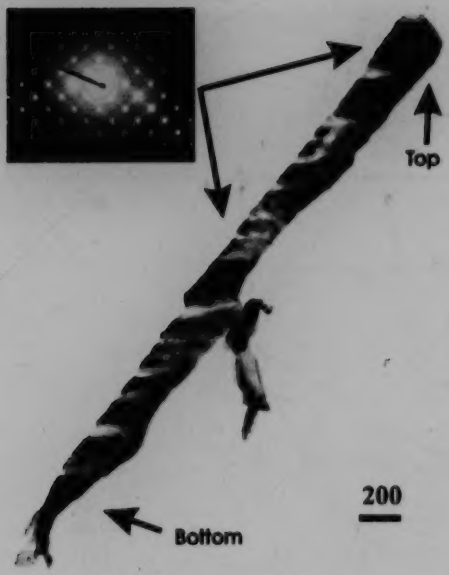

Figure 5.4 Cross-sectional TEM micrograph of a narrow bismuth helix deposited at $\theta = 86°$, 0.2 rev/min and R = 1 nm/s. Inset is diffraction pattern from the upper half of the helix. The scale bar corresponds to 200 nm.

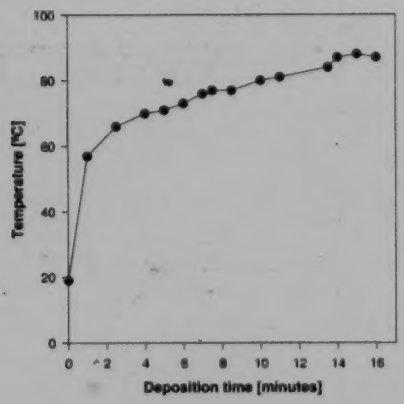

Figure 5.5 Typical profile of temperature rise with increasing film thickness. Measured for nickel deposition, with deposition rate R = 8 Å/s and final film thickness measured by an in-situ crystal thickness monitor 770 nm (measured in plane perpendicular to the incoming flux of atoms).

The above results imply that substrate temperature is an important parameter determining the final morphology of the films. To control the substrate temperature, we installed a radiative heater at the substrate level (figure 5.1b), allowing the substrate heating to be adjusted independently of the operation of the vapor source. For example, by preheating substrates prior to deposition, followed by decrease in heater power during deposition, we were able to keep the film temperature constant to within a few °C. A miniature K-type thermocouple mounted at the same level as the substrate (same distance from the vapor source and heater) enabled us to monitor the substrate temperature on time scales much shorter than for a thermocouple mounted within the substrate holder. Nevertheless, such measurements should be taken only as an indication of changes in film temperature, rather than a precise reading of the temperature of the growing film.

A typical temperature profile for a deposition with *no* substrate heating is in figure 5.5. As can be seen, the temperature increases rapidly at the start of the deposition and very moderately thereafter. For films deposited without the use of radiative heater, any temperature-related change in diffusion would therefore happen within the first 1 min or so of the deposition. For most of our films this corresponds to the first few tens of nanometers of the film thickness. Similar observations were made for each film material: the final temperature did not exceed 130°C for high-T_m films (nickel, silicon, titanium) and was much lower for low-T_m films (bismuth).

5.3.1.3 Comparison with films deposited onto a *stationary* oblique substrate

The deposition of films onto a stationary substrate, oblique with respect to the incoming flux of atoms, has been studied by many authors since the early days of physical vapor deposition (PVD), both from experimental[24-27,29,30,37,43,46,49,50] and theoretical[19,23,31-36,38-42,44,52,53] perspectives. Early researchers realized the importance of shadowing for the oblique deposited films as reported by Smith et al[37] and references therein. Transmission electron microscopy revealed bundling of the columns in the direction perpendicular to the plane of incidence[26,30,37,46]. Abelman and Lodder published a comprehensive review of the processes involved in the deposition onto oblique stationary substrate[25]. On the theoretical side, the problem is approached from two directions. Models based on a continuum approach have been recently developed[33] that can capture non-local phenomena (such as shadowing)[***]. Ballistic deposition models have traditionally had more difficulties to incorporate surface smoothening by diffusion processes[23,32]. It is therefore desirable to compare deposition using the GLAD technique with deposition onto an oblique stationary substrate.

Silicon deposition onto a stationary substrate at an angle of $\theta = 83°$ (deposition rate R = 1.7 nm/s) resulted in a film composed of separated 950nm-tall columns, about 100 nm in diameter at the top. Figure 5.6 is a cross-sectional TEM micrograph of the

upper part of such a silicon column. It shows the column to be composed of individual fibers about 3 to 5 nm in diameter, which grow together within the column in the same way as the fibers which form a helix arm. Figure 5.6 also reveals that the shape of the top of a column is determined by the heights reached by individual fibers within the column and is approximately parallel to the substrate in the plane of incidence (inset). The cross-sectional profile of the column is likely determined by the spatial distribution of individual fibers within it. Due to the separation between fibers, the influence of processes such as parallel momentum transfer and trapping of adatoms by impurities[25] is likely to be limited to individual fibers. The lifetime (branching to termination length) is likely to be determined by shadowing between fibers within a column and by shadowing between columns. The column inclination angle for the silicon film in figure 5.6 was $\beta = 70°$ (determined from a cross-sectional SEM micrograph), somewhat closer to the substrate normal than the value ($\beta = 76°$) predicted by the tangent rule[25,23,32,44-46,51,52]. Branching within a column is less pronounced for nickel films deposited onto a stationary oblique substrate, but is still present and appears to be the mechanism determining the column diameter. The diameter of the individual fibers in nickel columns varies from 10 nm up to about 50 nm.

*** This model proposed by Keblinski et al (ref 33) is a phase-field model with dynamics which conserves the order parameter.

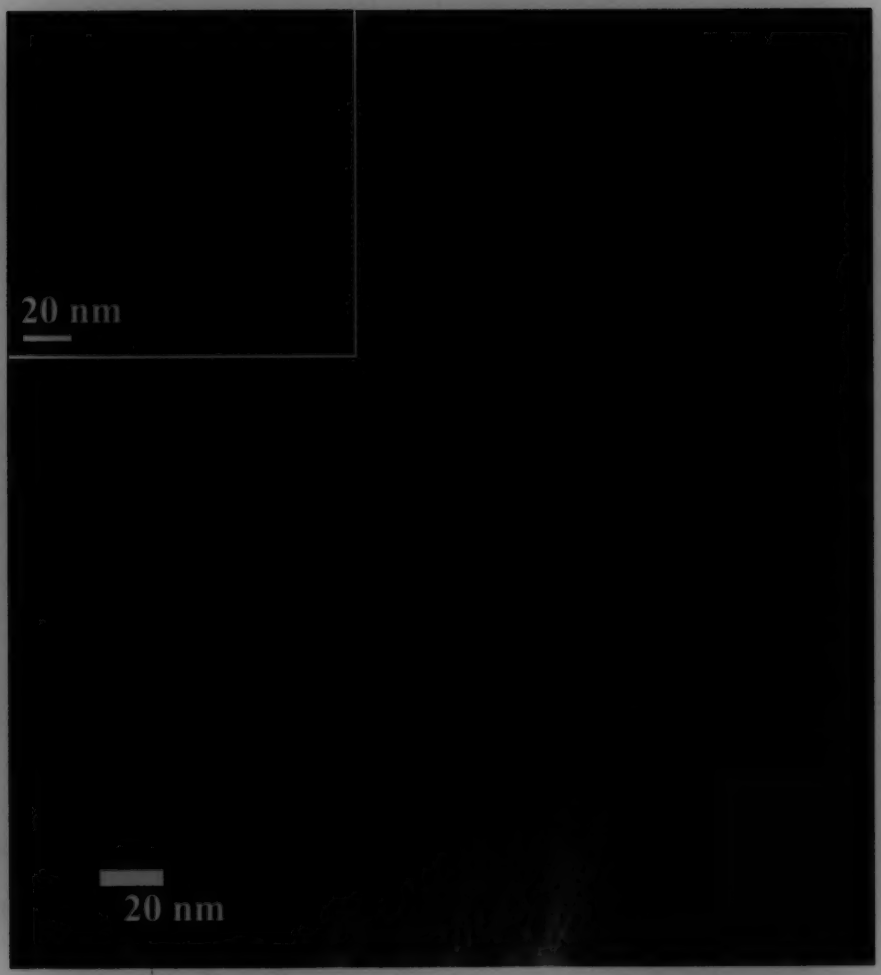

Figure 5.6 Cross-sectional TEM micrograph of silicon columns deposited onto a stationary substrate at θ = 83° and deposition rate R = 1.7 nm/s, viewed from a direction perpendicular to the plane of incidence. Inset: view of a similar column in the plane of incidence. The scale bars correspond to 20 nm.

The above observations illustrate the similarity between growth onto an oblique rotating substrate and onto a stationary substrate at low T_s/T_m (e.g. silicon onto a room-temperature substrate). Both columns and helices are composed of a number of individual fibers growing roughly parallel to each other. The overall shape of both columns and helices is determined by frequency of bifurcation of the component fibers, pointing to shadowing as the mechanism governing film growth. The frequency of bifurcation (and consequent increase in diameter) appears to be somewhat larger for helices (rotated substrate) than for columns (stationary substrate) under otherwise identical conditions.

5.3.1.4 Initial stages of growth of randomly nucleated arrays

Even though the initial stage (nucleation and first few nanometers) of film growth is short compared to the overall height of the helices, it may have a major influence on the resulting film[7]. In this section, we examine the processes which govern the first few nanometers of growth of a film deposited onto an oblique substrate which is *fast-rotating* (giving rise to *pillars*) or *stationary* (giving rise to *columns*).

The nickel film shown in figure 5.7 was grown onto a 10 nm-thick carbon-coated TEM grid at an angle of incidence $\theta = 83°$. The substrate was rotated 63 times during the deposition. The smallest particles in figure 5.7 are of the order of 2 nm in size; the largest ones are over 10 nm in diameter. The presence of small-size particles

(~ 2 nm) confirms the small size of critical nuclei[†††]. There is no faceting of the particles, suggesting a short adatom diffusion length. The nucleus-size distribution is fairly wide but the number of nuclei quickly decreases as their diameter increases. This suggests there is competition between nuclei (due to shadowing) at the early stages of film growth. The round shape, separation and size distribution of the nuclei confirms that deposition onto a fast-rotated oblique substrate can be viewed as deposition in which the incoming flux arrives from all azimuthal angles within a polar angle $\theta \pm \alpha$ (where α is the divergence angle of the vapor source)[4,5]. The fact that the film is composed of separate nuclei confirms that growth onto a fast-rotating substrate retains the importance of shadowing, which is characteristic for deposition onto an stationary susbtrate[23,25].

The nickel film in figure 5.8 was deposited onto an oblique *stationary* substrate to evaluate the influence of the substrate rotation during the initial stages of film growth. This film is composed of columnar fibers, aligned approximately in the direction of the incoming flux of atoms,[37,46] with diameters between 10 nm and 15 nm. The spacing of the individual fibers is typically less than 20 nm. Unlike figure 5.7, there are almost no particles between the growing columns. This suggests that there is more effective shadowing when the film is grown onto a stationary substrate.

[†††] Critical nuclei = smallest stable nickel particle. The critical nuclei is either same size or smaller than the smallest visible nickel particle in the figure 5.7. Caution has to be taken not to mistake the structure of the underlying amorphous carbon film with small nickel particles.

Figure 5.7 Initial stages of growth of nickel pillars: cross-sectional TEM micrograph of a film grown at $\theta = 83°$, deposition rate R = 0.1 nm/s. The substrate was rotated 63 times during film growth. The film thickness measured in situ using a crystal film thickness monitor placed in a plane perpendicular to the incoming flux of atoms is 40 nm. The scale bar corresponds to 20 nm.

Figure 5.8 Initial growth stage of a nickel film deposited onto a stationary thin-carbon substrate at $\theta = 83°$ and deposition rate R = 0.4 nm/s; the substrate temperature T_s did not exceed 70°C. The scale bar corresponds to 20 nm.

5.3.1.5 Pillars – deposition onto a *fast-rotating* substrate.

Decreased growth-to-rotation ratio (substrate rotated *fast*) results in pillar rather than helical film microstructure[4,5,7,23]. We will compare growth of pillar films (grown onto *fast* rotating substrate) with helical films (grown onto *slowly* rotating substrate) and columnar films (grown onto *stationary* substrate).

A cross-sectional TEM micrograph of a titanium pillar grown onto fast-rotated room-temperature substrate ($T_s/T_m = 0.15$) is shown in figure 5.9. The pillar diameter varies little during growth, remaining between 110 nm and 180 nm. Each pillar appears to be formed from a single fiber with occasional (unsuccessful) attempts at branching. The frequency of branching is strongly suppressed compared to helical films grown under similar conditions but slower substrate rotation. The crystallite size within a pillar in figure 5.9 is in the order of 20 nm. The small crystallite size suggests a short adatom diffusion length, a situation in which bifurcation was strong in the case of helices. The mechanism responsible for the reduced branching frequency for a fast-rotated substrate might be the prompt shadowing of newly starting fibers by the main pillar. Even though the underlying mechanism is different, the result of fast substrate rotation is similar to deposition onto an elevated-temperature substrate. However, the fast-rotation films do not allow for growth of helices and they still exhibit a certain degree of branching (usually seen as increased roughness of the pillar surface).

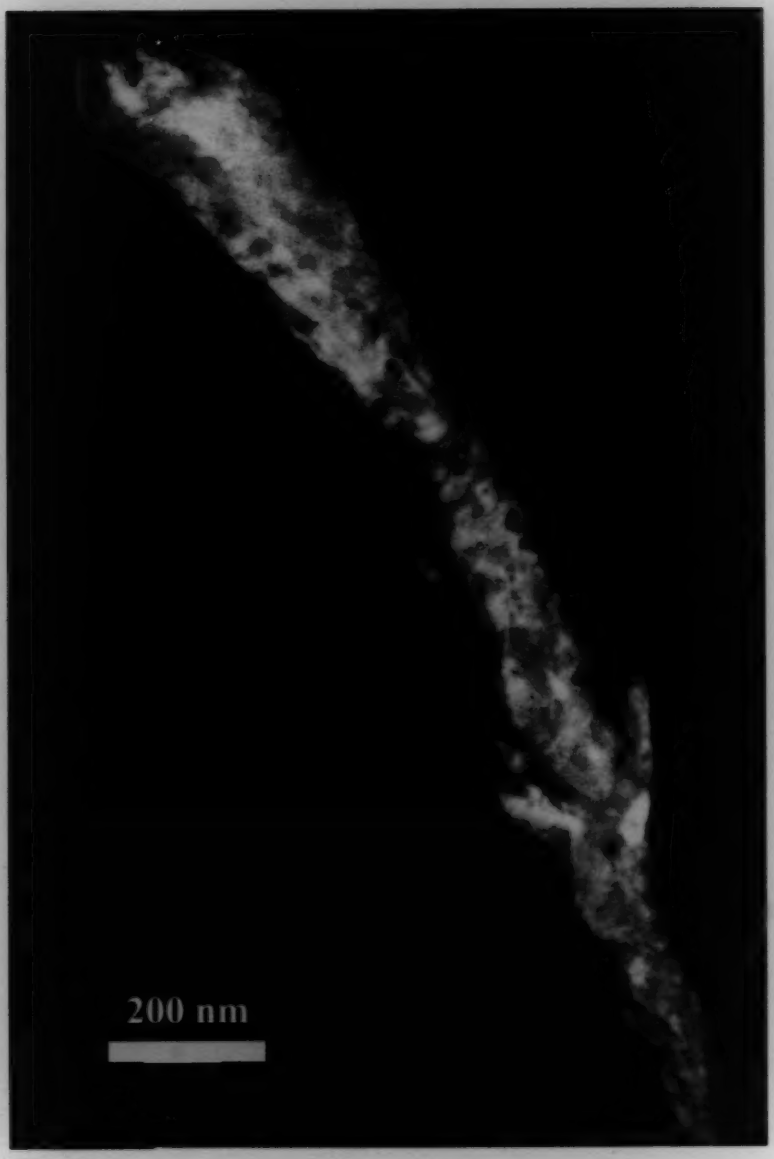

Figure 5.9 Cross-sectional TEM micrograph of titanium pillar grown onto fast-rotated substrate at $\theta = 85°$ and deposition rate R = 15 nm/s and rotation rate 12 rev/min. The scale bar corresponds to 200 nm.

5.3.2 Films grown onto a patterned substrate

We have shown previously that the GLAD method can be used to grow *regular* arrays of pillars and helices when deposition is done onto a pre-patterned substrate[8]. Here we will describe the similarities and differences between regular and random arrays and the influence of introducing a pattern defect on the growth of a regular array.

5.3.2.1 Differences in the growth of regular and random arrays

In the case of random arrays, the position (and size) of pillars and helices is determined by randomness of the nucleation process and by random selection due to shadowing between structures[7,19]. Since growth occurs on an oblique (rotating) substrate, any suitable-scale surface roughness (height modulation) is accentuated during film growth[19,24,25,32,33,35,36], especially under conditions of low adatom mobility[52,53]. To induce the growth of structures in regular arrays, we introduce suitable-scale surface roughness by patterning the substrate with arrays of artificial nuclei onto substrate prior to deposition[8]. If shadowing by next-nearest neighbors is sufficient to promote growth of the artificial nuclei, then for a square lattice we have[8]:

$$\tan\theta = 2^{1/2}\,(a/h) \qquad (5.1)$$

Here θ is the angle of arriving species with respect to substrate normal, h is the height of the artificial nuclei and a is the repeat distance (lattice constant) of the regular array, as depicted in figure 5.10a.

A top-view scanning-electron micrograph of the edge of a regular array of silicon helices (repeat distance about 1 μm) is shown in figure 5.10b, from which the relation between random (bottom part of the figure) and regular (upper part) helices can be observed. The distribution of helix-arm diameters in the regular array is much narrower than in the random area. The strongly anisotropic shadowing of the first row of helices within the regular array is responsible of the larger helix-arm diameter of this row. This larger diameter also reduces the growth of helices in nearby regions of the random area and within the second row of the regular array. This effect quickly diminishes towards the inner regions of the regular array, even though small helix-height variations were present in all our regular arrays (helices up to 10 μm high). Shadowing of a helix within a regular (square) array is provided by neighbors at a different distances (as the substrate is rotated through azimuthal angles), implying *anisotropic* shadowing, but the shadowing is the same (periodic) for all helices. Shadowing within a regular array is therefore *regular*, and this regularity has a determining influence on the helix-size distribution. Moreover, the regularity of shadowing within a regular array is maintained during film growth, resulting in only a moderate increase in helix-arm diameter (except for first few tens of nanometers, when a steady-state condition is being established).

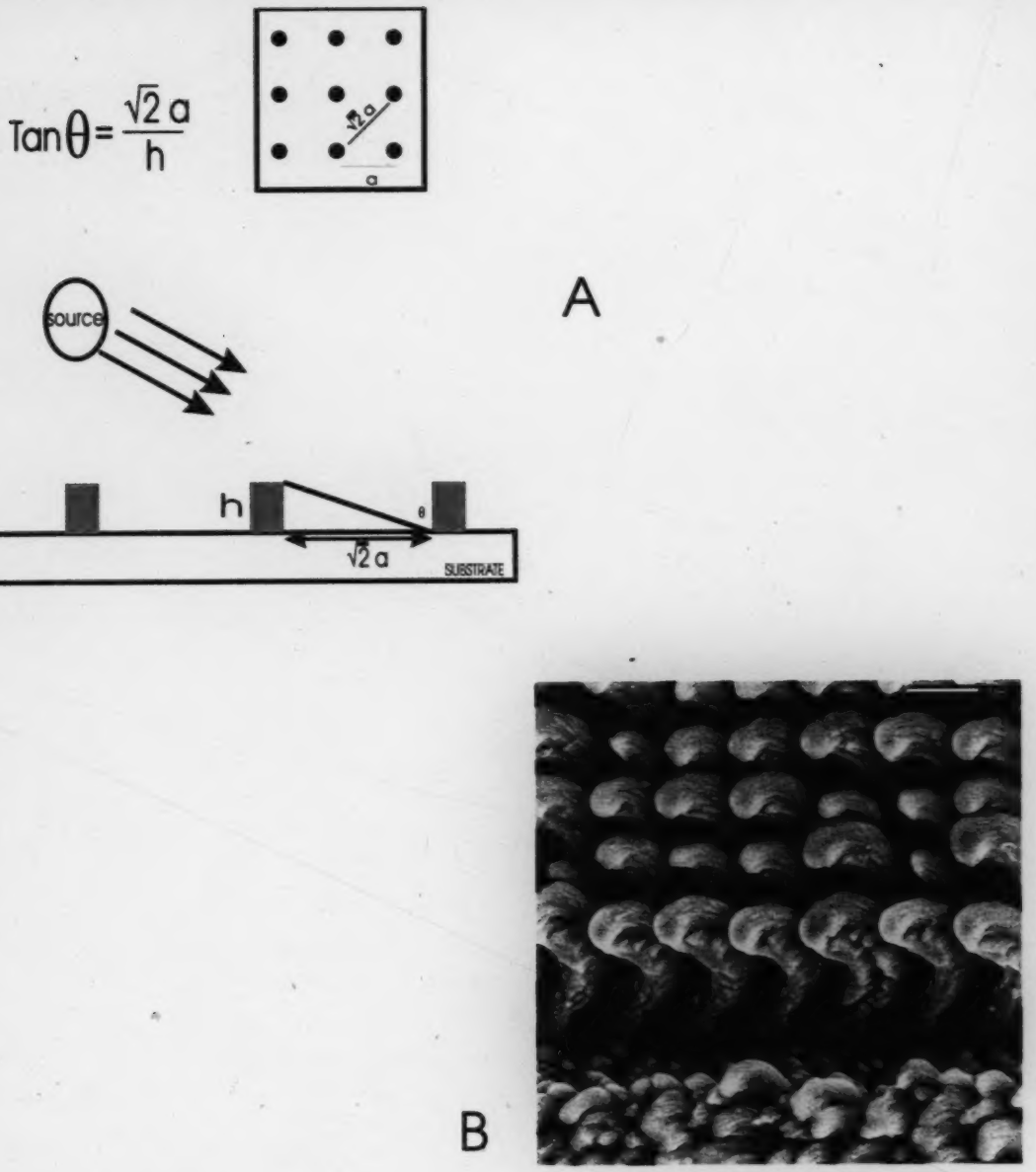

Figure 5.10 a) Geometrical considerations for patterning artificial nuclei for growth of a regular array of pillars or helices. b) Top view SEM micrograph of a border between regular (upper part) and random (bottom) areas of a silicon-helix array. The repeat distance of the array is about 1μm. The film was grown at θ = 83°, deposition rate R = 3 nm/s and rotation rate 0.1 rev/min. The scale bar corresponds to 1 μm.

5.3.2.2 Introduction of a defect into a regular array

The presence of a defect (such as a line of missing pillars or helices) in a regular array is desirable for some applications.[8,57] It is therefore desirable to determine the influence of introducing such a defect (at the patterning stage) on subsequent film growth. A top-view SEM micrograph of a line defect within a square array of silicon pillars (with repeat distance about 1μm) is shown in figure 5.11a. As can be seen, the presence of the line of missing pillars induces two major changes. First, the diameter of pillars directly neighboring the missing line is altered, likely due to reduced shadowing of flux arriving from the direction of the defect: incoming flux can reach deeper onto a pillar adjacent to the defect than elsewhere in the array. The more parallel (in the substrate plane) to the line defect the incoming flux arrives, the deeper it reaches.

The second change is the increased amount of debris between the pillars within the defect. The increased amount of debris within the defect was confirmed both by cross-sectional and top-view SEM (figure 5.11a). The origin of this debris is incomplete shadowing during film growth, since shadowing is less efficient in the area of the defect. However, the relatively minor influence of an initially-introduced defect (within the regular array) confirms the robustness of the growth process[‡‡‡]. Additionally, this robustness suggests that the height and spacing of the initial nuclei, leading to a desired surface morphology, may not be limited to those described by Eq. (5.1).

---

‡‡‡ The influence of a point defect on the growth of regular arrays is similar to the influence of a line defect but smaller in extent (see Appendix H, figure H.5).

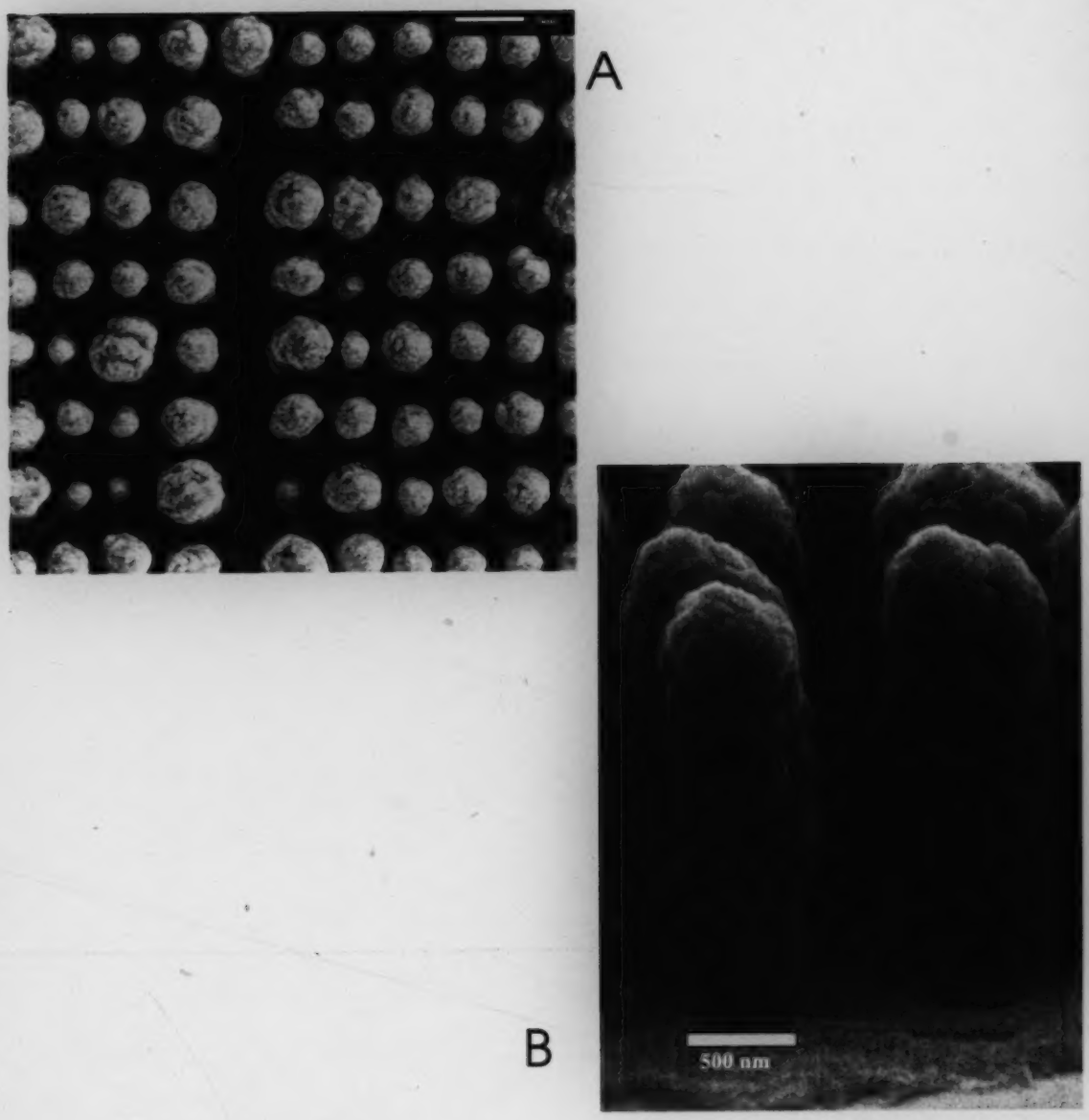

Figure 5.11 a) Line defect within a regular array of silicon pillars with 1 μm repeat distance. The film was grown at angle of incidence θ = 83°, deposition rate R = 5.5 nm/s and rotation rate 0.6 rev/min. The scale bar corresponds to 1 μm. b) Side view of a pillar within the same area; the scale bar corresponds to 500 nm).

The silicon pillar in figure 5.11b (taken from the same area of the sample as the figure 5.11a) reveals a relation between the growth of helices and pillars; a pillar is grown by filling in the helix-pitch. In the case of random arrays, this filling can be achieved by increasing the rotation rate. In case of regular arrays the transition from a helix to pillar can be achieved either by an increase of substrate-rotation rate or by adjusting (increasing) the nearest-neighbor repeat distance.

5.4 Conclusions

Our findings on growth of pillars and helices are summarized in this paragraph. The final shape of a helix is a result of competition between (adatom) diffusion and shadowing. For low ratio T_s/T_m (substrate and melting point temperatures) shadowing is the governing process. Shadowing seems to operate on at least two length-scales:

- among helices (leading to termination of whole helices)
- among fibers within a helix-arm diameter (leading to bifurcation and termination of fibers).

The helix-arm diameter is determined by the number of fibers within a helix-arm, even at considerably high T_s/T_m (~ 0.55). By adjusting the growth rate, rotation rate and substrate temperature, it is possible to suppress bifurcation and grow a single-crystal helix of considerable height with little increase of helix-arm diameter. The influence of bifurcation on final microstructure was suppressed by depositing onto *fast-rotated* substrate (allowing for growth of pillars). The diameter of pillars is given by shadowing between pillars rather than by adatom diffusion. Shadowing within a pillar

leads to reduced frequency of bifurcation compared to helices. The *columns* grown onto *stationary* oblique substrate were also composed of a large number of fibers. The column diameter is determined by number of fibers within a column. Fiber-diameter range in nickel columns was wider than in silicon columns. Both crystalline and amorphous materials exhibit similar behavior when grown under conditions with approximately the same (small) extent of diffusion processes (low T_s/T_m) with respect to shadowing.

The suppression of randomness during nucleation (introducing artificial initial surface height modulation) leads to growth of regular arrays. The periodicity of shadowing in regular arrays leads to suppression of helix termination and consequently to a steady-state or very slowly-evolving growth mode.

5.5 References:

[1]Robbie K, Brett MJ, Lakhtakia A, J. Vac. Sci. Technol. A **13** (6), 2991 (1995).
[2]Robbie K and Brett MJ, J. Vac. Sci. Technol. A **15** (3), 1460 (1997).

[3]Robbie K, Sit JC, Brett MJ, J. Vac. Sci. Technol B **16** (3), 1115, (1998).

[4]Sit JC, Vick D, Robbie K, Brett MJ, Journal of Material Research **14** (4), 1197 (1999).

[5]Liu F, Umlor T, Weston J, Eads W, Barnard JA, Mankey GJ, J. Appl Phys **85**, 5486 (1999).

[6]Robbie K, Broer DJ, Brett MJ, Nature **399**, 764 (1999).

[7]Robbie K, *Glancing Angle Deposition*, Ph.D. Thesis (University of Alberta), 1998.

[8]Malac M, Egerton R, Brett MJ, Dick B, J. Vac. Sci. Technol **B 17**, 1999

[9]Vick D. Tsui YY, Brett MJ, Fedosejevs R, Thin Solid Films **350**, 1999

[10]Dick B, Brett MJ, Smy TJ, Freeman M, Malac M, Egerton RF, Periodic Magnetic Microstructures using Glancing Angle Deposition *46 International Symposium of American Vacuum Society, Seattle October 25th–29, 1999.*

[11]Robbie K, Friedrich LJ, Dew SK, Smy T, Brett MJ, J. Vac. Sci. Technol. **A 13** (3), 1995.

[12]Vick D, Friedrich LJ, Dew SK, Brett MJ, Robbie K, Seto M, Smy T, Thin Solid Films **339**, (1999).

[13]Lakhatia A, Messier R, Materials Research Innovations **1** (3), 1997.

[14]Messier R, Lakhatia A, Materials Research Innovations **2** (4), 1999.

[15]Lakhatia A, McCall M, Optics-Communications 168, (1999).

[16]Lakhatia A, Optical Engineering **38** (9), (1999).

[17]Weighofer WS, Lakhatia A, Electromagnetics **19,** 4 (1999).

[18]Chou SY, Proceedings of the IEEE **85**, 652 (1997).

[19]Bales GS, Bruinsma R, Eklund EA, Karunasiri RPU, Rudnick J, Zangwill A, Science **249**, 264 (1990).

[20]Messier R, Gehrke T, Frankel C, Venogopal VC, Otano W, Lakhatia A, J. Vac. Sci. Technol. **A 15** (4), 1997.

[21]Egerton R, Cheng SC, Ultramicroscopy 55, 1994.

[22]Egerton R, Wan L, Journal of Microscopy **191**, 113 (1998).

[23]Dirks AG, Leamy HJ, Thin Solid Films **47**, 219 (1977).

[24]Karunasiri RPU, Bruinsma R, Rudnick J, Phys. Rev. Letters **62** (7), 788 (1989).

[25]Abelman L, Lodder C, Thin Solid Films 305, 1 (1997).

[26]van de Waterbeemd JGW, van Oosterhout GW, Philips Res. Repts **22**, 1967.

[27]Thornton JA, Ann. Rev. Mat. Sci. **7**, 1977 pp. 239-260

[28]Meakin P, J. Phys. A: Math. Gen. **20**, L1113 (1987).

[29]Pandaya DK, Rastogi AC, Chopra KL, Journal of Applied Physics **46** (7), 2966 (1975).

[30]Okamoto K, Hasimoto T, Hara K, Maiya M, Fujiwara H, Thin Solid Films **147**, 299 (1987).

[31]Kardar M, Parisi G, Zhang YC, Physical Review Letters **65** (9), 889 (1986).

[32]Muller-Pfeiffer S. van Kranenburg H, Lodder JC, Thin Solid Films **213**, 143 (1992).

[33]Keblinsky P, Maritan A, Toigo F, Messier R, Banavar JR, Physical Review E **53** (1), 759 (1996).

[34]Plischke M, Racz Z, Phys. Rev. Lett. **53** (5), 415 (1984).

[35]Plischke M, Racz Z, Phys. Rev. Lett. **54** (18), 2053 (1985).

[36]Lichter S, Chen J, Phys. Rev. Lett. **56** (13), 1396 (1986).

[37]Smith DO, Cohen MS, Weiss GP, J. Appl. Phys. **31** (10), 1755 (1960).

[38]Tang C, Bruisma R, Phys. Rev. Lett. **64** (7), 772 (1996).

[39]Kim JM, Kosterlitz JM, Phys. Rev. Lett. **62** (19), 2289 (1989).

[40]Family F, Vicsek T, J. Phys.A: Math. Gen. **18**, L75 (1985).

[41]Orlowski BA, Spicer WE, Baer AD, Thin Solid Films **34**, 31 (1976).

[42]Ko DYK, Seno F, Phys. Rev. E, 50 (3), R1741 (1994).

[43]Tait RN, Smy T, Brett MJ, J. Vac. Sci. Technol. A **10** (4), 1518, (1992).

[44]Meakin P, Phys. Review A **38** (2), 994 (1988).

[45]Nieuwenhuizen JM, Haanstra HB, Phillips Tech. Rev. **27** (87), 1996.

[46]Nakhodkin NG, Shaldervan AI, Thin Solid Films **10**, 109 (1972).

[47]Brietling G, J. Vac. Sci. Technol. **6**, 628 (1969).

[49]Kambersky V, Malek Z, Frait Z, Ondris M, Czech J. Phys. B **11**, 171 (1961).

[50]Lennard-Jonnes JE, Proceedings of the Physical Society **49E**, 140 (1937).

[51]Tait RN, Smy T, Brett MJ, Thin Solid Films **226**, 167 (1993).

[52]Krug J, Meakin P, Physical Review A **40** (4), 2064 (1989).

[53]Krug J, Meakin P, Physical Review A **43** (2), 900 (1991).

[54]Partin DL,Heremans J, Morelli DT, Thrush CM, Olk CH, Perry TA, Phys. Rev. B 38 (6), 3818 (1988).

[55]Rudee ML, Howie A, Phil. Mag, **25**, 1001 (1972).

[56]Shiojiri M, Myiyano T, Kaito C, Jpn. J. Appl, Phys, **18**, 1937 (1979).

[57]Mekis A, Shanhui F, Joannopoulos JD, Physical Review B **58**, 4809 (1998).

[58]Smy T, Vick D, Brett MJ, Dew SK, Wu AT, Sit JC, Harris KD, Three dimensional simulation of film microstructure produced by glancing angle deposition, Accepted for publication in J. Vac. Sci. Technol. A. (2000).

[59]Lakhatia A, Messier R, Brett MJ, Robbie K, Innovations in Materials Research 1 (2), 165 (1996).

[60]Robbie K, Brett MJ US patent # 5,886,204 (1999).

Chapter 6
Thin-film regular-array structures with 10-100nm repeat distance

Marek Malac, Ray Egerton, accepted for publication in Nanotechnology.

Deposition onto a rotating substrate which is oriented obliquely with respect to incoming flux (figure 6.1) allows the fabrication of thin-film microstructures such as helices or separated pillars (Robbie et al 1995, Dirks and Leamy 1977). The technique is often referred to as GLancing Angle Deposition (GLAD) (Robbie and Brett 1997). Due to the small angle between incoming atoms and the substrate, strong shadowing during such deposition enhances any initial surface roughness (Dirks and Leamy 1977, Bales et al 1990). We have shown previously (Malac et al 1999) that a patterning array of artificial nuclei on a substrate (prior to deposition) leads to the growth of pillars and helices in a regular array (figure 6.2). The locations of the pillars and helices within such arrays are determined by the positions of the pre-patterned nuclei (Malac et al 1999).

The ability to engineer film structure on a microscopic scale, by adjusting the substrate rotation and deposition rate, together with the ability to predictably position the structural units (pillars, helices) broadens the range of applicability of the GLAD technique (Malac et al 1999, Dick et al 2000). Control over the repeat distance on a sub-100 nm scale may allow new applications such as quantum devices (lasers), perpendicular magnetic-storage media (Dick et al 2000, Robbie and Brett 1999), molecular filters (Lakhatia 1996). In the present paper, we report on the size limits for

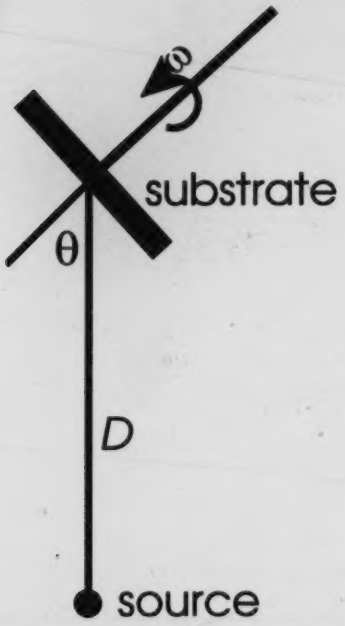

Figure 6.1 GLAD technique; position of the substrates in the vacuum chamber and substrate rotation during the film growth.

Figure 6.2 Scanning electron micrograph of regular array of large silicon helices with repeat distance a = 1250 nm. The film was deposited at angle of incidence $\theta = 83°$ deposition rate R = 30 Å/s and substrate rotation rate 0.1 min^{-1}. The scale bar corresponds to 500 nm.

the growth of regular arrays and we discuss the microscopic processes which determine those limits, in relation to models of thin film growth.

Our films were grown using electron-beam evaporation in a LN_2-trapped diffusion-pumped system having a base pressure below $5x10^{-7}$ torr (Malac et al 1999). The angle θ (typically 80° to 87°) between the incoming flux of atoms and the substrate normal (figure 6.1) was held constant during deposition. To enable patterning with sub-100 nm repeat distance, our substrates were 10nm-thick amorphous-carbon films stretched across 200-mesh electron-microscope grids. Deposited films, as well as the arrays of artificial nuclei, were examined using a JEOL 2010 transmission-electron microscope (TEM) equipped with a LaB_6 electron source, energy-dispersive x-ray (EDX) detector and a Gatan 666 parallel-recording electron energy-loss spectrometer (PEELS) (Egerton and Cheng 1994). The microscope was operated at 200 kV incident electron energy and artificial nuclei were patterned on the carbon foil using the same TEM. The use of a thin, light-element substrate greatly reduces proximity problems caused by backscattered electrons. In our case, 10 nm-thick amorphous carbon substrates allowed convenient TEM observation of grown structures; the use of silicon nitride windows would be a practical alternative. We used the phenomenon of localized contamination build-up (Hren 1979) in an electron beam to write the initial arrays. Since the amount of deposited contamination is proportional to incident charge (beam current times time) (Hren 1979) the nucleus height can be controlled by the beam dwell-time at each position where an artificial nucleus is created.

Figure 6.3 shows an array of silicon helices (each one sixth of a turn) grown onto a TEM-patterned substrate. The substrate was turned through an angle of $\Delta\varpi$ = 60° during the film growth. Figure 6.3 was recorded with the sample tilted 30° with respect to normal to the substrate plane. The repeat distance (determined from a perpendicular-view TEM micrograph) is 63 nm and the nucleus diameter about 20 nm. The helix-arm diameter is about 27 nm within the inner part of the array, and about 46 nm in the outer row of helices. This increase in helix-arm diameter is a consequence of the reduced shadowing of the outer row, compared the helices within the array. Figure 6.3 reveals that a helix arm is composed of many individual fibers, as we observe also in case of large helices (as in figure 6.2). The fiber diameter is 3.5 nm ± 1 nm and remains constant along the entire height of the helix (Malac and Egerton 2000). Fiber diameters in the regular array and in the surrounding random areas are the same, suggesting that this diameter is determined by processes (such as adatom diffusion) which are common to both areas, rather than by shadowing between helices. The large diameter of the artificial nuclei (relative to the fiber diameter) is most likely responsible for the large number of fibers which grow together within a helix arm. The random area in the figure 6.3 suggests that randomly nucleated helices start growing as a single fiber but branch later during the deposition. The narrow fiber-diameter distribution within a random array may be important for applications where a high areal density of small identical features is desired, such as field emission. The well-defined helix-arm diameter and spacing within the regular array is required for applications where well-defined repetitive features are desired, such as molecular filters (Lakhatia 1996) and magnetic storage media (Dick et al 2000).

Figure 6.3 Transmission electron micrograph of initial stage of growth of silicon helices grown onto a patterned 10 nm-thick amorphous carbon film. The helices are viewed at angle 30° with respect to substrate normal. The repeat distance of the array is about 63 nm. The film was grown at $\theta = 83°$, deposition rate (measured in a plane perpendicular to the incoming flux) R = 80 nm/min and rotation rate 0.1 rev/min. The substrate was rotated through $\Delta\varpi = 60°$. The scale bar corresponds to 50 nm.

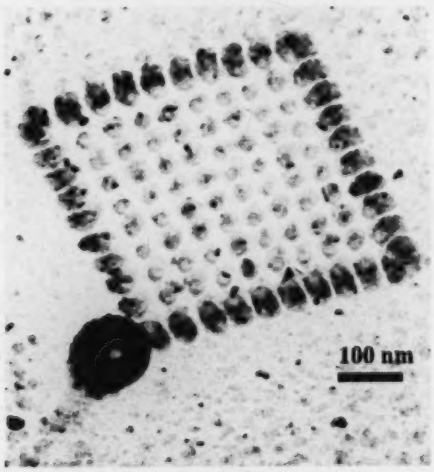

Figure 6.4 Cross-sectional TEM micrograph of a regular array of nickel pillars with repeat distance a = 35 nm. The array was grown onto a TEM-patterned 10 nm-thick amorphous-carbon coated grid at an angle θ = 83°, deposition rate R = 0.2 nm/s and rotation rate 0.3 rev/min. The scale bar corresponds to 100 nm.

Fast substrate rotation (low ratio of film growth to substrate rotation) during glancing-angle deposition results in films composed of isolated pillars (Dirks and Leamy 1977, Sit et al 1999). As in the case of helices, growth onto a pre-patterned substrate leads to the growth in a regular array. A cross-sectional TEM micrograph of regular sequence of nickel pillars is shown in figure 6.4, which shows a repeat distance of 35 nm and pillar diameter about 20 nm. This diameter is larger than the fiber width for nickel helices grown under similar deposition conditions (Malac and Egerton 2000) , suggesting that the pillar diameter is determined by shadowing between neighboring pillars (and within a pillar) rather than by the adatom diffusion length. Low-loss electron energy-loss spectroscopy (EELS) gave the height of the artificial nuclei as 40 nm, and the height of the nickel pillars as an additional 42 nm. Figure 6.4 reveals that each pillar is composed of a very limited number of crystallites, but contains a large number of stacking faults[§§§]. No nickel debris is observable between the pillars. Such a regular array of nickel pillars may find application as magnetic storage media (Malac et al 1999, Dick et al 2000). The regularity of the array would not only improve head-tracking[****] and signal to noise ratio (Lambert et al 1991), but also allow higher areal density then conventional magnetic-storage media (White et al 1997).

[§§§] The pillars in figure 6.4 provide large amount of diffraction contrast likely arising from stacking faults, crystallite boundaries, twins and other types of defects. Such defects are likely to provide preferential channels for bulk diffusion within grown pillars.

[****] Lambert et al (Lambert 1991) demonstrated that Patterned magnetic media can be used to provide feedback to head positioning device thus reducing problems with head positioning errors.

The behavior of pillars and helices described above is typical for materials with high melting point; any differences arising from whether they form crystalline (nickel) or amorphous (silicon) films are minor. We now consider the physical processes which set a lower limit on the growth of regular arrays, since this may determine the range of applications within the reach of the GLAD technique.

It appears possible to relate fiber diameter to smoothing of a growing structure by adatom diffusion (Bales et al 1990). Given suitably spaced nuclei, the minimum pillar diameter is likely determined by the adatom diffusion length at a given substrate temperature. The fiber diameter is typically less than 10 nm for high-melting-point materials deposited onto a room-temperature substrate, and could be adjusted by controlling the substrate temperature (Malac and Egerton 2000). Reduction of the substrate temperature should lead to shortened adatom diffusion lengths (Abelman dn Lodder 1997, Meakin 1988) and consequently reduced fiber diameter. Even at very low (~80 K) substrate temperatures, however, the arriving atoms tend to travel distances of a few unit cells along the film surface (Sanders et al 1986). Molecular-dynamic simulations suggest that the last portion of travel of an atom arriving at the substrate is in a direction perpendicular to local surface (Sanders et al 1986). The finite adatom diffusion length and change in the direction of arriving atoms are likely to set a limit on the smallest achievable repeat distance in regular arrays, by suppressing the importance of short length-scale initial surface roughness. The corresponding length scale (1 nm and smaller) is however out of reach of our current lithography technique,

which so far has created nuclei down to ~10 nm in diameter with repeat distance ~ 18 nm.

The growth of helices is somewhat different than pillar growth. A helix arm is typically composed of many individual fibers, which we believe to be a result of the required *low* ratio of substrate rotation to deposition rate. Slow substrate rotation leads to exposure of the *side* of a growing structure to the incoming atomic flux, thus promoting branching and an increase in the number of fibers within each helix-arm. However, the random area in the figure 6.3 suggests that helices can start to grow as a single fiber, if suitably small nuclei are provided. As mentioned above, the fiber diameter is related to the adatom diffusion length; adatom diffusion suppresses branching on the length scale over which it operates. To maintain single-fiber helix growth, the adatom diffusion length must be comparable to helix-arm diameter. This condition can be achieved by increasing the adatom diffusion length or by decreasing the repeat distance between the helices in a regular array. However, the repeat distance necessary for growth of single-fiber silicon and nickel helices onto a room temperature substrate would require nuclei 3 nm to 5 nm in diameter, which is below the reach of our current patterning technique.

From our experience, contamination lithography using high-molecular-weight linear carbonaceous molecules appears to be limited by "flow" of the written patterns under electron-beam irradiation and at elevated temperatures, as when the substrate is exposed to an evaporation source. This phenomenon becomes a problem at length

scales below about 20 nm repeat distance and about 10 nm nuclei diameter; it may derive from the fact that the beam-exposed polymer is not fully cross-linked, resulting in a low glass-transition temperature. So even though oblique deposition of high-melting-point materials onto a room-temperature patterned substrate provides opportunity for structural control on a scale below 10 nm, the limiting factor currently appears to be the resolution of the initial pattern-forming process.

6.1 References

Abelman L, Lodder C (1997), Thin Solid Films 305, pp.1.

Bales GS, Bruinsma R, Eklund EA, Karunasiri RPU, Rudnick J, Zangwill A (1990), Science 249, pp. 264-268.

Dick B, Brett MJ, Smy TJ, Freeman M, Malac M, Egerton RF (2000), Periodic Magnetic Microstructures using Glancing Angle Deposition, J. Vac. Sci. Technol A 18 (4), pp.1838.

Dirks AG, Leamy HJ (1977), Thin Solid Films **47**, pp.219.

Egerton R, Cheng SC (1994), Ultramicroscopy 55, pp.43.

Hren, JJ (1979), in Introduction to Analytical Electron Microscopy, ed. Hren JJ, Goldstein JI and Joy DC (Plenum, New York) pp.481

Lakhtakia A, Messier R, Brett MJ, Robbie K (1996), Innovations in Materials Research 1, pp. 165.

Lambert SE, Saunders IL, Patlach AM, Krounbi MT, Hetzler J (1991), J. Appl. Phys. 69, pp. 4724.

Malac M, Egerton R, Brett MJ, Dick B (1999), J. Vac. Sci. Technol **B 17**, pp. 2671.

Malac M, Egerton RF (2000), accepted for publication in Journal of Vacuum Science and Technology A (Chapter 5 of this thesis).

Meakin P (1988), Phys. Review A38 (2), pp. 994.

Robbie K, Brett MJ, Lakhatia A (1995), J. Vac. Sci. Technol **A 13** (6), pp.2991.

Robbie K and Brett MJ (1997), J. Vac. Sci. Technol. A **15**, pp.1460.

Robbie K, Brett MJ (1999), US patent # 5,866,204

Sit JC, Vick D, Robbie K, Brett MJ (1999), Journal of Material Research **14** (4), pp. 1197.

Sanders DE, Halstaed DM, DePristo AE (1992), J. Vac. SCI. Technol. A 10 (4), pp. 1986.

White RL, New RMH, Fabian R, Pease W (1997), IEEE Trans. Mag. 33 (1), pp. 990.

Chapter 7

General Discussion and Conclusions

This thesis contains summaries of the important results at the end of each previous chapter. This final chapter is aimed at outlining connections between the present work and current research, placed in a broader perspective. Possible directions of future research are also mentioned.

Transmission-electron microscopy is a mature technique capable of providing valuable information in variety of fields (as different as material science and cancer research) with high spatial resolution. Despite this maturity, electron microscopy and microanalysis has limitations and it is worthwhile to explore and attempt to extend these limits. The boundaries of electron microscopy can be envisioned in several directions: limits on the spatial resolution in imaging mode; limits on the information obtainable from electron diffraction; limits on the capabilities of elemental analysis, particularly the identification and quantification of small quantities of an element. The first two issues, imaging and diffraction, are closely related and are explored by many microscopists. Research seems to be progressing toward *quantitative* interpretation of high-resolution images and toward measurement of charge density distributions (Zhu, 1999). Those two topics are not discussed within the thesis. Instead, I have concentrated on quantitative analysis of light elements and the detection limits for light elements.

Chapter 2 was dedicated to the development of calibration samples necessary for quantitative analysis of light elements using Energy Dispersive X-ray (EDX) spectroscopy. The results of this work provide the microscopy community with a set of calibration samples necessary for quantitative analysis of light elements using EDX. Chapter 3 was concerned with probing limits of light-element detection using electron energy-loss spectroscopy (EELS), broadening our knowledge of the detection limits using EELS as well as identifying the processes underlying those limits in relation to practical issues.

It may be said that, although more widely used (because of its user friendliness), EDX does not offer the same wealth of information as EELS. Combined with energy-filtering transmission electron microscopy (for elemental mapping), EELS provides a potentially more powerful and reliable method of elemental analysis in a transmission electron microscope. The better sensitivity to light elements (Egerton 1996, pp. 25) and superior energy resolution (~1 eV compared to ~150 eV for EDX) makes EELS the method of choice for analysis of biological samples, which are composed mostly of light elements. Current achievements (Jouffrey and Egerton, 2000; Leapman, 1999) demonstrate the capabilities of EELS. The work described in Chapter 3 was aimed at analysis of radiation sensitive (biological) samples, where the detection of low concentration at moderate spatial resolution is often required. This situation is different from work aimed at probing minimum detectable mass (e.g. chemical identification of single atoms). The particular interest in boron detection and mapping is motivated by ongoing research on brain cancer treatment at Brookhaven National Laboratory.

The detection limit in the case of a parallel-EELS detector (such as the Gatan 666) stems from the gain variations within the detector array. Even though there are several methods available to circumvent this problem (Egerton,1996 pp. 108; Feng, 1999) each of them has limitations and it seems worthwhile to seek better methods for gain variation correction. The detection limit in case of a two-dimensional CCD detector is determined by the beam shot noise. In case of the Gatan Image Filter (GIF), the situation is worsened by the long CCD-readout time inherent to this system. Shortening the readout-time, blanking the electron beam during array readout or providing higher resolution of digitization of the CCD could improve the detection limit but would require hardware development.

Thin film technology was employed in the preparation of the calibration specimens (Chapter 2) and the boron-containing specimens (Chapter 3). Transmission (and scanning) electron microscopy can in turn provide a large amount of data on the morphology, structure and chemical composition of thin films. Chapters 4, 5 and 6 of the thesis are dedicated to studies of the microscopic mechanisms of thin film growth onto an oblique (rotating) substrate, often referred to as GLancing Angle Deposition (GLAD). The GLAD technique was recently developed in Dr. Mike Brett's group in Electrical Engineering Department (Robbie 1995, Robbie 1997 and Robbie 1998). It allows structural control of films on a scale of a few tens of nanometers by exploiting a shadowing mechanism during deposition onto an oblique substrate (Robbie 1998). This technique can be viewed as a significant extension of deposition onto an oblique

stationary substrate by adding another degree of freedom: substrate rotation. In fact, thin film growth onto a *stationary* oblique substrate, even though studied by many scientists, is not fully understood. A review by Abelman and Lodder (1997) provides good insight into the current situation. A wide range of applications of the GLAD technique has already been demonstrated by members of Dr. Brett's group (Robbie, 1995, Robbie 1997, Robbie 1998, Seto, 1999, Dick 1999) but a detailed understanding of the GLAD growth process is no more advanced than the understanding of growth onto a stationary oblique substrate. The large number of parameters influencing the growth and the complexity of their mutual relations can be blamed for these difficulties.

The motivation for my work on microscopic mechanisms influencing the growth is twofold. On the one hand, adequate understanding and better control over film growth and its microstructure is crucial to broaden the area of applications. On the other hand, the processes involved in film growth may provide fundamental insight into a whole class of stochastic processes. The models designed to explain such non-equilibrium growth approach from two main directions. The first class of models, often called continuum models, attempt to explain the growth using an almost macroscopic thermodynamic approach (Kardar, 1986). One of the most advanced models of this class is discussed by Keblinski et. al (1996), including a comparison with real films. The second class, sometimes referred to as "toy" models, includes diffusion-limited aggregation (DLA), ballistic deposition (Krug and Meakin, 1989, Smy et al. 2000) and models based on random walks (Eden, 1960). This class of

models treats film growth in terms of the discrete arrival of atoms at the substrate. Models of this class are more successful in describing growth in which non-local shadowing processes are strong with respect to adatom diffusion. Molecular dynamics simulation (MDS) can be considered a sophisticated model of the "toy" class. MDS models provide more detailed insight into the condensation phase of film growth (Sanders, 1992). However, such models require extensive computation even for small numbers of particles involved in the process, so can not be applied to large film thickness. The scaling behavior of the first two classes of these models is intriguing to theorists (Bales et al, 1990) due to the wide variety of phenomena which exhibit similar scaling properties.

On the experimental side, extensive work was done on obliquely deposited films onto stationary substrates. Interesting properties (magnetic and optical anisotropy) were the motivation for most of this research. The crucial importance of shadowing was recognized very soon (Smith, 1960 and references therein). Transmission electron microscopy of such films (Nakhodin 1972, Okamoto 1986) revealed the columnar nature of the growing films and bundling of the columns. But despite the large amount of research dedicated to understanding film growth, the interplay of the microscopic processes is still not fully resolved.

The work reported in chapters 4, 5 and 6 is an attempt to improve understanding of the growth process and the influence of substrate rotation on this process. Success in controlling the position of individual pillars and helices opens the

door to applications which require a high level of control over film microstructure. Controlling the positions of individual pillars and helices also results in more predictable and controllable shapes of the individual structures (pillars or helices). Probing the size limits for growth of regular arrays helps in recognition of the range of applications within reach of the GLAD technique. Identifying the processes setting those limits is necessary for pushing them even further. Cross-sectional TEM of grown structures (on both stationary and rotating substrate) revealed that the structures are composed of individual, separated fibers. This puts a boundary on importance of processes such as adatom diffusion and parallel momentum transfer. The fact that the individual helices start as single-fiber structures is also intriguing. The narrow (of the order of a few nanometers) fiber-diameter distribution can perhaps be exploited for applications such as field emission.

7.1 References

Abelman L, Lodder C (1997), Oblique evaporation and surface diffusion, Thin Solid Films 305, pp. 1-21.

Bales GS, Bruinsma R, Eklund EA, Karunasiri RPU, Rudnick J, Zangwill A, (1990) Growth and Erosion of Thin Solid Films, Science 249, pp. 264-268.

Dick B, Brett MJ, Smy TJ, Freeman M, Malac M, Egerton RF (1999), Periodic Magnetic Microstructures using Glancing Angle Deposition *46 International Symposium of American Vacuum Society, Seattle October 25 –29, 1999. Submitted to J. Vac. Sci. Technol. B.*

Eden M, (1960), Proceedings of the Fourth Berkley Symposium on Mathematical Statistics and Probability, University of California Press, Berkley 1961, pp. 223-239, edited by F. Neyman.

Egerton RF (1996) Electron Energy-Loss Spectroscopy in the Electron Microscope, Plenum, 1996.

Jouffrey B and Egerton R (2000), editors. *Electron Energy-Loss Spectroscopy*, Micron 31 (4).

Feng JL, Ho R, Shao Z, Solmyo AP (1999), Parallel electron energy-loss spectroscopy free from gain variation, Ultramicroscopy 76, pp. 221-231.

Kardar M, Parisi M, Zhang YC (1986), Dynamic Scaling of Growing Interfaces, Phys. Rev. Lett. 56 (9), pp. 889.

Keblinski P, Maritan A, Toigo F, Messier R, Banavar JR, (1996) Continuum model for the growth o interfaces, Phys. Rev E, 53 (1), pp. 759-778.

Krug J, Meakin P, (1989), Microstructure and surface scaling in ballistic deposition at oblique incidence, Phys. Rev. A 40 (4), pp. 2064-2077.

Leapman RD (1999), editor, *Towards Atomic Resolution Analysis*, Ultramicroscopy 78 (1-4).

Nakhodin NG, Shaldervan AI (1972), Effect of Vapour incidence angles on profile and properties of condensed films, Thin Solid Films 10, pp. 109.

Okamoto K, Hashimoto T, Hara K, Kamiya M, Fujiwara H (1987), Columnar structure and texture of iron films prepared at various evaporation rates, Thin Solid Films 147, pp. 299.

Robbie K, Brett MJ, Lakhatia A (1995), First thin film realization of a helicoidal bianisotropic medium, Journal of Vacum Science and Technology A 13 (6), pp. 2991-2993.

Robbie K, Brett MJ (1997), Sculptured thin films and glancing angle deposition: Growth mechanics and applications, Journal of Vacuum Science and Technology A 15 (3), pp. 1460-1465.

Robbie K (1998), Glancing Angle Deposition, PhD Thesis (University of Alberta).

Sanders DE, Halstead DM, DePristo AE (1992), Metal/metal homoepitaxy on fcc(111) and fcc(001) surfaces: Deposition and scattering form small islands, J. Vac. Sci. Technol. A 10 (4), pp. 1986.

Seto MW, Robbie K, Vick D, Brett MJ (1999), Mechanical response of thin films with helical microstructures. Journal of Vacuum Science and Technology B 17 (5), pp. 2172-2177.

Smith DO, Cohen MS, Weiss GP (1960), Oblique-Incidence Anisotropy in Evaporated Permalloy Films, J. Appl. Phys. 31 (10), pp. 1755.

T. Smy, D. Vick, M.J. Brett, S.K. Dew, A.T. Wu, J.C. Sit, and K.D. Harris (2000), Three dimensional simulation of film microstructure produced by glancing angle deposition, Accepted for publication in J. Vac. Sci. Technol. A.

Zhu Y (1999), editor. *Advanced Electron Microscopy Studies of High-Temperature Superconductors*, Micron 30 (5), pp. 355-560.

Chapter 8 Appendices

Appendix A

Calibration Sample Preparation Procedures

The following text gives detailed description of fabrication process for calibration samples discussed in Chapter 2.

A.1 Sample A (Carbon, Oxygen, Silicon)

This sample is optimized for measuring Cliff-Lorimer factors of oxygen ($k_{O/Si}$) and carbon ($k_{C/Si}$) related to silicon. The starting materials are
2.5 grams of SiO_2 (99.999%) powder (ICN Pharmaceuticals, Inc) and
2 grams of pure graphite powder (Aldrich #28286-3). These powders are mixed in a alumina mortar until a fine mixture is obtained. This mixture is then pressed to form a pellet ½ inch in diameter in a hydraulic press at pressure 6000 psi. These pellets in a copper crucible are electron beam evaporated in a diffusion pumped LN_2 trapped system. Preheating the pellets in an oven at 150 °C before introducing into vacuum helps to prevent spitting during evaporation. Freshly cleaved muscovite mica is a suitable substrate. The deposition parameters are:

- e-gun to substrate distance 19.5 cm
- e-gun to crystal thickness monitor distance 29.5 cm
- thickness monitor (Sycon STM 100/ MF) settings:
    - density = 2.20 g/cm^3

- Z factor = 1.070
- tooling factor = 225 %.

The 7cc Temescal® electron gun is operated at 7 kV with a filament current between 0.21 A and 0.23 A. Preheating the pellet prior to deposition (with closed shutter) at a filament current of about 0.18 A to 0.20 A for approximately 5 minutes helps to reduce spitting from the source during deposition. Base pressure $3x10^{-6}$ torr in the chamber is sufficient. The deposition under the conditions described above takes between 8 min and 9 min and should result in a film thickness of 140 Å on thickness monitor. Finally, the film is floated from the substrate by slow immersion in a deionized water and collected on a 200 mesh copper grid.

A.2 Sample B (Nitrogen, Oxygen, Silicon)

This sample is optimized for the measurment of Cliff-Lorimer k-factors for nitrogen relative to silicon ($k_{N/Si}$) and to a lesser extent for measuring the k-factors for oxygen with respect to silicon ($k_{O/Si}$). The sample contains a small amount of boron (which is not detected by the EDX) to avoid sample charging in the TEM.

The fabrication of the sample consists of two steps. First, a silicon – nitrogen film is prepared by reactive sputtering. Second, a thin boron layer is deposited using electron-beam evaporation. Freshly cleaved rock salt (NaCl) is used as a substrate.

1) Reactive sputtering of silicon- nitrogen film:

A two-inch silicon target (99.9999 % purity) is sputtered in pure nitrogen (UHP-grade from Praxair) using an Angstrom Sciences, Inc. magnetron gun in a cryopumped system. The base pressure should be $2x10^{-7}$ torr or better. The nitrogen pressure during sputtering measured using an MKS Baratron® capacitance gauge was $7.2x10^{-3}$ torr. The substrate is positioned at the same level as the sputtering source, at a distance of 15 cm from the source. The thickness monitor is positioned at a distance 29.5 cm from the sputtering source. The thickness monitor settings are:

- density = 2.32 g/cm^3
- Z-factor = 0.712
- tooling factor = 100 %.

A 13.6 MHz power supply is used to deliver 140 W of forward power to the target. Typically the reflected power is 25 W. The target must be pre-sputtered for at least 6 minutes (preferably 10 min) with a closed shutter. The deposition rate on the thickness monitor is about 0.1 Å/s and final thickness of the film read by the thickness monitor should be 14 Å. It takes approximately 5.5 minutes to 7 minutes. The sample has to be left under vacuum for at least another hour to cool.

2) e-beam evaporation of Boron onto silicon-nitrogen film described above:

The boron is e-beam evaporated in the same system as used for fabrication of sample A (paragraph 7.1.1). Crystalline boron pieces from Alfa Products (#00430

–m2N8) in a molybdenum crucible are used as the source material. The thickness monitor settings are:

- density = 2.54 g/cm^3
- Z factor = 0.389
- tooling factor = 225 %

The base pressure in the system before deposition is 1.5×10^{-6} torr or better. The electron gun is run at 9 kV and filament current is 0.34 A. The deposition rate should be in the order of 2 Ås^{-1} to 3 Ås^{-1}. The final film thickness read by the thickness monitor should be 8 Å. The source should be cleaned by pre-evaporating with closed for a few minutes.

Finally the NaCl substrate is dissolved by slow immersion to a deionized water and the floating film is collected onto a 200 mesh copper grid. Consequently, the silicon-nitrogen film should be closer to the copper grid and the boron layer should be at the top.

A.3 Sample C (Boron, Fluorine, Magnesium, Silicon)

This sample is designed for measurement of Cliff-Lorimer factors of boron ($k_{B/Si}$), fluorine ($k_{F/Si}$) and magnesium ($k_{Mg/Si}$) with respect to silicon. The film is fabricated in three steps. First, a silicon film is grown onto a freshly cleaved rock-salt (NaCl) substrate. Second, a thin film of magnesium fluoride (MgF_2) is deposited on the silicon film. Finally, a boron film is grown on the above layered sample. Electron beam evaporation is employed to make all three layers.

1) deposition of silicon:

Pieces of silicon wafer in a molybdenum crucible are used as a source for electron beam evaporation. The base pressure in the chamber should be 1.5×10^{-6} torr or better. The settings of the thickness monitor are as follows:

- density = 2.32 g/cm^3
- Z factor = 0.712
- tooling factor = 225 %

The electron gun is run at 9 kV and the filament current is 0.3 A. The deposition rate should be between 0.5 $Å s^{-1}$ and 2.5 $Å s^{-1}$ and the final thickness on the thickness monitor should be 120 Å. The film needs to cool under vacuum for about an hour before venting the vacuum chamber.

2) deposition of magnesium fluoride (MgF_2)

MgF_2 powder from Aldrich (# 20831-0) in a copper crucible is used as a source for electron-beam evaporation. The base pressure in the chamber should be 1.5×10^{-6} torr or better. It is necessary to preheat the MgF_2 source gently to avoid outgassing. Since MgF_2 decomposes at high temperatures it is necessary to do the evaporation at as low a source temperature as possible. The setting of the thickness monitor for this deposition is:

- density = 3 g/cm^3
- Z factor = 1
- tooling factor = 225 %

The electron gun is run at 9 kV and the filament current during the deposition is between 0.21A and 0.24 A. The deposition rate should be about 3 $Ås^{-1}$ and the final film thickness on the thickness monitor should be 90 Å. The film should be left under vacuum to completely cool down.

3) deposition of boron

Crystalline boron pieces from Alfa Products (#00430 –m2N8) in a molybdenum crucible are used as the source material. The base pressure in the chamber should be better than $1.5x10^{-6}$ torr. The thickness monitor settings for this deposition are:

- density = 2.54 gcm^{-3}
- Z factor = 0.389
- tooling factor = 225 %

The electron gun is run at 9 kV and the filament current about 0.28 A to 0.32 A. The deposition rate on the thickness monitor should be about 2 $Ås^{-1}$ and the final film thickness on the thickness monitor should be 170 Å. The film needs to cool down under vacuum for about an hour.

Finally the NaCl substrate is dissolved in deionized water and the film is collected onto a 200 mesh copper grid.

Appendix B

Details on contamination lithography in JEOL 2010

Chapters 4 and 5 discuss fabrication of regular arrays of pillars and helices by deposition onto an oblique, rotating substrate (GLAD technique). It appears that the height and repeat distance have to satisfy Eq. 4.1 and certain limitations on the nuclei diameter to promote growth of regular arrays. The fabrication of such nuclei is straightforward when their diameter and repeat distance fall within the reach of standard electron-beam lift-off lithography (chapter 4). The GLAD technique however, is capable of control over the fabrication on a scale smaller than can be reached by lift-off lithography. Electron-beam contamination lithography in TEM is one approach capable of overcoming the limitations of the lift-off process. This approach exploits the well-know phenomenon of localized contamination build up within an area irradiated by electron beam. Below is a detailed description of the contamination lithography process. Additionally, the chapter 7.3 contains a listing of the program used to position the beam in the TEM.

One of the limitations of the lift-off process and lithography on a bulk silicon substrate is exposure of the photoresist by the backscattered electrons, an effect which causes difficulties when the feature size gets smaller than about 100nm. This limitation can be overcome by using a thin (~ 10 nm) light-element substrate, where exposure by backscattered electrons is largely eliminated. Further reduction of the exposure by backscattered electrons can be achieved by increasing the energy of the

incident electrons (to 200 keV in our case). A further requirement for reproducible lithography below 100nm is adequate spatial and temporal stability of the electron beam, to guarantee the necessary probe size and repeatable beam positioning. All of these requirements can be satisfied by using a transmission electron microscope (such as the JEOL 2010) capable of forming a convergent beam and equipped with some means of beam scanning. Scanning of the beam was achieved by using the internal programming language of the JEOL 2010.

An amorphous 10nm-thick carbon film mounted on a 200mesh copper grid is used as the substrate for lithography. Localized contamination build-up on the area illuminated by electron beam is used to write the dot-pattern array. When the desired dimension of the contamination dots is in the range of several nanometers, it is preferable to use a local vapor source for the contamination, rather than relying on diffusion along the film surface. A microscopic drop of mechanical pump oil (vapor pressure 10^{-5} torr at room temperature) is dropped on the side of the sample-retaining ring and acts as the hydrocarbon-contamination source. There is therefore no direct contact of the contamination source (microscopic oil drop) and the substrate (10 nm-thick carbon film). The contamination thickness deposited depends on the total charge (beam current times time), for given partial pressure of the contaminant. Subsequently, the height of the nuclei can be controlled by the beam dwell-time at each point (in our case 1 second to 2 seconds for beam current $I = 6 \times 10^{-11}$ A). This method allows the growth of high-aspect-ratio artificial nuclei, as required for complete shadowing of the substrate between the nuclei. It relies on the fact that the polymerization of

hydrocarbons takes place only in the area irradiated by the electron beam, whether the beam is positioned on a fresh substrate or on a partly fabricated nucleus. Arrays up to about 2 μm x 2 μm, with repeat distance down to 18 nm, can be written using this technique; writing larger areas requires inconveniently long exposures. The JEOL 2010 allows beam positioning to within one nanometer and forms a (convergent) probe down to about 1 nm in diameter. However it is difficult to write arrays with repeat distance smaller than 10 nm, due mainly to the polymer nature of the contamination deposit (written patterns tend to "flow") and also to sample drift during the writing process.

Appendix C

Program for beam scanning in JEOL 2010 TEM

As described in chapter 5, the JEOL 2010 transmission electron microscope was employed to pattern substrates in cases where small (below 100 nm) repeat distance was desired, and for samples dedicated to study of the initial stages of the film growth. The beam positioning for writing these patterns (arrays of nuclei) was done using the internal programming language of the JEOL 2010 microscope. The program (named "SCAN") with comments is listed below.

Program	Comment
10 UFC I, 20	sets a user function
20 INPUT "X" X	- reads value of size of the regular array in units of steps of the microscope deflection coils
30 DFC 5,X,0	- the beam is moved through all four
32 DFC 5,X,X	corners of the square array to be
34 DFC 5,0,X	written
36 DFC 5,0,0	
38 DFC 5,-X,-X	- moves the beam to a dummy point outside the area where the array will be written
70 INPUT "?? OK = 1" Q	- asks for confirmation that the

	positioning of the area to be written is correct, chance for a user to change the size and position of the area before writing the array
80 IF Q < > 1 GOTO 20	- will return program to ask for new size X of the array
90 INPUT "# OF POINTS" N	- asks user to specify to how many intervals the arrays (size X) should be divided in both *x* and *y* directions
100 A=X/N	- calculates the repeat distance of the array
105 DFC 5,X,X	- moves the beam back from the dummy point to the corner of the array to be scanned
110 FOR I=0 TO N-1	- loop controlling stepping in *x* direction
130 FOR J=0 to N-1	- loop controlling stepping in *y* direction
140 DFC 5,0,A	- moves the beam by step A in *y* direction
145 BEEP	
150 FOR K=0 TO "user defined number"	- sets the exposure time for one point

	by executing a dummy loop "user defined" times. One loop takes about 0.1 sec
160 NEXT K	- end of dummy loop
170 NEXT J	- moves back to line 130
180 NEXT I	- moves back to line 110
190 DFC 5,-2*X,-X	- moves the beam to a dummy point
200 UFC C,20,0,FFFF	
210 BEEP	
220 BEEP	- double beep when writing is finished
230 STOP 230	- stops the execution of the program

This program is sufficiently short to be easy to maintain and modify. It allows writing a lattice of different symmetry (hexagonal or even circular patterns) by easy modification of the scanning loops. The fifth deflector is used to move the beam in the specimen plane (command DFC 5,X,X – the first number specifies which deflector is addressed).

At the beginning, the beam is scanned through all four corners of the square array (lines 30 to 38) to give user a chance to verify the position where the array will be written, as well as the *real* size of the array. Entering anything except "1" as an answer to the question on line 70 will result in a return to line 20 and a prompt for a new value of X. The repeat distance (lattice constant) of the array to be written is the size of the

array X divided by number of points N. The step size can be different for different operating modes of the TEM but is verified by the user by scanning the beam through all four corners (lines 30 to 38). The loop in K (lines 150 and 160) is used to set the exposure time; one loop takes about 0.1 sec and typical value for the "user defined number" is between 10 and 20. Due to excellent beam current stability and repeatability, I found it more convenient to edit in line 150 when the exposure time is to be changed, rather than prompt the user to enter the value each time the program is run.

The following commands may be useful to a user:

CONS – switches the display to console mode

FILES – prints all programs stored in the microscope

LOAD *name* – loads program *name*

LIST – lists the currently loaded program.

RUN – runs the currently loaded program

P1 – returns from console to page 1

Editing of a given line is done by typing the line number followed by the desired new command and "Enter" key. Pressing ESC key at any time interrupts the program execution.

Appendix D

Lithography on bulk silicon substrates

Regular arrays of pillars and helices described in Chapter 4 and 5 were grown either onto a bulk silicon substrate (100 or 111 oriented wafers) or onto a 10 nm-thick amorphous-carbon substrate. The lithography for growth of regular arrays onto 10 nm-thick carbon substrate is described in appendices 8.2 and 8.3. A brief description of lithography process used to fabricate arrays of artificial nuclei on a silicon substrate is given here.

The artificial nuclei on bulk silicon substrate were fabricated using PMMA-based lift-off process. Silicon wafers 4 inches in diameter were mounted onto a spin coater and squirted with methanol at 4000 rpm to remove dust particles. A 2:3 solution of 950,000-molecular weight polymethylmetacrylate (PMMA) in chlorobenzene was dipped onto a stationary wafer. The substrate was then spinned at 4000 rpm for 30 seconds to obtain uniform layer of PMMA. Such PMMA-coated wafers were baked at 160° C for 1 hour. The resulting photoresist thickness was 270 nm as measured using a step profilometer.

The photoresist was exposed using Phillips 505 scanning electron microscope operated at 30 kV beam energy and 50 nm nominal spot size. As described in chapter 4 an image acquisition system was used to drive the beam. Typical beam current measured using Keithley 610 electrometer was 4×10^{-11} A (not compensated for

secondary electron emission), typical dwell time was 3 ms (300 points written per second). This gives 1.3×10^{-13} C per point with a dose to about 1.6 mC/cm^2. The exposed photoresist was developed in solution of three parts of isopropyl-alcohol (IPA) and one part of methyl-isobuthyl-ketone (MIBK) at room temperature for 70 seconds. The development was followed by wash in IPA for 20 seconds and rinsed in deionized water. Finally the wafer was dried by blowing dry nitrogen.

The material required to form the arrays of artificial nuclei was evaporated onto such substrate using electron beam evaporation. The substrates were positioned next to the thickness monitor oriented perpendicular to the incoming flux of vapour.

The final step of fabrication of arrays of artificial nuclei is removal of areas between the nuclei by dissolving the unexposed PMMA in acetone.

Appendix E

Substrate rotation device for growth using Glancing Angle Deposition (GLAD) technique

Substrate-rotation device used for growth of arrays of pillars and helices by deposition onto an oblique rotating substrate is described in this appendix.

The substrate rotation device is consists of a Hurst Model SAS stepper motor with 1:300 reduction gearbox. Both the stepper motor and reduction gearbox were

mounted outside the vacuum chamber. The stepper motor was driven from a stepper motor controller (Herbach & Rademan TM 98 CTL 3145). The output axle of the reduction gearbox was connected to the inside of the vacuum chamber using an O-ring sealed feedthrough connected to a rotatable substrate holder using two 90° gear-sets inside the vacuum chamber. The controller board for the stepper motor offers a possibility of control by external computer. However, it proved to be more convenient to use the on-board oscillator of the controller board to set desired (constant) rotation rate before deposition. In a typical experiment the angle between the substrate holder and the incoming flux of vapour was set before the experiment by mechanically adjusting the holder. The rotation rate of the stepper motor was set by adjusting on-board oscillator. The rotation rate was measured by timing 10 rotations of the stepper motor axle before 1:300 reduction. The deposition rate was usually controlled manually during the deposition. As a result of keeping both the rotation rate and deposition rate constant the contamination level of the growing film was held constant during the deposition.

Appendix F

Electron energy-loss spectroscopy (EELS)

Collisions of a fast electron with the sample can be elastic or inelastic. Elastic collisions refer to events where the energy transfer to sample is less than the energy resolution of the analytical instrument (for example a TEM with energy-loss spectrometer). If an incoming electrons suffers collisions resulting in measurable

energy transfer, the energy transferred to the sample can be used obtain information about the sample. To retrieve this information on the sample the energy transferred to the sample by such fast electrons has to be measured. A convenient way to analyze the energy of the electrons is by the use of magnetic-prism spectrometer (using the fact that an electron trajectory will bend in magnetic field depending on the velocity of an electron). In practice, such spectrometers bend electron trajectories by an angle of 90 degrees; the trajectories of electrons which suffered inelastic collisions (slower) are bent more than those who interacted with sample elastically. In other words the electrons will be dispersed according to their energy (energy-loss). A photodiode array can be used to detect the different trajectories of the electrons emerging from the spectrometer. The signal (number of counts at given energy loss) is then binned at selected energy intervals giving an EELS spectrum such as in figure 2.1.

The inelastic interaction can be classified by the type of interaction an electron suffered. Interaction with conduction-band electrons leads to plasmon oscillations in the material. The information on those oscillations is in the low-loss part of a spectra (plasmon peak). The interaction of fast electrons with core-level electrons results in higher energy losses (above about 50 eV). The spectral features corresponding to core-level excitations have often an appearance similar to what can be seen in figure 2.1. The shape of such a core-loss edge (after subtraction of non-characteristic background) can provide information on chemical state of the atoms involved in the interaction (near-edge fine structure). The extended fine structure (more than about 50 eV beyond the edge onset) of core-loss ionization edges can additionally provide

information on the local geometry in the vicinity of the interacting atom. The "intensities" of such core loss edges can be used to obtain information on areal density of given type of atom.

Electron energy-loss spectroscopy and related techniques (spectral imaging, energy-filtering transmission electron microscopy and diffraction) are very wide and active research areas. Several books are available to gain more insight in the technique. Ray Egerton's book (Egerton 1996) provides comprehensive review of the technique, underlying theory and practical issues. It also contains large number of references to original publications. An introductory text by David Williams and Barry Carter (Williams Carter 1996) is aimed to users rather than developers of the technique. The book edited by Ludwig Reimer (Reimer 1995) provides a thorough description of several aspects of the technique. Journals publishing a great deal of original work in the field include Ultramicroscopy and Micron.

F.1 References

Egerton R (1996), Electron Energy-Loss Spectroscopy in the Electron Microscope (second edition), Plenum Press 1996.

Reimer L (ed.) (1995), Energy-Filtering Transmission Electron Microscopy, Springer, 1995.

Williams DB, Carter BC (1996), Transmission Electron Microscopy: A textbook for material science, Plenum Press (1996).

Appendix G

Energy dispersive x-ray microanalysis (EDX)

As briefly described in Appendix F the interaction of a fast electron with a sample can be either elastic or inelastic. The inelastic interactions of a fast electron with the sample can lead to excitation of an atom within the sample (for example by removing an inner shell electron). Such an excited atom eventually returns back to the ground state. Different processes of the return to the ground state are possible (radiative transition, Auger process). The radiative return to the ground state involves emission of a photon. The energy of the emitted photon is characteristic for the atom (and energy level) which underwent this process. The analysis of the photons coming out of the sample can therefore yield an information about chemical composition of the sample. Information obtainable from such characteristic x-rays provides basis for energy dispersive x-ray microanalysis (EDX) and wavelength-dispersive x-ray microanalysis (WDX). The detector used for energy-dispersive x-ray microanalysis (EDX) is based on electron-hole pair generation in a semiconductor diode by the photon emitted from the sample. The number of electron-hole pairs created by a photon in such detector is proportional to the energy of the photon, resulting in current pulses in a suitable circuit. Binning of these pulses according to their "size" results in a spectra such as in figure 2.4. Position of a peak in such spectra provides information on the type of atoms in the sample. The peak intensity (number of counts of given "size") provides information on number of photons of given energy. The number of counts of given energy is proportional to areal density of given type of atoms.

Sensitivity of the EDX detector varies with the energy of the incoming photons (generally getting worse for lower energy photons) and can change during the service life of the detector. Therefore the constant of proportionality (sensitivity) between number of counts of given type and the areal density of given atoms has to be obtained experimentally (as described in Chapter 2). These experimentally obtained sensitivity factors (k-factors or Cliff-Lorimer k-factors) can be then used to convert measured intensities of characteristic peaks to chemical composition of an unknown sample.

EDX spectroscopy does not currently yield the wealth of information EELS provides. This is partly due to worse energy resolution of the EDX spectrometer (~ 100 eV compare to ~ 1 eV for EELS). On the other hand EDX spectroscopy is more user-friendly and more convenient to use.

As in case of EELS a vast amount of literature is available to researchers. Book by David Williams and Barry Carter (Williams 1996) discusses the technique in sufficient depth for users of the technique as well as provides references to more advanced texts. The book by Rolf Woldseth (Woldseth 1973) provides an advanced, enjoyable reading on x-ray energy spectroscopy.

G.1 References

Williams DB, Carter BC (1996), Transmission Electron Microscopy: A textbook for material science, Plenum Press (1996).

Woldseth R (1973), All you ever wanted to know about XES* (*X-ray energy spectroscopy), Kevex Corporation (1973).

Appendix H

Selected unpublished micrographs

The aim of this appendix is to provide the reader with additional insight in the growth of obliquely deposited films (chapter 4,5 and 6). The micrographs in this chapter were not published in any journal (at the time of writing of this thesis), but might be of use to a reader trying to understand the growth of the GLAD films.

Bifurcation of the growing structures as discussed in chapter 4,5 and 6 can be controlled by adjusting rotation speed, deposition rate and substrate temperature. The bismuth helix in figure 5.4 is an example of the level of control which can be achieved. It is however illustrative to compare figure 5.4 to a bismuth helix grown onto a room temperature substrate (same as helix in figure 5.4) at a higher ratio of deposition rate relative to the rotation speed. The example of such a helix is shown in figure H1. The small frequency of bifurcation in figure H1 suggests that diffusion processes ($T_s/T_m = 0.55$) are suppressing bifurcation. On the other hand, the upper part of the helix in figure H1 suggests that the helix-arm diameter is eventually determined by the number of fibers growing within a helix arm. Adjustment of the ratio of rotation rate to the deposition rate is therefore necessary to grow single-fiber structures such as in figure 5.4, even at high substrate temperature.

Figure H2 is a cross-sectional transmission electron micrograph of the smallest-repeat-distance array of regular nickel pillars I was able to fabricate by contamination lithography in TEM. The array was deposited at the angle of incidence (between the substrate normal and incoming flux of atoms) a $\theta = 83°$. The substrate was rotated 1.2 rotations during the deposition (at deposition rate 2 Å/s). The small number of rotations during the deposition may be responsible for the somewhat rugged look of the pillars. Other reasons for the rough look of the structures include difficulties with the initial pattern forming process (flow of the written pattern as described in chapter 6 and sample drift during the pattern-writing process) and a steep angle of incidence of the incoming vapour ($\theta = 83°$ as opposed to $\theta = 87°$ for most films).

The decrease in bifurcation rate for pillars in comparison to helices can be seen from figure H3 and H4. Figure H3 is a top view scanning electron (SEM) micrograph of an array of titanium pillars. The micrograph was acquired at angle $\beta = 45°$ between the substrate normal and the electron beam. The film itself was grown at an angle of incidence $\theta = 86°$, deposition rate R = 300 Å/s and rotation rate RPM = 1.6 min^{-1}. Figure H4 is an SEM micrograph (collected at angle $\beta = 57°$) of a film of titanium helices grown at angle of incidence $\theta = 86.3°$, deposition rate R = 300 Å/s and rotation rate RPM = 0.12 min^{-1}. The major difference between these two films is in the ratio of deposition rate and rotation rate. The higher ratio allows for growth of helices, lower ratio allows for growth of pillars. The pillars in figure H3 appear to be fairly solid

Figure H1 Bifurcation in a bismuth helix. Grown at $\theta = 86°$, RPM = 0.2 min^{-1}, and R = 70 Å/s. Scale bar corresponds to 200 nm. Compare with figure 5.4.

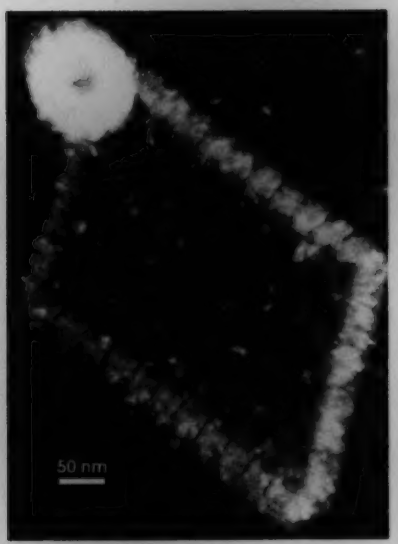

Figure H2. Array of nickel pillars with repeat distance ~ 18 nm. Grown at $\theta = 83°$, R = 2 Å/s. The substrate was rotated 1.2 rotation during the film growth. Sample drift was a problem during writing of the initial pattern in the TEM. Scale bar corresponds to 50 nm.

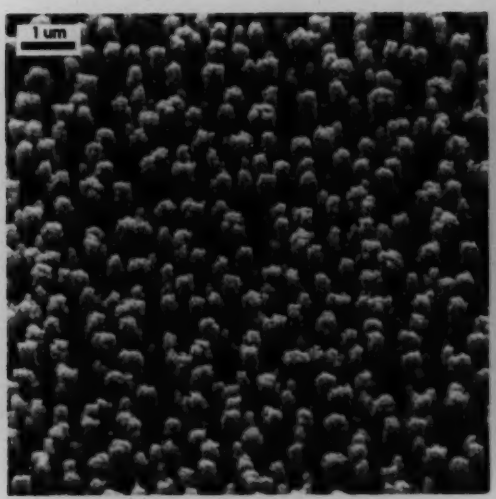

Figure H3 Bifurcation in titanium pillars. Grown at $\theta = 86°$, R = 300 Å/s and RPM = 1.6 min^{-1}. Compare with figure H4.

Figure H4 Bifurcation in titanium helices. Grown at $\theta = 86.3°$, R = 300 Å/s and RPM = 0.12 min^{-1}.

structures. The helices in figure H4 have the appearance of brooms of separated fibers growing within an individual helix. It can be said that in case of helices a newly starting fiber survives for considerable portion of growth but in case of pillars a newly starting fiber is promptly shadowed by the main pillar (TEM micrographs).

The influence of a point defect (a missing pillar) on the growth of regular arrays of silicon pillars can be observed in figure H5. This figure is from a regular array of silicon pillars within the same sample as figure 5.2 and figure 5.11a. The defect originates from a missing artificial nuclei in the initial pattern of nuclei. The increase in the amount of debris between the pillars within the defect is much smaller than in case of line defect in figure 5.11a. The change in diameter of pillars adjacent to the defect is also much less pronounced than for the line defect in figure 5.11a. The smaller increase of the depth reached by the incoming flux (compared to the line defect in figure 5.11a) is likely to be responsible for the minor influence of a point defect.

The quality of the initial pattern (and resulting array of initial nuclei) can have an influence on a microstructure of the regular array. Figures H6 and H7 provide information on the quality of the initial patterns for growth of regular arrays of pillars or helices. Figure H6 is a perpendicular-view SEM micrograph of an initial pattern exposed and developed in PMMA photoresist. The pattern was created by onto bulk silicon substrate using Phillips 505 scanning electron microscope (as described in Chapter 4, 5 and 6 and in Appendix D). The initial pattern (even before deposition and

lift-off of initial nuclei) already has imperfections. Figure H6 reveals that the sizes of the holes in the photoresist are not uniform; that the holes in the photoresist are not round (stigmatism of the pattern-writing beam) and some of the holes are even joining together (upper part of the figure). Despite these imperfections (likely amplified by the lift-off process during the fabrication of the initial nuclei) subsequent deposition onto such initial array results in a good quality regular array of pillars or helices. The good quality of the resulting arrays of pillars and helices deposited onto such an imperfect initial array of nuclei suggests robustness of the growth process.

A substrate (10 nm-thick amorphous carbon film) patterned in transmission microscope (TEM) is shown in figure H7. The repeat distance of this array of artificial nuclei is about $a = 52$ nm. Note that these are dots of contamination on the substrate (as described in more detail in Chapter 6, Appendix B and Appendix C) and the pillars or helices are deposited directly onto this exact array (no lift-off or other technological step prior the growth). The TEM-patterned initial array of artificial nuclei exhibits much less imperfections than the SEM-patterned arrays onto bulk silicon substrate. The slight difference in the contrast around one nuclei can be attributed to beam tilt during the acquisition of the TEM image (imaging artifact) or during the patterning process (nuclei "tilted" with respect to the substrate normal).

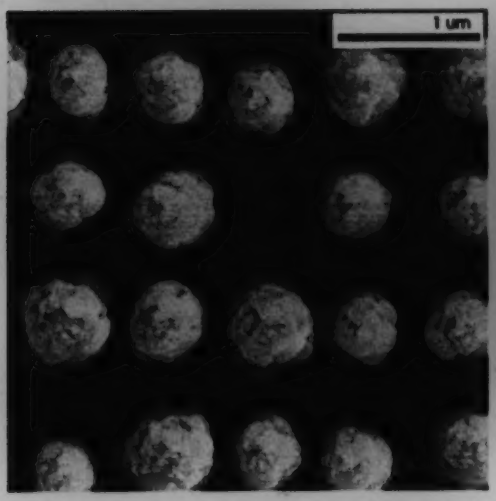

Figure H5 Point defect in a regular array of silicon pillars. The scale bar corresponds to 1 μm. Grown at $\theta = 83°$, R = 55 Å/s, RPM = 0.6 min^{-1}. Compare to figure 5.11a.

Figure H6 initial pattern patterned onto bulk silicon substrate. PMMA photorezist. Scale bar corresponds to 500 nm.

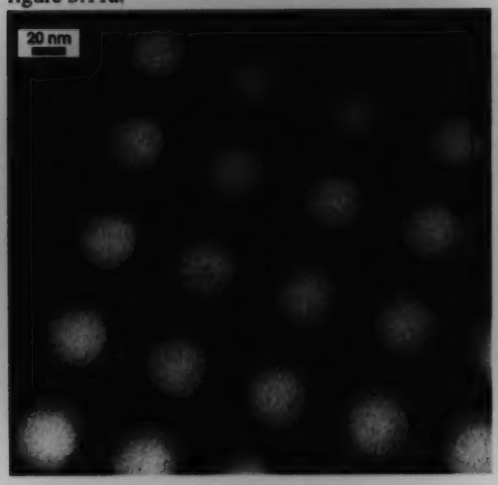

Figure H7 Initial pattern created by contamination lithography in TEM. The scale bar corresponds to 20 nm.

Figure H8 is a cross sectional scanning electron micrograph of the initial stages of growth of silicon helices – initial ~100 nm in helix-height where most of the helix terminations occur (Chapter 5, paragraph 5.3.1.1 and 5.3.1.4). This high-magnification SEM micrograph however has been taken close to information limit of the JEOL JSM 6301 FXV microscope for this type of sample (probably determined by penetration of the electron beam through the studied structures). Figure H8 was taken from the same area of the same sample as figure 5.2 and from the same sample as figure 5.11a and figure H6. Further insight in the initial stages of growth of helices can be gained from figure 6.3 and corresponding text in Chapter 6.

Figure H9 illustrates the relation between the size of the crystallites and fiber diameter in nickel helices (Chapter 5, paragraph 5.3.1.2). This figure reveals that each newly starting fiber is composed of many individual crystallites (inset) with size much smaller than the diameter of a newly starting fiber. As discussed in paragraph 5.3.1.2, this suggests that (for low substrate temperature) the crystallinity of the growing material occurs on a scale smaller than the fiber diameter. The branching occurs on a scale much larger than crystallite size. The crystallite size is believed to be comparable to adatom diffusion length. The branching therefore occurs on a scale much larger than the adatom diffusion length.

The cross sectional TEM micrograph in figure H10 provides insight to the change of a growing microstructure from a helix to a pillar. In the bottom part of this figure the helical microstructure is well developed. As the helices continue to grow some of

them are terminated (shadowed by their neighbors). This leads to increased spacing between the surviving helices. Consequently, the amount of material collected by survivors increase, leading to filling of the helix-pitch and change of the helical microstructure to pillar-like microstructure. The same behavior can be observed from comparison of figures 5.2 and 5.11b in chapter 5. Both of these figures are from the same sample. The increase in spacing between the structures within the regular array (compared to the random area) leads to change in microstructure from helices (random area, figure 5.2) to pillars (regular area, figure 5.11b). It can be said that the deposition rate, rotation rate and the spacing between the structures determine the microstructure (helical or pillar) of the growing film (for a fixed angle of incidence θ). In the case of random arrays, the spacing between the structures is given by the randomness of the nucleation process. Regular arrays provide the opportunity to determine the spacing independently of the deposition process (by fabrication of arrays of initial nuclei with appropriate repeat distance).

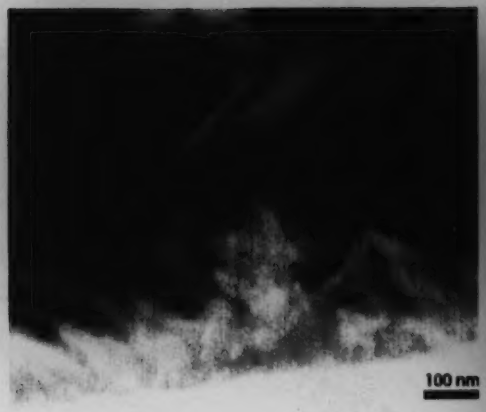

Figure H8 SEM micrograph of initial stages of growth of silicon helices. Grown at $\theta = 83°$, R = 55 Å/s, RPM = 0.6 min^{-1}. The scale bar corresponds to 100 nm.

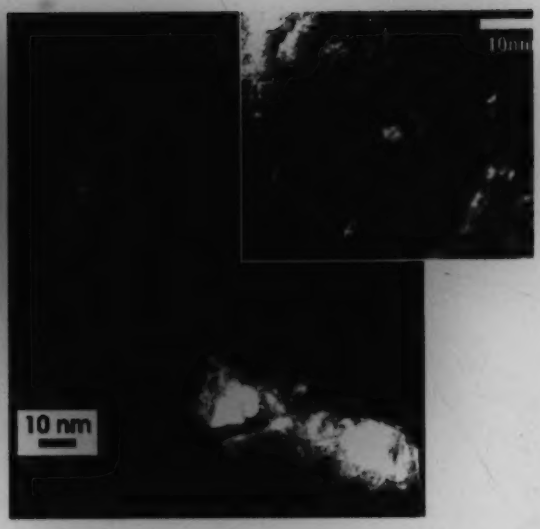

Figure H9 Detail revealing the relation of crystalline nature of nickel helices. The inset is a higher magnification of the same helix. Grown at $\theta = 88°$, R = 9 Å/s and RPM = 0.04 min^{-1}. Refer to paragraph 5.3.1.2 for more detail. Scale bars correspond to 10 nm.

Figure H10 Relation between helices and pillars. Helices are grown by filling helix-pitch. Titanium film grow at $\theta = 86°$, R = 300 Å/s and RPM = 1.6 min^{-1}. Scale bar corresponds to 200 nm.